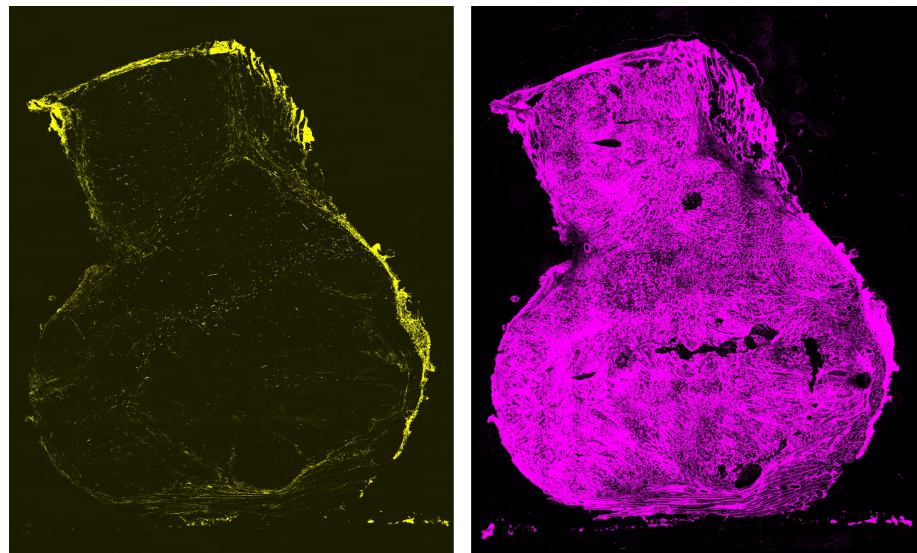


Håkon Fosslund Wesche

Identifying Barriers in Extracellular Matrix for Ultrasound-Mediated Delivery of Nanoparticles in 4T1, KPC and CT26 Tumor Models

Master's thesis in Nanotechnology
Supervisor: Catharina de Lange Davies
Co-supervisor: Caroline Einen
July 2023



Håkon Fosslund Wesche

**Identifying Barriers in Extracellular
Matrix
for Ultrasound-Mediated Delivery of
Nanoparticles in 4T1, KPC and CT26
Tumor Models**

Master's thesis in Nanotechnology
Supervisor: Catharina de Lange Davies
Co-supervisor: Caroline Einen
July 2023

Norwegian University of Science and Technology
Faculty of Natural Sciences
Department of Physics



Norwegian University of
Science and Technology

Abstract

One of the challenges with cancer therapies today, is that only a small fraction of the drug accumulates in the tumor. The dense extracellular matrix (ECM) in tumor tissues is thought to be a reason for this. Hyaluronic acid and collagen are two ECM constituents that are often linked to poor prognosis and are theorized to be barriers that could hinder drug penetration into the tumor interstitium. Advanced nanoparticle drug-delivery systems have been developed to increase tumor accumulation and drug penetration so that the drugs reach all the cancer cells. Ultrasound-mediated delivery of drug-loaded nanoparticles is one of these. This technique uses the interactions between microbubbles and ultrasound that mechanically influence the tumor tissue to increase the uptake and penetration of nanoparticles.

This work studied three murine tumor models: 4T1 breast cancer, CT26 colon cancer, and KPC pancreatic cancer. The area fractions of hyaluronic acid and collagen were characterized in thin frozen tumor sections using confocal laser scanning microscopy. Imaging of the hyaluronic acid was through immunostaining and the collagen was imaged using second harmonic generation. To evaluate the effect of these ECM constituents on drug delivery, the tumors were injected with fluorescently labeled liposomes, and the extravasation distance of these liposomes from the blood vessels into the tumor interstitium was studied. Half of the tumors were also treated with ultrasound and microbubbles (USMB), to evaluate the effect of this treatment method and see if it could improve the penetration of the liposomes through the dense ECM into the tumor interstitium.

It was found that the KPC tumors had larger area fractions of hyaluronic acid and collagen compared to the 4T1 and CT26 tumors, although not statistically significant. The values for the area fractions of hyaluronic acid and collagen were in accordance with the range of values reported in the literature. The mean extravasation distance was shorter for the USMB-treated KPC tumors compared to the USMB-treated 4T1 and CT26 tumors. This indicates that both hyaluronic acid and collagen can be barriers to drug penetration into the interstitium. It also indicates that ultrasound and microbubble treatment can increase the extravasation distance of drugs for some tumor models, and not for others.

Lastly, it is possible that the shorter mean extravasation distance in the KPC tumors was due to the denser ECM. However, since the results in this study were not statistically significant and came from a small sample size one cannot be sure. Several other parameters could have contributed to the discrepancy, and more research is needed to identify the main barriers for drug delivery. Even though the results were not conclusive, studies like this illuminate the mechanisms for ineffective treatment of cancer and are an important step on the path to curing cancer.

Sammendrag

En av utfordringene ved dagens kreftbehandlinger er at kun en liten del av medisinene akkumuleres i svulsten. Man tror noe av grunnen til dette skyldes at den ekstracellulære matriksen (ECM) i svulstvevet er ekstra tettpakket. Hyaluronsyre og kollagen er to ECM komponenter som ofte henger sammen med dårligere prognoser, og man tror at disse kan hindre medisiner fra å trenge gjennom svulstvevet. Avanserte nanopartikkel medikamentleveringssystemer har blitt utviklet for å øke oppsamlingen av medisin i svulsten, og i tillegg, øke penetrasjonsdistansen i svulstvevet slik at medisinene når alle kreftcellene. Ultralyd-mediert levering av medikamentlastede nanopartikler er en av disse. Teknikken utnytter interaksjonene mellom mikrobobler og ultralyd som mekanisk påvirker svulstvevet slik at oppsamlingen og penetrasjonen av nanopartikler inn i svulstvevet øker.

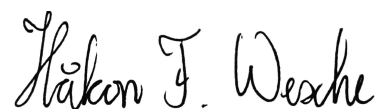
I dette arbeidet så vi på tre murine svulstmodeller: 4T1 brystkreft, CT26 tarmkreft og KPC pankreaskreft. Arealfraksjonene av hyaluronsyre og kollagen ble karakterisert i tynne fryste svulstsnitt ved konfokal laserskanning mikroskopi. Hyaluronsyren ble avbildet gjennom immunfarging, og kollagenet ble avbildet gjennom det andreharmoniske signalet. For å evaluere effekten av disse ECM komponentene på medikamentlevering, ble fluorescerende liposomer injisert i svulstene og ekstravaseringsavstanden fra blodårene inn i svulstvevet ble studert. Halvparten av svulstene fikk også ultralyd og mikroboble (USMB) behandling for å se på effekten behandlingen og om den kunne forbedre leveringen av liposomene gjennom den tettpakkede ECM-en inn i svulstvevet.

Resultatene viste at KPC svulstene hadde høyere arealfraksjon av både hyaluronsyre og kollagen sammenlignet med 4T1 og CT26 svulstene, men forskjellen var ikke statistisk signifikant. Verdiene for arealfraksjonene av hyaluronsyre og kollagen var også sammenlignbare med litteraturen. Det ble også funnet at den gjennomsnittlige ekstravaseringsavstanden, var kortere for de USMB-behandlede KPC svulstene, sammenlignet med de USMB-behandlede 4T1 og CT26 svulstene. Dette indikerer at både hyaluronsyre og kollagen kan være barrierer for levering av medisiner til svulster. I tillegg, indikerer det at USMB behandling kan øke ekstravaseringsavstanden for noen svulstmodeller og ikke øke den i andre svulstmodeller.

Til slutt er det viktig å si at den kortere gjennomsnittlige ekstravaseringsavstanden i KPC svulstene kan ha blitt forårsaket av en tettere ECM, men siden resultatene i denne studien ikke var statistisk signifikante og var basert på et relativt lite antall prøver kan man ikke konkludere med det. Andre parametere som ikke ble studert kan også ha bidratt til denne forskjellen, og mer forskning trengs for å identifisere de viktigste barrierene for medisinlevering i kreft. Selv om resultatene ikke var entydige, bidrar studier som denne med å belyse mekanismer for ineffektive behandlingsmetoder og er et viktig steg på veien til å kurere kreft.

Preface

This master's thesis is written as the final work of the five-year master's program in Nanotechnology with a Bionanotechnology specialization at the Norwegian University of Science and Technology. This thesis was written in the spring of 2023 at the Department of Physics under the Faculty of Natural Sciences. This project is a continuation of the author's project thesis work, *Characterization of extracellular matrix constituents in three murine tumor models*, which started in the fall of 2022 and was finished in the winter of 2023. Some parts of this thesis are rewritten from the project thesis and may overlap, specifically some sections in the *Theory*. Caroline Einen, Sofie Snipstad, Einar Sulheim, and Veronica Nordlund performed the animal experiments described in this thesis.



Håkon Fossland Wesche
10th July 2023

Acknowledgements

First of all, I would like to thank my supervisor Professor Catharina de Lange Davies for being an amazing supervisor. I have learned so much about being a scientist under your guidance and I am extremely grateful for all the feedback, care, and motivation you have instilled in me. Secondly, a huge thanks to my Co-supervisor, Caroline Einen, for always being available for discussions and giving me thorough feedback about the experimental work, the writing of this thesis, and always having a positive outlook. A special thanks to Astrid Bjørkøy for training me on the confocal laser scanning microscope, and being a great discussion partner on all things image acquisition and processing. My thanks to Sofie Snipstad as well, for training me in immunostaining of tumor sections and for sharing her expertise with me.

For my friends from back home: Every "Kaffeslabberas" this spring has been an energy boost and I must thank all of you for being the most caring, hilarious, and genuine group of people I know. I am also grateful for the support and care from my family, especially my twin brother, Andreas.

A round of applause is given to my fellow nanotechnology students in Kull 18. What an enthusiastic, eclectic, and amazing group of people to have spent the last five years with! A special mention to Vilde, Erica, Susanne, Vilde, Amalie, Hedda, Kasper, and Rakel. Words cannot describe how glad I am to have met you guys, and I can't wait for future adventures!

I would like to dedicate this master's thesis in memory of my father, Finn Aage Wesche, who passed away from cancer last year. Thank you for always believing in me, and encouraging me through peaks and valleys these last five years.

List of Acronyms

TME	tumor microenvironment
ECM	extracellular matrix
CAF	cancer-associated fibroblast
NP	nanoparticle
DDS	drug delivery systems
EPR	enhanced permeability and retention
USMB	ultrasound and microbubble
MB	microbubble
PDAC	pancreatic ductal adenocarcinoma
GAG	glycosaminoglycans
sGAG	sulfated-glycosaminoglycans
HA	hyaluronic acid
IFP	interstitial fluid pressure
CW	continuous wave
PW	pulsed wave
PRP	pulse repetition frequency
DF	duty factor
MI	mechanical index
UCA	ultrasound contrast agents
HES	hematoxylin-eosin-saffron
LED	light emitting diode
WLL	white light laser

AU airy unit

CLSM confocal laser scanning microscope

AOTF acousto-optic tunable filter

PMT photomultiplier tube

HyD hybrid detectors

MP multiphoton

SHG second harmonic generation

SHGF second harmonic generation forward

SHGB second harmonic generation backward

CMIC Cellular and Molecular Imaging Core Facility

HABP hyaluronic acid binding protein

NA numerical aperture

BV blood vessel

ROI region of interest

SC subcutaneous

OT orthotopic

Contents

Abstract	i
Sammendrag	ii
Preface	iii
Acknowledgements	iv
List of Acronyms	v
1 Introduction	1
2 Theory	3
2.1 Cancer	3
2.2 Tumor Models	3
2.2.1 4T1	4
2.2.2 CT26	4
2.2.3 KPC	5
2.3 Extracellular Matrix in Tumors	5
2.3.1 Collagen	6
2.3.2 Glycosaminoglycans	7
2.4 Drug Delivery Systems for Cancer	7
2.4.1 ECM as a Barrier for Drug Delivery	8
2.5 Ultrasound and Microbubble Treatment	9
2.5.1 Fundamental Physics of Ultrasound	9
2.5.2 Generation of Ultrasound and Medical Applications	10
2.5.3 Biophysical Effects of Ultrasound	11
2.6 Staining of Biological Components	12
2.6.1 HES Staining	13
2.6.2 Fluorescent Staining	13
2.7 Fluorescence Microscopy	15
2.7.1 Fundamentals of Fluorescence	15
2.7.2 Epi-Fluorescence Microscopy	16
2.7.3 Confocal Laser Scanning Microscopy	17
2.7.4 Multiphoton Microscopy and Second Harmonic Generation	18

3	Materials and Methods	20
3.1	Materials	20
3.1.1	Cell Lines and Cell Culture Chemicals	20
3.1.2	Chemicals	20
3.1.3	Equipment	21
3.2	Methods	21
3.2.1	Tumor Cell Implantation	21
3.2.2	Pearl Epifluorescent Imaging	22
3.2.3	Ultrasound and Microbubble Treatment	22
3.2.4	Tumor Harvest and Sectioning	24
3.2.5	Hyaluronic Acid Immunofluorescent Staining	25
3.2.6	Confocal Laser Scanning Microscope Imaging	25
3.2.7	HES Imaging	29
3.2.8	Image Analysis	29
4	Results	35
4.1	Characterization of Tumor Models	35
4.1.1	Hyaluronic Acid Area Fraction	35
4.1.2	Collagen Area Fraction	36
4.1.3	SHG F/B ratio	38
4.1.4	Cell Density	39
4.2	Tumor Weight and Area Fraction Correlation Analyses	40
4.3	Effect of USMB Treatment on Uptake of Liposomes	42
4.3.1	Uptake Timelines for Tumor Models	42
4.3.2	Uptake of Ex Vivo Tumors	44
4.4	Correlation Between Tumor Uptake of Liposomes and Area Fractions of ECM Constituents and Cell Density	45
4.5	Effect of USMB Treatment on Extravasation Distance of Liposomes	47
4.5.1	Mean Extravasation Distances of NP Clusters	47
4.5.2	Fraction of NP Clusters as a Function of Extravasation Distances	52
4.6	Correlation Between Extravasation Distances, and ECM Constituents and Cell Density	55
5	Discussion	57
5.1	Characterization of Tumor Models	57
5.1.1	Hyaluronic Acid Area Fraction	58
5.1.2	Collagen Area Fraction	59
5.1.3	Collagen Organization Measured by the SHG F/B Ratio	61
5.1.4	Cell Density	61
5.1.5	Tumor Weight and ECM Constituents	62
5.1.6	Quality of Tumor Sectioning	62
5.2	Effect of ECM Constituent on Liposome Uptake and Extravasation Dis- tance	63
5.2.1	Interpreting the Tumor Uptake and Extravasation Distance of Liposomes	63

5.2.2	Hyaluronic Acid as a Barrier for Nanoparticle Delivery	64
5.2.3	Collagen as a Barrier for Nanoparticle Delivery	65
5.2.4	Cell Density as a Barrier for Nanoparticle Delivery	66
5.3	Effect of USMB Treatment on Liposome Uptake and Extravasation Dis- tance	66
5.3.1	Effect of USMB Treatment on Uptake of Liposomes	66
5.3.2	Effect of USMB Treatment on Extravasation of Liposomes Into the Tumor Interstitium	67
5.4	Future Work	69
6	Conclusion	70
	References	72
A	Data for plots	78
A.1	Tumor Weights	78
A.2	Hyaluronic Acid Area Fraction Data	79
A.3	Collagen Forward Area Fraction Data	80
A.4	Collagen Backward Area Fraction Data	81
A.5	F/B Ratio Data	82
A.6	Cell Density Data	83
A.7	Uptake Timeline Data	84
A.8	Uptake Ex Vivo data	85
A.9	Mean Extravasation Distance Data	86
A.10	Fraction of NP Clusters As A Function Of Extravasation Distances Data	87
A.11	Correlation Coefficients and P-values	88
B	Images	90
B.1	4T1 Tile Scan	91
B.2	CT26 Tile Scan	92
B.3	KPC Tile Scan	93
B.4	Blood Vessel and Nanoparticle Images	94
C	Scripts	97
C.1	Hyaluronic Acid Image Processing Macroscript	97
C.2	Collagen Image Processing Macroscript	97
C.3	SHG F/B Ratio Macroscript	98
C.4	Cell Density Image Processing Macroscript	98
C.5	Blood vessel and Nanoparticle Pre-Processing Macroscript	98
C.6	Extravasation Distance Matlab Script	99

List of Figures

2.1	Simplified schematic of the ECM	6
2.2	Visualization of pulsed ultrasound waves	10
2.3	Biophysical effects of acoustic radiation force and cavitation in a blood vessel	12
2.4	Schematic of direct and indirect immunofluorescence	14
2.5	Jablonski diagram for fluorescence and second harmonic generation	16
2.6	Epi-flourescence microscopy and confocal laser scanning microscope setup	17
3.1	Schematic overview of the ultrasound and microbubble treatment set-up.	23
3.2	Timeline for ultrasound and microbubbles treatment and animal imaging	24
3.3	HES section tile scan image	30
3.4	Overview of ROIs used for the area fraction analyses	31
4.1	Area fraction of hyaluronic acid in 4T1, CT26 and KPC tumor sections.	36
4.2	Area fraction of forward and backward collagen signal in 4T1, CT26, and KPC tumor sections.	37
4.3	SHG F/B ratio in 4T1, CT26 and KPC tumor sections.	38
4.4	Percentage of cell density in 4T1, CT26 and KPC tumor sections.	39
4.5	Correlation matrix of tumor weight and area fractions	40
4.6	Correlation plots between the area fractions and tumor weights	41
4.7	Timeline plots of the mean fluorescence of the liposomes in vivo during and around the USMB treatment	43
4.8	Mean fluorescence from tumors ex vivo 24 h after treatment for the 4T1, CT26, and KPC tumors.	44
4.9	Correlation plots between the ECM constituents, and cell density and uptake of fluorescent liposomes	46
4.10	Mean extravasation distance for the 4T1 tumors in the treated and control group for the entire section, periphery, and center.	48
4.11	Mean extravasation distance for the CT26 tumors in the treated and control group for the entire section, periphery, and center.	49
4.12	Mean extravasation distance for the KPC tumors in the treated and control group for the entire section, periphery, and center.	50
4.13	Mean extravasation distance for the treated and control group for the 4T1, CT26, and KPC sections.	51
4.14	Plot of the percentage of extravasated NP clusters in 4T1 tumor sections at increasing extravasation distances	52

4.15	Plot of the percentage of extravasated NP clusters in CT26 tumor sections at increasing extravasation distances	53
4.16	Plot of the percentage of extravasated NP clusters in KPC tumor sections at increasing extravasation distances	54
4.17	Correlation plots between the area fractions of ECM constituents and cell density, and mean extravasation distances of the fluorescent liposomes	56
B.1	Example of tile scans fromr 4T1 section	91
B.2	Example of tile scans from CT26 section	92
B.3	Example of tile scans from KPC section	93
B.4	Example of the blood vessel and nanoparticle images from 4T1 tumor .	94
B.5	Example of the blood vessel and nanoparticle images from CT26 tumor	95
B.6	Example of the blood vessel and nanoparticle images from KPC tumor	96

Chapter 1

Introduction

Already in 1889, Stephen Paget developed his seed-and-soil hypothesis for metastatic diseases to explain how cancers spread in the body [1, 2]. 134 years later we understand that Paget developed a sound hypothesis, but a cure for cancer is yet to be found. In 2020, The Global Cancer Observatory could report about 10 million cancer-related deaths, and almost 20 million new cases [3]. Despite massive research efforts, the prognoses for a lot of cancers are still poor. In the last 25 years, research efforts have been shifted to look at solid tumors as complex organs with a tumor microenvironment (TME) that can further the pathogenesis [4].

The TME describes the cellular environment around tumors and consists of immune cells, blood vessels, fibroblasts, signaling molecules, and the extracellular matrix (ECM) in which the cells are embedded in [5, 6]. The ECM consists of a network of various macromolecules with different physical and biological properties including collagens and glycosaminoglycans like hyaluronic acid [6]. Fibroblasts are transformed into cancer-associated fibroblasts (CAFs) through signal molecules secreted from the tumor cells and they produce more ECM constituents than regular fibroblasts. Resulting in tumor masses comprising of up to 60 % ECM [4]. This way, a dense ECM can directly inhibit therapeutics from reaching the tumor cells. For instance, an accumulation of collagenous ECM and increased hyaluronic acid are both linked to poor cancer prognosis and resistance to therapies [4]. However, different tumors and their ECM composition can be very heterogeneous [7]. Thus, different tumor ECMs need to be characterized to optimize the therapeutic approaches.

In an effort to increase the delivery of therapeutics through the ECM and into the tumor cells, several nanoparticle drug delivery systems (NP DDS) have been developed [8]. Loading therapeutics in NPs is reported to lead to a larger accumulation of drugs in the tumor site due to the enhanced permeability and retention (EPR) effect [9]. The EPR effect describes tumor tissues' leaky blood vessels and poor lymphatic systems. This allows the NPs to transport over the blood vessel wall into the tumor interstitium, and stay there. To further increase the accumulation of the NPs at the tumor site, one can use focused ultrasound together with microbubbles [10]. Ultrasound and microbubble (USMB) treatment can generate mechanical effects called acoustic radiation forces and cavitation. The acoustic radiation force can increase the NP's penetration through the ECM by causing acoustic streaming and shear stresses that can push microbubbles toward the blood vessel walls and displace tissue. Cavitation is caused by the oscillation of the MBs and this can generate microstreams that create shear stresses that can create pores in the endothelial wall for the NPs to diffuse through.

At higher acoustic pressures the ultrasound can collapse the MBs and this can lead to shock waves and microjets that further push the NPs into the tumor tissue.

This work is part of a research group at NTNU that uses this USMB treatment in solid tumors to uncover the most important mechanisms for successful drug delivery. There are three main objectives for this project: 1) To characterize the ECM in three murine tumor models. Specifically, the collagen and hyaluronic acid in 4T1 breast cancer, CT26 colon cancer, and KPC pancreatic cancer. 2) See if there are any correlations between the amount of collagen and hyaluronic acid and the extravasation distance of fluorescently labeled liposomes from blood vessels. 3) Evaluate the effect of USMB treatment in the three tumor models by studying tumor uptake and extravasation distances of fluorescently labeled liposomes.

This work is a continuation of the author's project thesis from the fall where the amount of collagen and sulfated glycosaminoglycans were biochemically characterized for the same three murine tumor models. Now, collagen and non-sulfated glycosaminoglycans (hyaluronic acid) will be characterized by fluorescent microscopy. With the inclusion of ultrasound-mediated delivery of NPs, this study could illuminate what could be the major barriers in the ECM for the delivery of therapeutics.

Chapter 2

Theory

2.1 Cancer

Cancers are characterized by uncontrolled cell proliferation where the rate of cell division and cell death is unbalanced. This leads to an accumulation of cells into masses which are called tumors [11]. Cancer can be grouped into four main groups: carcinomas, sarcomas, lymphomas, and leukemias. Carcinomas are by far the most prevalent type of cancer, accounting for 90 % of all cancers, and describe cancer originating from epithelial cells covering external and internal organ surfaces. Sarcomas originate from supporting tissues like muscle, bone, fat, and cartilage. Lymphomas describe solid tumors in blood and lymphatic vessels while leukemias describe cancers proliferating in the bloodstream.

In the year 2000, Douglas and Weinberg summarized the essential hallmarks of cancer [12]. The original six hallmarks included *Self-sufficiency in growth signals*, *Insensitivity to anti-growth signals*, *Tissue invasion and metastasis*, *Limitless replicative potential*, *Sustained angiogenesis* and *Evading apoptosis*. These hallmarks are connected to how cancer cells proliferate by influencing each other and the microenvironment, and how they are able to avoid immunodestruction. In 2011 and 2022, this list of hallmarks was expanded upon by the authors to include new and more precise cancer-related properties that have garnered attention in later years [13, 14]. Our understanding of cancer evolves and becomes more complex. Thus, to treat cancer there is a need for new strategies that take target several of these hallmarks.

2.2 Tumor Models

Before testing therapeutics and cancer treatments in humans, animal models are always employed to look at the efficacy and safety of the treatments [15, 16]. Rodents, and especially mice, are most frequently used in these animal studies because they are genomically 95 % similar to humans, rather inexpensive, small, and can easily be genetically modified [15]. There are different categories of tumor models based on whether they originate from humans or mice, where they are grown in the animal, and how they are grown.

A syngenic tumor model is cancer implanted in the same animal the cancer originates from e.g. murine cancer cells or explants implanted in mice [15, 16]. One

advantage of using syngenic mice models is that the mice can have a functional immune system which is useful when looking at therapeutic efficacy. Other advantages include low cost, reproducible tumor histology and growth rates, and easy implementation. The main limitation of syngenic models is whether they are representative enough for human tumors.

A xenograft model is cancer implanted in another species than the cancer originates from e.g. human cancer cells or explants implanted in mice [15, 16]. The main advantage of these models is that they are more clinically relevant for human therapeutics. However, these xenografts must be grown in immunocompromised animals and discrepancies may arise in tumor histology, vasculature, and extracellular matrix [16]. Immunotherapies or immune responses in these mice can not be studied in these mice because of this.

Tumor models can also either be grown orthotopically i.e. in the location/organ where the cancer was derived from or subcutaneously i.e. in the fatty tissue right under the skin [15]. Subcutaneous tumors are often favored due to easy implantation, high reproducibility, and homogeneity in tumor histology and growth rates. Orthotopic tumors are favored when the aim is to mimic the carcinogenesis and metastasis of the tumors. In order to implant in their target organ, complex surgery may be needed and this is costly and challenging. A third option is genetically altering animals so that they spontaneously form tumors. This can be a good representation of how tumors form in humans, but is very costly and has low reproducibility.

2.2.1 4T1

4T1 is a spontaneously formed mammary carcinoma model originating from a BALB/c mouse [17]. This murine breast cancer model is characterized by being highly tumorigenic and invasive with the ability to spontaneously metastasize to multiple different sites. It resembles human mammary cancer in that the tumor cells can easily be inoculated into the mammary gland. 4T1 is also a triple-negative breast cancer model which is more difficult to treat due to the lack of three important cellular receptors [18]. In addition, due to a substantial amount of breast cancer patients being diagnosed with detectable metastases or developing metastatic lesions, it serves as a realistic model [19]. Human xenografts of breast cancer in mice have not shown the same potential despite established metastatic properties in humans.

2.2.2 CT26

CT26 is a chemically induced murine colon carcinoma model originating from Balb/c mice [20, 21]. CT26 is an undifferentiated cancer type, meaning that it is not morphologically similar to its site of origin. Due to this, the CT26 model is aggressive and highly metastatic. It is one of the most used studied carcinomas for drug development because of its easy and reproducible implantation [22].

2.2.3 KPC

KPC also known as PDX-1-Kre is a genetically engineered murine pancreatic ductal adenocarcinoma (PDAC) model [23]. The original KPC model originated from a mixed genetic background of 129Sv and C57BL/6 mice. It was engineered specifically to share PDACs properties of spontaneous formation of fully invasive ductal adenocarcinomas. Later it has been found that the KPC model shares several other key features with PDAC including a robust inflammatory response and exclusion of cytotoxic T cells [24]. There are also similarities between the histopathological properties like cellular morphology, poor vascularity, and metastatic spread. In addition, the KPC model is also characterized by desmoplasia which means that elevated levels of collagen are produced by CAFs in the tumor creating a dense ECM similar to human PDAC [23, 24].

2.3 Extracellular Matrix in Tumors

¹ Cells are embedded in an extracellular matrix that is essential for the structure and function of tissues [11]. The ECM is made up of three main types of constituents: structural proteins, glycosaminoglycans, and adhesive glycoproteins. Structural proteins like collagens and elastins give the tissue its mechanical strength and structure. The proteoglycans form a sugar gel in which the cells and structural proteins are embedded while adhesive glycoproteins like integrins function as anchors between the cells and the ECM. The ratio of these three main constituents will depend on the tissue and will vary greatly from one tissue to another. A simplified schematic of the ECM is shown in Figure 2.1.

Cells called fibroblasts are the main producers of ECM in all tissues [26]. Fibroblasts in regular tissues are usually quiescent and their activation is strictly regulated, but in cancerous tissues, they can be chronically activated and transform into cancer-associated fibroblasts (CAFs) [6, 26]. ECM production increases due to the CAFs always being activated, and as a result, tumors often contain unusually high amounts of ECM. Many studies report this increased amount of ECM being a determining factor in decreasing therapeutic efficacy [4].

¹Section 2.3 Extracellular matrix is rewritten from the author's project thesis [25]. Some parts may overlap.

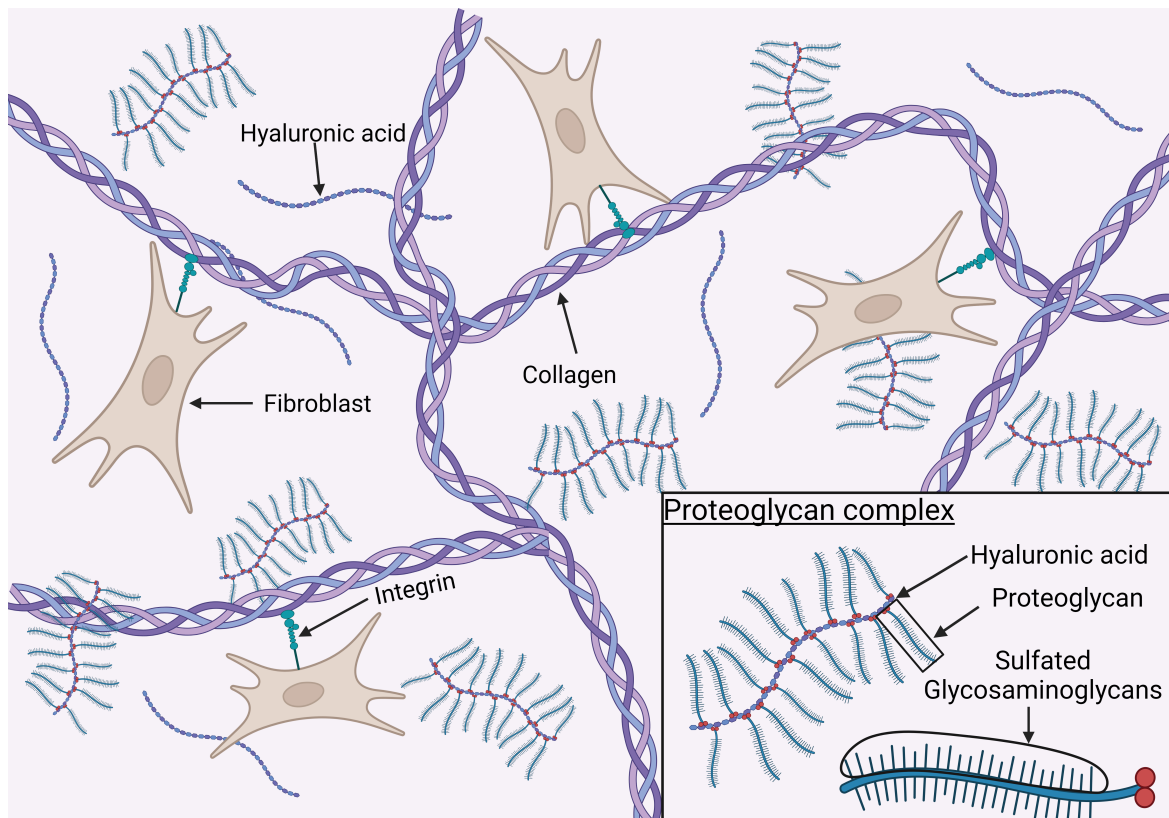


Figure 2.1: Simplified schematic of ECM with emphasis on the collagen fiber network surrounded by an abundance of proteoglycans complexes and free hyaluronic acid. Proteoglycan complexes consist of a hyaluronic acid core with proteoglycans adhered to it. The proteoglycans consist of a core protein, sulfated glycosaminoglycan side chains and a linker protein at the end. ECM-producing fibroblasts are also included. Created with BioRender.com

2.3.1 Collagen

Collagen is the most abundant ECM protein and contributes greatly to the mechanical strength in tissues [11]. Collagens are structured as fibers throughout the ECM and each fiber consists of three collagen fibrils. These fibrils are made up of several collagen molecules which have a triple helix structure and each helix is called an α chain. An alpha chain consists of three amino acids per turn: proline, hydroxyproline, and glycine. There have been identified 28 different collagen sub-groups in vertebrates with collagen type I being the most abundant [27]. Collagen type I, II, III, and V share the classical long fibrillar structure while type IV creates a network-forming structure and is found in basal laminae.

2.3.2 Glycosaminoglycans

The hydrated sugar gel where the fibrillar proteins and cells are embedded consists of large carbohydrates with repeated disaccharides called glycosaminoglycans (GAGs) [11]. The three most common GAGs are chondroitin sulfate, keratan sulfate, and hyaluronate. It is common to group the two first as sulfated glycosaminoglycans (sGAG) and hyaluronate is just the salt of what is commonly known as hyaluronic acid (HA) or hyaluronan. As shown in Figure 2.1, the proteoglycan complex consists of a hyaluronate core with several proteoglycans along the side. These proteoglycans consist of a core protein, sGAG side chains, and a linker protein at the end. HA also exists as a free GAGs, unlike the sGAGs which always are part of a proteoglycan. HA is a polar structure and can bind up to 10000 times its own weight of water [28]. Due to this, it can build a large swelling pressure so that the tissue is able to withstand compressive forces. The GAGs also regulate the transport of nutrients, waste, and signal molecules.

2.4 Drug Delivery Systems for Cancer

² In cancer treatment today, the first treatment option is the surgical removal of the tumor mass[8]. Radio- and chemotherapy are used as supplementary treatments or as the second and third treatment options if surgery is not possible. However, for late diagnoses or aggressive cancers, these methods often do not have a curative outcome. This is often due to a lack of accumulation of therapeutics at the tumor site to get rid of all the cancer cells. In the search for new more effective treatments, advanced drug delivery systems (DDS) have been developed.

Loading the therapeutics in nanoparticles (NP) is one promising strategy for increased delivery of drugs to tumors [29]. The main reasons for loading drugs in NPs is due to their longer circulation time, increased drug stability, and the possibility for controlled drug release. To accumulate into the tumor site and increase the delivery, NPs take advantage of the enhanced permeability and retention (EPR) effect [9]. The EPR effect describes the leaky blood vessels and poor lymphatic drainage caused by underdeveloped vascularization as the tumor grows too quickly. When the NPs enter blood vessels in the tumors they can diffuse through pores in the blood vessel wall, and because of ineffective drainage inside the tumor interstitium, the NP stays there.

Three main strategies for NP DDS include passive targeting, active targeting, and triggered targeting [30]. The passive strategy loads the therapeutics into an NP and relies on the EPR effect for successful delivery to the tumor interstitium. Active targeting modifies the NPs by functionalizing the surface with targeting ligands that have a high binding affinity to a biomarker upregulated in the tumor tissue. Triggered targeting uses external forces or mechanisms to induce drug delivery and release of the NPs at the tumor site only.

²Section 2.4 Drug Delivery Systems is rewritten from the author's project thesis [25]. Some parts may overlap.

A problem when using a passive strategy and relying on the EPR effect is that the NP may be able to transport over the blood vessel wall, but on the other side is a dense ECM which traps the NP and prevents it from reaching the cancer cells [9]. Literature reports that with regular chemotherapy 0.001-0.01 % of the injected dose ends up in the tumor [31]. Wilhelm et al. looked at the fraction reported in the literature between 2006-2016 for NP DDS with a passive targeting strategy and found a median accumulation of 0.7 % in the tumors. This is higher than without using NPs, but still relatively low. To increase this fraction it is important to modify our DDS to increase delivery through the tumor interstitium.

2.4.1 ECM as a Barrier for Drug Delivery

As mentioned in Section 2.3, CAFs produce too much ECM and can also remodel the ECM to further tumorigenesis [32]. To illuminate the barriers for drug delivery through the ECM one must look at the two main mechanisms of transport in the tumor tissue: diffusion and convection [33]. The driving forces for diffusion and convection are concentration gradients and fluid pressure differences, respectively.

The fluid pressure within the tumor interstitium is called the interstitial fluid pressure (IFP) and for convection to contribute to the delivery of therapeutics one needs a higher fluid pressure in the blood vessels than the tumor interstitium [33]. This is not the case since plasma leaks through the blood vessel wall, and this excess fluid drives up the pressure because of poor lymphatic drainage. Solid stress in tumors originating from increased amounts of ECM constituents also contributes to increasing the IFP [34, 33]. Increased production of collagen would increase the tumor stiffness and thus, contribute to the solid stress in the tumor. While increasing the levels of glycosaminoglycans like HA would attract more water, increasing the swelling of the tissue and also increasing the tumor stiffness. Increased solid stress in the tissue will compress the blood and lymphatic vessels, reducing perfusion, increasing the IFP, and reducing the possibility for drug delivery. Another adverse side effect of increased tumor stiffness is that the compression of fibroblasts elicits the transformation into CAFs [32, 33].

This leaves diffusion as the only feasible transport mechanism [33]. Therefore, one must look at what constituents in ECM may inhibit diffusive transport. In 2002 Ramanujan et al. studied gels with collagen and HA at concentrations found in tumors to look at the diffusion of fluorescently labeled IgG [35]. They found that collagen obstructed the diffusion of IgG to a greater extent than HA, but that HA obstructed the diffusion as well. When Stylianopoulos et al. modeled the diffusion of particles in the ECM with a focus on steric, hydrodynamic and electrostatic interactions [36]. Their model concluded that the optimal NP should be cationic to target the tumor vessel before changing to a neutral charge after entering the tumor interstitium. Negatively charged glycosaminoglycans could potentially have repulsive interactions with charged nanoparticles according to their model.

2.5 Ultrasound and Microbubble Treatment

2.5.1 Fundamental Physics of Ultrasound

Ultrasound is acoustic waves propagating through a medium at frequencies above human hearing [37, 38]. Ultrasonic waves propagate through the medium as pressure waves characterized by the movement of molecules in the medium. At a fixed location in the medium, these pressure waves alternate between an increased pressure in the medium which is called compression, and a decreased pressure which is called rarefaction. This compression and rarefaction alternate with repeating pressure waves in a fixed cycle.

The duration of these cycles is defined by the ultrasound frequency, f , which is inversely related to the ultrasound wavelength, λ , through Equation 2.1 [39, 40]. c is the propagation speed which for tissues is assumed to be constant at 1540 m/s. More visually as seen in Figure 2.2, the wavelength is defined as the distance of one cycle and is measured from one compression peak through one rarefaction trough to a new compression peak.

$$f = \frac{c}{\lambda} \quad (2.1)$$

Ultrasound can be generated either as a continuous wave (CW) or a pulsed wave (PW) [39]. The pulse duration, τ , will be described by the number of cycles per pulse, N , and the wave frequency, f , as seen in Equation 2.2.

$$\tau = \frac{N}{f} \quad (2.2)$$

The pulse repetition period (PRP) is the period before the pulse is repeated and it is related to the pulse duration through what is called the duty cycle or duty factor (DF) which describes the fractional amount of time that the pulse is on. It is given by Equation 2.3 where PRF is the pulse repetition frequency. The pulse duration and pulse repetition frequency are illustrated in Figure 2.2.

$$DF = \frac{\tau}{PRP} = \tau PRF \quad (2.3)$$

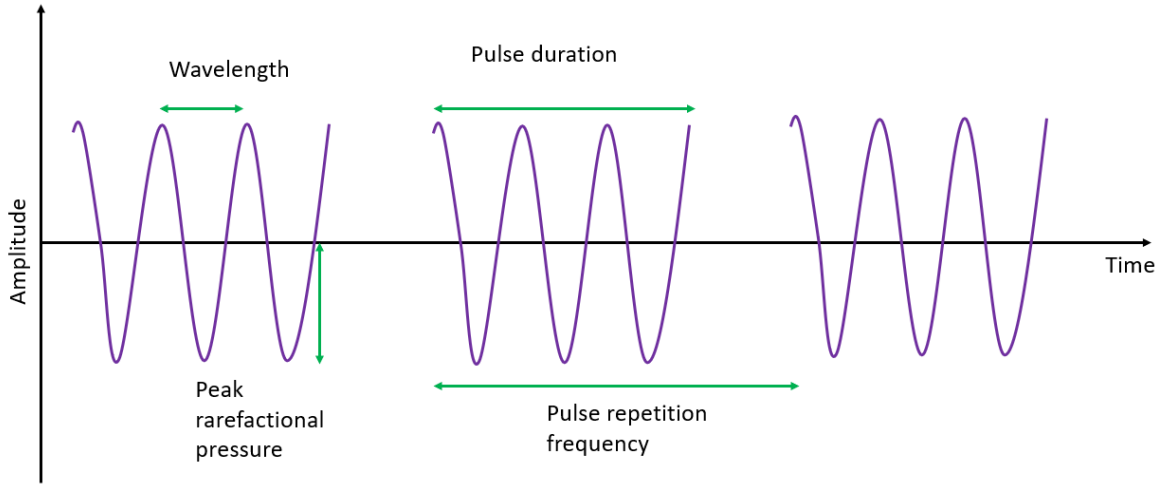


Figure 2.2: Visualization of pulsed ultrasound waves and important parameters including the wavelength, peak rarefactional pressure, pulse duration, and pulse repetition frequency. The figure is adapted from O'Brien [39]

2.5.2 Generation of Ultrasound and Medical Applications

In medical ultrasound, transducers or probes that convert electrical energy to vibrational energy are used to generate the ultrasound pulse [38, 41]. These probes contain many piezoelectric crystals that start to vibrate under an applied electric current. The vibration of the crystals creates alternating pressure waves which propagate through the tissue. With imaging modes, these piezoelectric crystals also detect the reflected waves, and thus, an image of the tissue is generated.

Medical ultrasound devices operate in a range of 1-20 MHz which is way above the upper limit of human hearing at 20 kHz [41]. For imaging purposes, higher frequencies are used to image superficial structures and lower frequencies are used to image deeper structures within the tissue. This is due to the attenuation of the higher frequency being larger than lower frequencies at longer distances. The one-dimensional attenuation of an ultrasound wave is given by Equation 2.4 where I_0 is the intensity of the ultrasonic wave at $x=0$, α is the absorption coefficient given by the medium, x the propagation distance and I is the resulting wave intensity [39].

$$I = I_0 e^{-2\alpha x} \quad (2.4)$$

A mechanical index (MI) was defined as a safety measure at the start of using ultrasound in diagnostics and is described as the likelihood that the ultrasound can cause adverse biological effects [42, 43, 44]. It is a measure of the power of an ultrasound beam and an indicator for possible non-thermal bioeffects like cavitation and acoustic streaming. MI is calculated by Equation 2.5 where P_r is the peak rarefactional pressure and f is the frequency. Frequencies are around 1 MHz for therapeutic applications like ablation and focused ultrasound for increased drug delivery [39].

$$MI = \frac{P_r}{\sqrt{f}} \quad (2.5)$$

2.5.3 Biophysical Effects of Ultrasound

Ultrasound can generate thermal and mechanical effects in tissues [39, 10]. When the ultrasonic pressure waves propagate through tissue it is attenuated and this is the result of either absorption or scattering. Absorption is when the loss of energy is transformed into heat in the tissue and scattering is when the pressure wave's propagation direction is changed. Mechanical effects include acoustic radiation force and cavitation. The acoustic radiation force arises from the transfer of energy locally to the tissue and can cause acoustic streaming, shear stresses, and displacements of tissue. Cavitation is the mechanism where the ultrasound affects gas bubbles in the tissue making them oscillate from expansion at low local pressure to contraction at higher local pressures. There are usually few naturally occurring gas bubbles or vapors in tissues, and a high MI is required to generate cavitation effects. Therefore, to take advantage of this cavitation effect in drug delivery, MBs are injected into the bloodstream. The MBs injected are often well-known ultrasound contrast agents (UCA) from ultrasound imaging, usually comprised of gas stabilized with a lipid shell. When combining focused ultrasound with microbubbles (MBs) the frequency should correspond to the resonance frequency of the MBs [43]. In imaging, the ultrasound uses the echogenic properties of the MBs which produce a strong backscattered ultrasound that is detected by the transducer [8].

These mechanical effects generated from the ultrasound, can be used to increase drug delivery through several different mechanisms shown in Figure 2.3 [37, 10, 42, 8]. The acoustic streaming resulting from the acoustic radiation force can move MBs closer to the blood vessel wall. At lower acoustic pressures, the MBs will oscillate linearly and symmetrically. This is called stable cavitation. If the MBs oscillate at the endothelial wall this can cause the pulling and pushing of the cell membranes and cell-cell junctions. The stable oscillations also produce circulating fluid flows around the bubble, and these are called microstreams. The increased velocities in these microstreams can transport drugs around in the surrounding fluids at high velocities, but more importantly, create high viscous shear stresses at the MB surface. These shear stresses can also result in push-pull effects on the endothelial cells, create small pores, and can enhance endocytosis. In addition, the shear stresses can rupture drug carriers when they exceed the strength of the carrier vesicle. At higher acoustic pressures, the MBs will not be able to oscillate symmetrically due to the inertia of the gas within the bubbles causing a pressure build-up inside the bubble. When the inside pressure becomes too large the MB will collapse and this is called inertial cavitation. This collapse can cause shock waves around the MB and microjets that pierce rigid surfaces like the blood vessel wall. This can result in the creation of pores in the blood vessel wall and cell membrane which trigger extravasation events of the drug bursting into the tumor interstitium. These effects could all contribute to the transfer of drugs

from the blood vessels, through the ECM-rich tumor interstitium, and finally to the cancer cells. Some reports also theorizes that these cavitation events could change the local perfusion and modify the ECM structure and composition.

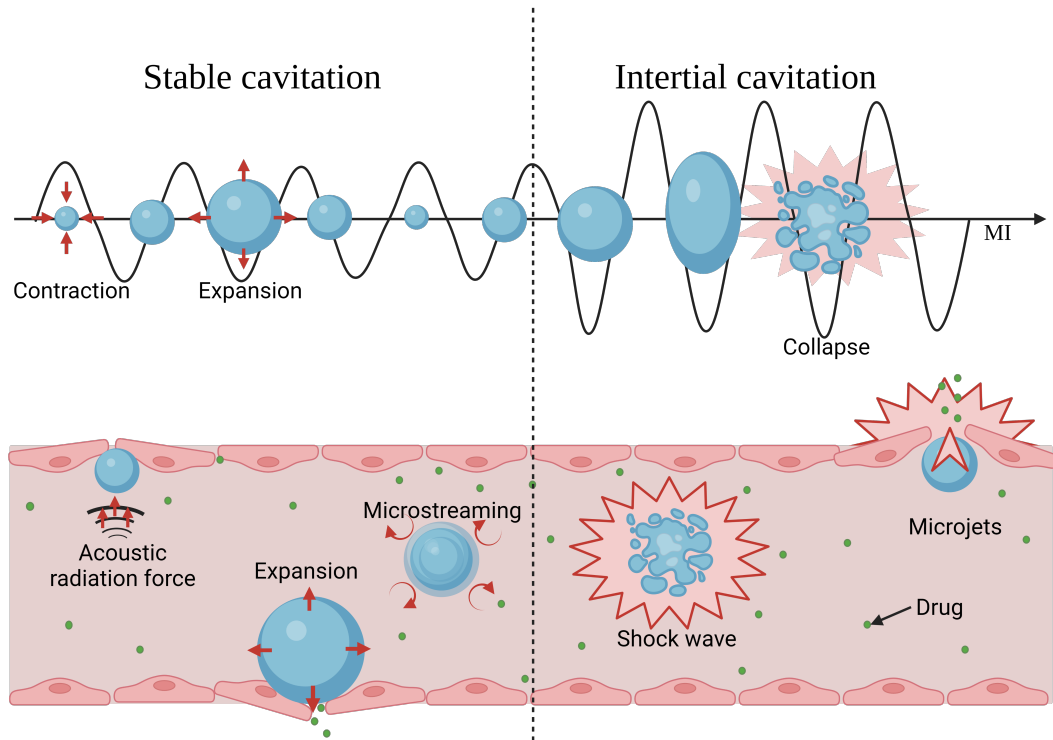


Figure 2.3: Biophysical effects of acoustic radiation force and cavitation in a blood vessel with a drug in circulation when using ultrasound and microbubbles. Stable cavitation effects are illustrated on the left of the figure and include expansion(oscillation) and microstreaming. Inertial cavitation effects are illustrated to the right of the figure and include shock waves and microjets. The figure is adapted from Liu et al. [8] and Årseth [45]. Created in BioRender.com

2.6 Staining of Biological Components

When looking at cellular components, regular bright-field microscopy may not yield a good enough contrast to isolate and identify these structures [46]. To improve the contrast some sort of staining or labeling of the components must be used. Some stains have colors that are visible to the eye, like histochemical staining techniques which use several chromatic and opaque labels. For even greater contrast, fluorescent probes can be used in conjunction with fluorescence microscopy [11]. These fluorophores are molecules that have the ability to emit fluorescent light with a specific wavelength

when excited at a specific wavelength. More on this mechanism in Section 2.7.1.

2.6.1 HES Staining

Hematoxylin and eosin (H&E) staining have been used for a long time to differentiate between tissue types and morphological changes in pathological tissues [47]. Hematoxylin stains nucleic acids and has a deep blue-purple color. Eosin stains proteins pink and is non-specific when it comes to which proteins. In a typical H & E-stained tissue section, the nuclei will be blue while the cytoplasm and ECM will have varying degrees of pink coloration. This is useful because the nuclei will show varying cell types and specific patterns of heterochromatin condensation which is important in cancer diagnostics. The downside to H&E staining, however, is its incompatibility with fluorescent staining.

When using H&E stain one of the disadvantages is that it is difficult to distinguish between muscle and connective tissue. For this saffron dye has been included as a staining agent because of its ability to bind to collagen with its characteristic deep orange color [48, 49]. With hematoxylin-eosin-saffron (HES) staining, it is easier to distinguish between tissues in a section and this is beneficial for pathological analyses of the tissue.

2.6.2 Fluorescent Staining

Fluorophores are usually organic dyes like Fluorescein which emits green light but can also be inorganic dyes like quantum dots [46]. The fluorophores can bind directly to a region of interest or they can be conjugated to another highly specific identifier. DAPI for instance binds directly to DNA with its high specificity to AT sequences and gives a strong fluorescent signal when excited [50].

We want our fluorescent labels to have high affinity, high avidity, low cross-reactivity, high stability, and easy identification [46]. High affinity means the labeling binds strongly to the specific target, and washing steps for instance will not make the fluorophore detach. Avidity describes the number of binding sites on the target molecule for the label, so a high avidity means that the label can bind to several locations on the molecule and yield a stronger fluorescent signal. Low cross-reactivity means that the label has low levels of unspecific binding. The stability of a label is important to ensure that the fluorescence is acceptable after sample preparation and during the entire imaging process. Easy identification means that multiple techniques can identify the same label, so there should not be any ambiguity about whether a signal arises from a label or not.

Fluorophores that do not directly bind to cellular components are often conjugated to antibodies [11, 46]. Antibodies can be made in the lab to bind to virtually any cellular component, and these targets are called antigens. Thus, if the fluorophore is bound to an antibody it can be used to visualize any cellular components. An antibody has the shape of a "Y" where the lower line is the constant region and the two upper

lines are the variable regions that can be engineered to bind to a desired antigen. Each antibody generally has several binding sites for fluorophores as well, yielding a strong fluorescent signal. This staining process is called immunofluorescence, and it can be direct and indirect which is shown in Figure 2.4. Direct immunofluorescence is when the fluorophore is bound to the primary antibody which is engineered to bind to the antigen. There is less chance for cross-reactivity with a primary antibody, however, they are generally expensive and they have decreased affinity and avidity. Indirect immunofluorescence uses a primary and secondary antibody. The primary antibody attaches to the specific target and the second antibody which is conjugated with the fluorophore binds to the primary antibody. The secondary antibodies are more easily conjugated to different fluorophores. Several primary antibodies can attach to the specific target, and several secondary antibodies can attach to the primary antibodies. This concentrates the fluorescent signal at our target and we get a signal amplification effect.

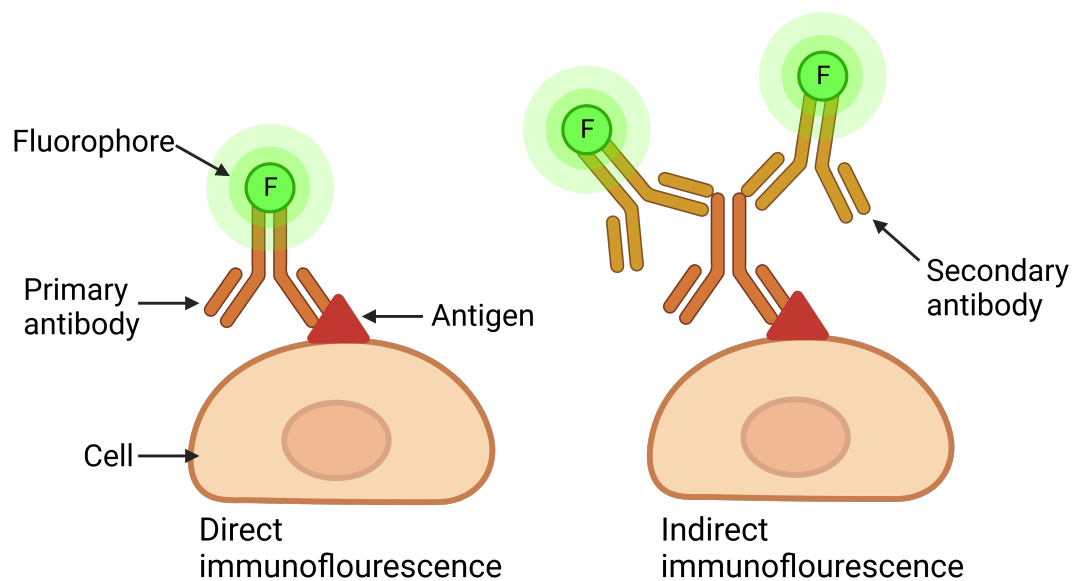


Figure 2.4: Schematic of direct and indirect immunofluorescence. In direct immunofluorescence, the primary antibody is conjugated to the fluorophore and binds to the target antigen. In indirect immunofluorescence, the fluorophore is conjugated to a secondary antibody which binds to the primary antibody and the primary antibody binds to the antigen. Created with BioRender.com

This indirect and direct immunofluorescence strategy can also be used with proteins

or other molecules with a high affinity for your desired antigen. For instance, one can use the highly specific binding between biotin and streptavidin which produces one of nature's strongest non-covalent interactions [51]. If the target antigen or the primary antibody is biotinylated, streptavidin will bind to it, creating a highly specific and strong bond.

2.7 Fluorescence Microscopy

2.7.1 Fundamentals of Fluorescence

Fluorescence describes the process where absorption of light leads to the excitation of an atom which in turn emits light when the molecule is in its relaxed state again [11]. Excitation explains the process where an atom absorbs a photon and this energy forces one of the ground-state electrons to jump to a higher energy state from S_0 to S_1 . Picoseconds after absorption, the electron will jump down again to its ground state and it is in this process of relaxation that a photon is emitted. Figure 2.5 a) shows an Jablonski diagram of this process.

The emitted photon will always have less energy than the incident photon, and thus, it will have a longer wavelength [52]. This difference in wavelength between the absorbed and emitted photon is called the Stokes shift. So, an absorbed photon in the blue range will likely emit a photon in the green range. In real life, fluorophores are not single-atom structures but molecules or compounds and the Stokes shift is highly dependent on each individual fluorophore's properties. Absorption only occurs if the incident light has a high enough energy to be able to excite the fluorophore to a higher energy state, and this energy corresponds to the difference in energy between the energy states.

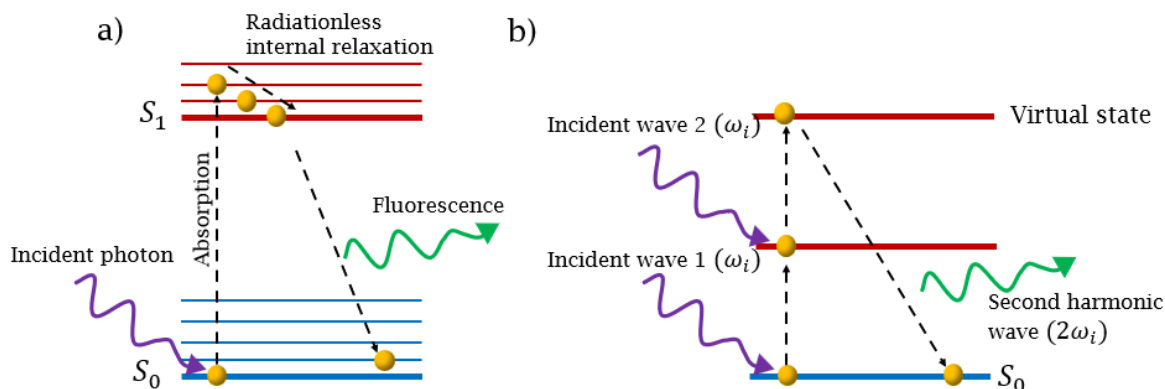


Figure 2.5: Jablonski diagram for fluorescence and second harmonic generation. a) shows an electron (yellow) in the ground energy state S_0 absorbing an incident photon which leads to the excitation of the electron to a higher energy level, S_1 . Internal radiationless relaxation follows between sublevels in S_1 before relaxing down to S_0 again. A photon is emitted whose energy is equivalent to the difference between the energy levels. b) shows this process for second harmonic generation. The electron absorbs two photons immediately after each other which excites it to a virtual state. When it relaxes again to its ground state the second harmonic is emitted. Adapted from Jerome [52]

2.7.2 Epi-Fluorescence Microscopy

Fluorescence microscopy images fluorescent samples against a dark background [11]. Epi-fluorescence microscopy specifically, is when this incident light beam illuminates the entire sample at the same time similar to regular wide-field light microscopy.

There are some important components that separate standard light microscopy and fluorescence microscopy, and these are shown in Figure 2.6 [53]. The first is a light source that produces light with a specific wavelength able to excite the desired fluorophore. It is important that this light source is able to maximally excite the fluorophore in order to get a signal that is distinguishable from background noise. These light sources are usually mercury arc lamps which are able to produce several peak-intensity wavelengths across the visible spectrum. After the light beam is created, the light beam goes through an excitation filter which only transmits light at a specific wavelength [11, 53]. With this, only the wavelength that excited the desired fluorophore is allowed to pass. Before the light beam hits the sample it hits the next critical component called the dichroic mirror which splits the beam into short wavelengths and long wavelengths. The short wavelengths are reflected down onto the sample and focused through the objective lens where they excite the fluorescent compounds in the sample. When the emitted light from the sample passes the dichroic mirror this is allowed to pass right through due to the longer wavelength. Before the detector or ocular, there is a final filter which is the emission filter. This filter further

ensures that only light created from the desired fluorophores is allowed through.

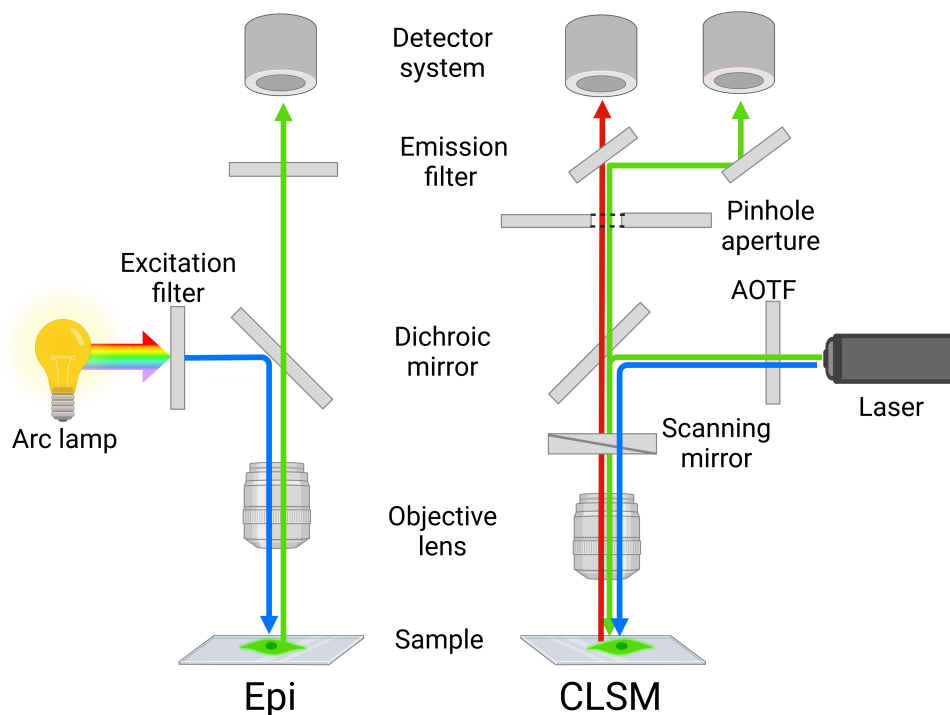


Figure 2.6: In the left schematic is the setup for epi-fluorescence microscopy with the arc lamp as a light source, excitation filter, dichroic mirror, objective lens, emission filter, and detector. Confocal laser scanning microscopy is the right schematic and includes the laser, acousto-optic tunable filter, dichroic mirror, scanning mirror, objective lens, pinhole aperture, emission filters, and detector system. Created with BioRender.com

2.7.3 Confocal Laser Scanning Microscopy

A confocal microscope share many of the same components as the Epi-fluorescence microscope as shown in Figure 2.6. The main feature of confocal microscopes is to illuminate small points in the sample one at a time, reject light from focal planes above or below these points, and then, use these point data to construct an image of the given sample slice [54]. The most critical component of a confocal microscope is the pinhole which grants the ability to reject fluorescence that originates from optical sections out of the focus point [54, 55, 56]. It is placed at the conjugate focal plane of the sample before the detector. When the pinhole is closed at one Airy unit (AU) it improves the lateral resolution when compared to epi-fluorescent microscopy. Opening the pinhole above one AU may increase blur and reduce contrast, but collects light from a larger optical section and thus, yields a stronger fluorescent signal. This pinhole

also makes it possible to image several optical slices of a sample and be able to do a 3D reconstruction of the sample which is called a z-stack.

In confocal laser scanning microscopy (CLSM), the illumination source is a laser beam as the name indicates [54]. Lasers are used because they provide a stable, uniform, and broad range of wavelengths without generating a lot of heat. The latest laser technology is white light lasers or supercontinuum lasers. They produce light by pulsing infrared light through a photonic crystal fiber which generates a constant energy distribution across the visible range. In this way, one can pick and choose the suitable wavelength at high precision using an acousto-optic tunable filter (AOTF) that is comparable to the emission filter in the epi-fluorescent setup described in the previous section.

After the laser beam wavelength has been filtered, it is reflected down onto the sample using a dichroic mirror as in epi-fluorescence. However, the laser is rapidly scanned across the XY-plane of the sample [56]. The scanning components are usually scanning galvanometer mirrors that direct the laser beam across the sample to create one optical slice [54]. The scanning is often done in a raster pattern across the sample which means moving the beam from one side to the other side from top to bottom [55]. It is important to consider the scanning speed since there are trade-offs between imaging speed, resolution, and field-of-view. Bi-directional scanning is one technique that can be implemented to increase the image acquisition speed [54].

Before hitting the sample, the laser beam passes through the objective lens. To ensure optimal imaging, these objective lenses should be immersion objectives that match the refractive index of the mounting media [54].

The emitted light is allowed to pass the dichroic mirror and continue through the pinhole. Before it hits the detector, there are several emission filters so several fluorophores can be imaged simultaneously [55]. These filters will sort the wavelengths to the appropriate detectors by reflecting the desired wavelengths up into the detectors. CLSMs usually have several detectors which include photomultiplier tubes (PMT) and GaAsP detectors. The GaAsP detectors have a higher sensitivity than the classic PMTs so a less intense illumination beam can be used which can be beneficial to avoid photobleaching of the fluorophores. There have also been developed new Power hybrid detectors (HyD) that use GaAsP photocathodes frontplates coupled with avalanche diodes which yield high performance and dynamic ranges for CLSM [57]. Detectors in CLSM do not recognize the specific wavelength of the signal, but they record the intensity which then can be translated into pixel values and these pixels make up an image [55].

2.7.4 Multiphoton Microscopy and Second Harmonic Generation

Multiple photons can be used to excite a fluorophore if the photons are absorbed simultaneously and their added energy corresponds to the needed excitation energy [55]. In practice, if multiphoton (MP) systems are used in microscopy it is usually with

two photons of equal energy, referred to as two-photon microscopy. If a fluorophore absorbs a photon there is a small window of about 10^{-18} s where another photon can contribute to the excitation. These two photons then become equivalent to a single photon with an energy equal to the sum of the two photons i.e. the same as half of the incident photons wavelength. The probability of two photons hitting a fluorophore simultaneously is dependent on the photon density of the illumination source and needs to be about a million times greater than for single-photon excitation. To be able to ensure this high photon density without damaging the sample or the fluorophore, the MP lasers are pulsed at incredibly short durations in the femto-to-pico second range. One advantage to two-photon excitation is fluorescence will only originate from the focal point since the photon density is too small outside the focal point. Thus, a better resolution and minimized photodamage can be obtained compared to the single-photon CLSM. Also, since shorter wavelengths attenuate faster than longer wavelengths in tissue, MP microscopy can image thicker samples and deeper in tissue.

Second harmonic generation (SHG) is a non-linear optical phenomenon where two photons with identical energy/wavelength can interact simultaneously with a specimen and a photon with an energy equal to the sum of the incident photons is generated without any energy loss [52]. This is illustrated in Figure 2.5 b).

With a multiphoton microscope, one can achieve second harmonic generation (SHG) which can be used to image collagen fibers in tissue samples [58]. Collagen is able to generate an SHG signal because it has a permanent dipole moment, and it has a non-centrosymmetric structure at the scale of the incident wavelength. This arises from the collagen helixes consisting of 3 α chains per turn which means that there is no symmetry along the lengthwise axis of the helix. Both type I and II collagen share this same property, and can be imaged with SHG. It has also been found that collagen has a Forward (SHGF) and Backward (SHGB) signal. Where the SHGF signal predominantly is generated from ordered longer fibers in the axial direction of the illumination beam, and the SHGB signal is generated from smaller more random structures with a non-axial orientation. Determining the SHGF/SHGB ratio can be property to describe the organization of collagen in a sample whether it is mostly ordered or random.

Chapter 3

Materials and Methods

3.1 Materials

3.1.1 Cell Lines and Cell Culture Chemicals

- 4T1 cancer cells (CRL 2539, American Type Culture Collection ((ATCC)) cultured in RPMI 1640 Medium (30-2001, ATCC) in 10 % fetal bovine serum (FBS) (F7524, Sigma Aldrich) supplemented with 1% penicillin streptomycin (P0781, Sigma Aldrich).
- KPC cancer cells (PDAC, Department of Radiation Oncology at the Massachusetts General Hospital) cultured in Dulbecco's Modified Eagle Medium (Gibco™ 11960-044, Thermo Fisher Scientific) with 10% FBS (F7524, Sigma Aldrich) , 1 % penicillin streptomycin (P0781, Sigma Aldrich) and 0.5 % L-Glutamine (G7513, Sigma Aldrich).
- CT26 cancer cells (CRL-2638, ATCC) cultured in RPMI 1640 Medium (30-2001, ATCC) in 10 % fetal bovine serum (F7524, Sigma Aldrich) supplemented with 1% penicillin streptomycin (P0781, Sigma Aldrich).

Cells were kept under exponential growth conditions in 75 cm^2 flasks at 37 °C with 5 % CO₂. CT26 and 4T1 cells were seeded at 1:20-1:30 ratios, while the KPC cells were seeded at 1:10-1:20 ratios.

3.1.2 Chemicals

Ultrasound and microbubble treatment

- 20 mM liposomes with ATTO680 and ATTO633 (Courtesy of SINTEF, Sjoerd Hark)
- SonoVue Microbubbles (Bracco)
- 2 mg/mL Fluorescein-lectin (FL-1171, Vector Laboratories Inc)

Staining chemicals

- Phosphate Buffered Saline (SLCL7026, Sigma-Aldrich)

- Acetone (STBK4453, Sigma-Aldrich)
- 10% Fetal Bovine Serum in PBS (F7524, Sigma-Aldrich)
- Hydrophobic PAP pen for immunostaining (3110, Sigma-Aldrich)
- Avidin in Dako blocking kit (ZE0917, Vector Laboratories Inc)
- Biotin solution in Dako blocking kit (ZE0917, Vector Laboratories Inc)
- Hyaluronic acid binding protein, Bovine Nasal Cartilage, Biotinylated (3993082, Sigma-Aldrich)
- Cy3-streptavidin (2471901, Thermo Fischer Scientific)
- Vectashield Vibrance with DAPI (ZK0310, Vector Laboratories Inc)

3.1.3 Equipment

Ultrasound and microbubble treatment

- Ultrasound transducer 1MHz (Imasonic SAS, Voray sur l'Ognon, France)
- Oscilloscope (LeCroy Wavesurfer 44 Xs, Teledyne LeCroy, Chestnut Ridge, NY, USA)
- 5 MHz transducer (V307-SU, Olympus)
- 50 db power amplifier (2100 L from Electronics and Innovations Ltd., Rochester, NY, USA)
- Signal generator (33500 B, Keysight Technologies, Santa Rosa, CA, USA)
- Pearl Impulse Small Imaging System (LI-COR Biosciences, Lincoln, NE, USA)

Confocal microscopes

- TCS SP8 Leica Microsystems Confocal Microscope
- LSM 800 Zeiss Confocal Microscope

3.2 Methods

3.2.1 Tumor Cell Implantation

Cell suspension for implantation was prepared by centrifuging for 5 min at 1500 RPM, removing the supernatant, and then adding cell medium to the desired concentration. For 4T1, the injection volume was 50 μ L containing 10 000 cells, and for

CT26 it was 50 μ L containing 100 000 cells. The KPC injection volume was 20 μ L containing 200 000 cells. The cell suspensions were injected subcutaneously in the right hind leg of BALB/c mice for the 4T1 and CT26 tumor cells, and in B6/albino mice for the KPC tumor cells. A total of 42 animals were included in this study with 14 mice for each of the tumor models. Within each tumor model group, 7 mice were in the control group and 7 in the treated as can be seen in Table 3.1. Around 14 days after implantation, most tumors had reached the desired size and ultrasound and microbubble (USMB) treatment commenced. The day before the USMB treatment, the tumors were imaged by Contrast-Enhanced Ultrasound for another project. This will not be discussed in this work.

Table 3.1: Overview of the number of animals in this study, and the number of animals in each group.

	4T1	CT26	KPC
Control	7	7	7
USMB Treated	7	7	7
Total	14	14	14

3.2.2 Pearl Epifluorescent Imaging

During all experiments and treatments at the animal facility, the mice were anesthetized with 2.5 % isoflurane per 1 L/min medical air either in a small gas chamber or from an inhalation tube. To begin with, the mice were all given a tail vein catheter.

To study the uptake of the fluorescently labeled liposomes, the mice were imaged in the Pearl whole-animal scanner where the fluorescence intensity from the NPs in the animal was measured. A laser wavelength of 685 nm was used to excite the ATTO 680 in the liposomes, and this generated emission at 720 nm which was detected in the whole-animal scanner.

A sequence of images was taken at different time points with the whole-animal scanner. The first image was taken before the injection of nanoparticles to be able to subtract the background/autofluorescence from the images. Then, all the mice were injected with 50 μ L of the liposome solution through the tail vein catheter and imaged immediately. After this, the animal was moved for ultrasound treatment. In addition to these two images, the animals were imaged directly after the ultrasound treatment, 4 hours after the treatment, and 24 hours after the treatment. This sequence is summarized in Figure 3.2.

3.2.3 Ultrasound and Microbubble Treatment

As mentioned, there was one USMB treated group and one control group for each of the three tumor models. The treated group received microbubble (MB) injections with the ultrasound turned on, while the control group received MB injections with

the ultrasound turned off.

The mice were placed onto the ultrasound rig with their right hind leg in a water tank filled with degassed water heated to 34 °C. At the bottom of the water tank was the ultrasound transducer. A simplified schematic of the ultrasound rig can be seen in Figure 3.1. The leg with the tumor was submerged in the water because the ultrasound needs a denser medium than air to propagate through. To ensure good circulation in the blood vessels and for the mice's comfort, a heating lamp was placed above the ultrasound rig. In addition, aquarium warmers were used to keep the water at 34 °C.

To initiate the treatment, 50 μ L MBs (SonoVue) were injected through the tail vein catheter and simultaneously the ultrasound was turned on. An ultrasound frequency of 1 MHz was used together with a pulse repetition frequency (PRF) of 0.25 Hz, 10 000 cycles, and a mechanical index (MI) of 0.50. Two subsequent injections of 50 μ L SonoVue were given at 3 and 6 minutes. The treatment lasted 3 minutes after the last injection for a total of 9 minutes.

A cavitation detection transducer in conjunction with a custom script was used to visually confirm the oscillations of microbubbles in the tumor. This data is not presented in this work.

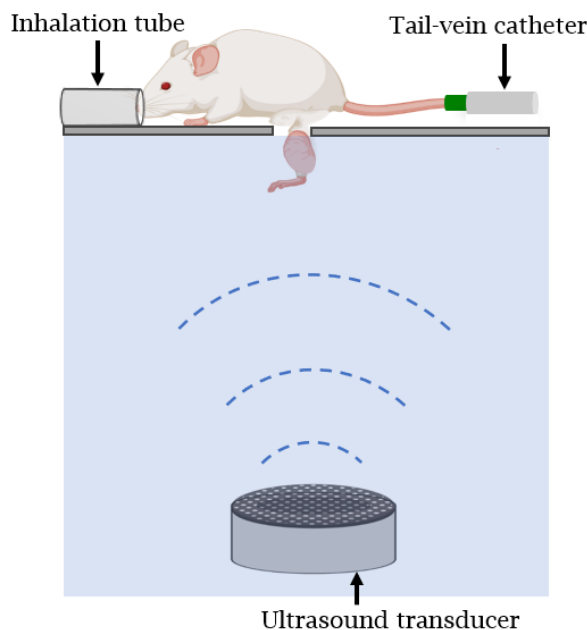


Figure 3.1: Schematic overview of the ultrasound and microbubble treatment set-up. The mouse lay on top of a water tank with the tumor-implanted leg submerged in the water. An ultrasound transducer sat in the bottom of the tank. To keep the mouse anesthetized, its snout was put into an inhalation tube where it received anesthetics. A tail-vein catheter was used to inject the microbubbles during the ultrasound treatment. Parts of the Figure created with BioRender.com

3.2.4 Tumor Harvest and Sectioning

24h after treatment, the last image was taken in the Pearl imaging system and the mice were injected with 50 μ L Fluorescein-lectin (FITC-lectin). The mice were euthanized 5 min after injection and the tumor, heart, lungs liver, spleen, and kidneys were surgically harvested from each mouse. These organs and the tumor were subsequently imaged in the Pearl scanner, ex vivo. Then, the tumors' length, height, width, and weight were measured. To store the tumors, they were flash-frozen in liquid nitrogen on a cork plate. The tumors were then sent to the Cellular and Molecular Imaging Core Facility (CMIC) which sectioned the tumors and deposited them on microscope slides. Each tumor was sectioned into three different levels 500 μ m apart. One level contained 11 different sections with a thickness of 8 μ m. 10 of the sections were left unstained while the 11th section was HES stained at CMIC. For this work, sections 8 and 9 from the second level were used with section 10 as a backup.

After receiving the sections, the unstained sections were stored at -80 $^{\circ}$ C while the HES stained sections were stored at 4 $^{\circ}$ C.

Cell culturing, implantation, USMB treatment, and harvest were performed by Caroline Einen and Sofie Snipstad. In addition, Einar Sulheim and Veronica Nordlund assisted with the USMB treatment and the whole animal Pearl imaging. The author assisted during the USMB treatment with logistics and various tasks. All animal experiments were approved by the Norwegian Food and Safety Authority.

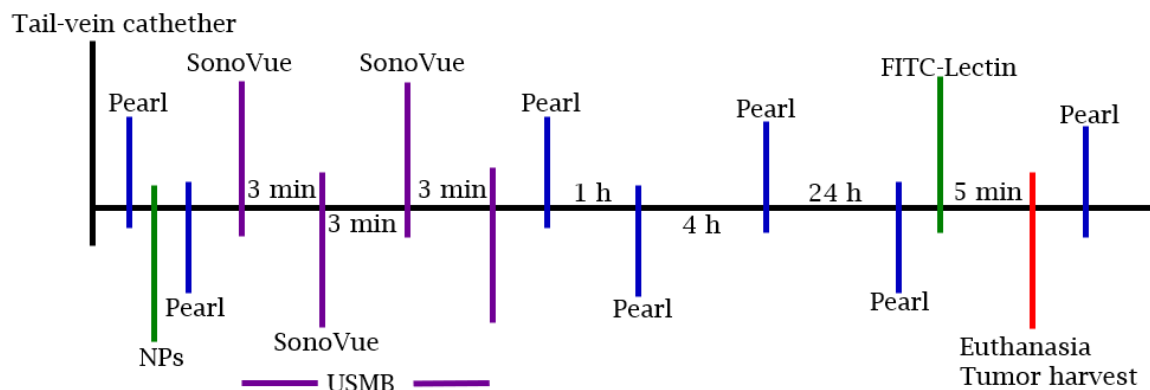


Figure 3.2: Timeline of the treatment and imaging. NPs, SonoVue and FITC-lectin denote injection of these into the mice. A blue line describes imaging of the biodistribution of the liposomes in the Pearl whole-animal scanner. Purple lines denote the injection of microbubbles during the USMB treatment, and green lines denote the injection of NPs and FITC-lectin. The red line describes the time point of euthanasia and tumor harvest.

3.2.5 Hyaluronic Acid Immunofluorescent Staining

To image the hyaluronic acid (HA) in the tumor sections, the HA was labeled by indirect immunofluorescence using biotinylated HA-binding protein (HABP) and Cy3 conjugated secondary antibody. Cy3 was conjugated to streptavidin which binds with high specificity to biotin, and thus to the biotinylated HABP.

The staining process started with thawing the tumor sections in RT for 3-5 min. Thereafter, the sections were immersed in PBS for 2 min to rehydrate the sections. Immediately after the rehydration, the sections were fixated by immersing them in - 20 °C Acetone for 10 min. Then, they were immersed again in PBS for 5 min to remove excess Acetone.

When the slides were dry, the tumor sections were encircled using a hydrophobic PAP pen. To ensure specific streptavidin-biotin conjugation, endogenous biotin, avidin binding sites, and biotin receptors were blocked using the DAKO blocking kit. Firstly, the sections were covered with the DAKO Avidin solution and incubated for 15 min. Then, they were briefly immersed in sterile PBS to wash off the solution. Secondly, the sections were covered with the DAKO biotin solution and incubated for 15 min before another brief immersion into sterile PBS. Lastly, the sections were incubated with a blocking solution for 1 h. The blocking solution was 10% Fetal Bovine Serum (FBS) diluted in PBS and was used to ensure that all biotin sites were blocked. Due to large differences in the size of the sections, different volumes of the blocking solutions were needed to cover the sections. Generally, the KPC sections needed about 100 μL whilst the 4T1 sections needed about 100-200 μL and the CT26 needed at least 200 μL . This also applied to the volume of HABP solution and Cy3-streptavidin solution needed.

The HABP was diluted by the manufacturer's instructions and aliquoted into 12 μL volumes with a concentration of 500 $\mu\text{g}/\text{mL}$ HABP. For incubation, one aliquot was diluted with 363 μL of the blocking solution to a concentration of 16 $\mu\text{g}/\text{mL}$. Sections were subsequently incubated overnight for at least 12 h at 4 °C in a lightproof box covered with aluminum foil and containing a damp paper towel.

The next day, the sections were washed by immersing them in sterile PBS for 3 min 3 times. Cy3-streptavidin was diluted in a 1:200 ratio with 10% FBS in PBS to a concentration of 7.5 $\mu\text{g}/\text{mL}$. Thereafter, the sections were incubated with the Cy3-streptavidin solution for 1 h at RT in a lightproof box covered with aluminum foil. When the incubation period was over, the section was washed in PBS 3 times for 3 min each time. After the sections were dry, they were counterstained with 8-10 μL Vectashield Vibrance with DAPI. A coverslip size no 1.5 was gently placed atop the section and after 1 h in RT the sections were ready for imaging in the CLSM.

3.2.6 Confocal Laser Scanning Microscope Imaging

The CLSM used for the imaging of the tumor sections was the Leica SP8 MP/SMD Confocal microscope. It was used together with the software, Leica Application Suite X (LAS-X). A condenser lens with a numerical aperture (NA) of 0.90 was used to ensure

a good signal for the forward scattered second harmonic generated (SHG) signal. The condenser lens system was lowered closer to the sample to collect as much transmitted light as possible. For the objective lens, a 25X water immersion objective with an NA of 0.95 was used. In addition, a filter cube with a 425 nm dichroic mirror, and a 390 and 445 nm filter was used. Before imaging sessions, the microscope was adjusted for Köhler for optimal illumination of the sample. All scans were also made using bidirectional scanning.

Fluorophores

Table 3.2: Overview of the fluorophores used in this work, their absorption, and emission maxima. What biological components they are staining for is also included.

Fluorophore	Stains	Absorption Maxima [nm]	Emission Maxima [nm]
FITC-lectin	Blood vessels	495	515
ATTO 633	Nanoparticles	630	651
CY3	Hyaluronic acid	552	565
DAPI	Nucleic acids	358	461

Hyaluronic Acid, Nucleic Acids, and Collagen imaging

To image the hyaluronic acid (HA), nucleic acids, and collagen, tile scans were taken of the tumor sections. For this part of the experiment, the samples were prepared as described in Section 3.2.5. The tile scans were taken separately, but in quick succession with the Cy3 channel first, then the DAPI channel second, and the SHG channel last.

The first tile scan was of the Cy3 fluorophore that indirectly stained the HA and it was excited by the white light laser (WLL) at 552 nm at 15 % laser intensity. A photomultiplier tube (PMT) detector with a range from 560-640 nm was used with a 725 V detector gain. In addition, Line Averaging was set to 2 and the pinhole was 2 airy units (AU). A line average of 2 means that the laser scans the same line twice and takes the average signal and increasing the pinhole size increases the optical section. 2 AU corresponds to a pinhole opening of 111.71 μm and an optical section of 3.07 μm .

The second tile scan was the imaging of the DAPI-stained nucleic acids which were excited by the multiphoton (MP) laser at 780 nm at 45 % intensity. To detect the DAPI signal, the pinhole was opened to the maximum. An internal PMT detector was used with a detection range of 435-485 nm and a detector gain of 850 V. A Line Average of 2 was also used here. Since the MP laser can generate a lot of heat and possibly boil the sample, an intensity experiment was done for the MP laser intensity. 45 % was the lowest laser intensity with an acceptable DAPI signal and no boiling was observed, so it was chosen for the tile scans.

The third tile scan was the imaging of the collagen fibers using the second harmonic generation (SHG) signal. An MP laser with a wavelength of 890 nm with a 15 %

intensity was used. The forward (SHGF) and backward (SHGB) SHG signals were detected using PMTs and hybrid detectors (HyDs), respectively. The PMT detector had a detector gain of 750 V while the HyD detector had a gain of 100 %. Due to the HyD detectors shutting down if the signal is too intense, a Linear Accumulation of 6 was used. This means that the laser scans the same line 6 times and adds the signal on top of each other to create the image. A summary of the settings for these three tile scans can be found in Table 3.3.

Table 3.3: Overview of the CLSM settings and sequence for the hyaluronic acid, collagen, and nucleic acid tile scans.

Sequence	Laser	Detector	Pinhole	Additional
1. Cy3	552 nm 15 %	560-640 nm 725V	2 AU	Line Avg 2
2. DAPI	780 nm 45 %	435-485 nm 850V	10.38 AU	Line Avg 2
3. SHGF	890 nm 15 %	445 \pm 10 nm 750V	1 AU	Line Acc 6
3. SHGB	890 nm 15 %	445 \pm 10 nm 100 %	1 AU	Line Acc 6

Before starting the tile scans, successful HA and nucleic acid staining was checked using the Epi-fluorescent mode. A filter cube with 525-565 nm excitation and 572-647 nm emission specters was used to check the Cy3 staining, and a filter cube with 340-380 nm excitation and 425 nm emission was used to check the DAPI staining. Thereafter, 4 points were marked to outline the entire tumor section. In the tile scan mode, each point you mark will make a grid between the marked points. After the entire section was included in the tile scan grid, 30-60 focus points were marked in the tumor section using the Epi-fluorescent mode with the filter cube corresponding to the Cy3. When marking these focus points, all points included tumor tissue, had minimal air bubbles, and were evenly distributed across the section.

After all the focus points were marked, they were manually focused in the CLSM live mode with the Cy3 channel by adjusting the z-position of the objective turret. 512x512 pixels and 400 speed were used for each tile in the tile scan. This corresponds to a pixel size of 0.91 μm^2 . Imaging of the entire section ensued and then the focusing step was repeated for the DAPI channel and lastly for the SHG. Since the water objective was used, it was important to always check the water droplet between each tile scan and add water to avoid evaporation.

Blood Vessel and Nanoparticle Imaging

The tumor sections used for the blood vessel (BV) and nanoparticle (NP) imaging were not HA stained to make sure that the repeated washing steps did not wash out the NPs from the sections. Therefore, the samples were prepared by thawing them for 3-5 min in RT before they were counterstained with 8-10 μL of Vectashield Vibrance with DAPI. A no. 1.5 coverslip was gently placed atop each section. After 1 h in RT, the sections were ready to be imaged.

For the BV and NP imaging, five images were taken in three sequences using the Mark and Find experiment tool in the LAS-X software. The first sequence was

imaging the BV and the NPs which were stained with the FITC-lectin and ATTO 633, respectively. FITC-lectin was excited with the WLL at 491 nm with a laser intensity of 35 %. The detector range for the FITC-lectin signal was from 500-550 nm using a PMT with detector gain of 825 V. ATTO 633 was excited by the WLL at 630 nm with 30 % laser intensity. The detector range for the ATTO 633 signal was from 640-740 nm using a HyD with a detector gain of 125 %. A pinhole size of 2 AU and Line averaging of 2 were used for both the FITC-lectin and the ATTO 633.

The second and third sequences were the DAPI and SHGFB sequences, respectively. The settings for these sequences were the same as described in the previous section. One important consideration was that the FITC-Lectin and ATTO 633 were the first sequence to avoid bleaching of the fluorophores by the MP laser. A summary of all the settings can be found in Table 3.4.

Table 3.4: Overview of the CLSM settings and sequence for the blood vessel and nanoparticle imaging. Sequence 1 contains the settings for blood vessel and nanoparticle imaging, sequence 2 contains the settings for collagen imaging, and sequence 3 contains the settings for nucleic acid imaging.

Sequence	Laser	Detector	Pinhole	Additional
1. FITC-lectin	491 nm 35 %	500-550 nm 825V	2 AU	Line Avg 2
1. ATTO 633	630 nm 30 %	640-740 nm 125 %	2 AU	Line Avg 2
2. SHGF	890 nm 15 %	445 \pm 10 nm 750V	1 AU	Line Acc 6
2. SHGB	890 nm 15 %	445 \pm 10 nm 100 %	1 AU	Line Acc 6
3. DAPI	780 nm 45 %	435-485 nm 850V	10.38 AU	Line Avg 2

To determine which areas to image, the epifluorescent image mode was used with a filter cube of 450-490 nm excitation wavelength and emission of 515 nm. This corresponds well to the FITC-lectin fluorescence spectrum. With the mark and find experiment function in LAS-X, FITC-lectin intense areas were marked for further inspection. Then, the filter cube was changed to 340-390 nm excitation and 425 nm emission which corresponds well with the DAPI spectrum, to look at the cell density. If the area had a particularly low nuclei density, it was deemed muscle or connective tissue and was omitted. At least 4 peripheral marks and 4 central marks were made. The periphery was defined as 10 % of the outer diameter of the tumor section, and the center was the rest. When all the marks were made, the microscope was switched to the CLSM mode.

In CLSM mode the best focus plane for the FITC-lectin and ATTO633 was found using the live feed with 512x512 pixels and 400 scan speed, and adjusting the z-position of the objective turret. This was done for all the marks, and when focus was achieved for all the points imaging ensued with 1024x1024 pixels and 100 scan speed. This corresponded to a pixel size of 0.45 μm^2 . Points that lacked a sufficient FITC-lectin or ATTO 633 signal in CLSM live mode were not imaged.

3.2.7 HES Imaging

To image the HES sections, the Zeiss 800 Airyscan Confocal microscope was used with the ZEN software. The images were taken using the CCD camera with a wide-field brightfield tile scan mode. An illumination voltage of 10.0 V was used for the images together with a 10 ms exposure time. Before imaging started the white balance was set for each section. A tile was determined by placing four points on the edges of the sections to create an imaging grid that included the entire section. A simple tilted focus map was created by creating four supporting focus points in the section. Then, the tile acquisition was initiated. After the tile scan was done, the images were stitched together using the processing tools in the ZEN software with a 10 % overlap between the tiles.

3.2.8 Image Analysis

All the image processing and analysis were done in FIJI [59] unless otherwise specified. FIJI is just ImageJ with additional plugins already installed. Macro scripts were created in Fiji to automate some of the image processing, and these can be found in Appendix C. Examples of images before analysis are given in Appendix B.

Pearl Scan Image Analysis

The images from the Pearl scanner were analyzed in FIJI. A region of interest (ROI) was drawn around the tumor and the mean fluorescence was measured. The mean fluorescence is the mean intensity value of the pixels within the ROI. This was done to all tumor images both in vivo, and ex vivo. Caroline Einen performed this image analysis and supplied the author with the raw data.

Area Fraction ROIs

To analyze the tile scan images ROIs, had to be made of the whole tumor section, the periphery, and the center. Many of the sections also had holes in them due to difficulties during the sectioning process, so the ROIs had to exclude these holes as well. For these considerations, an ImageJ protocol was made to create these ROIs using the DAPI image of the section.

Firstly, a loose ROI was manually drawn around the section and all pixels outside of the section were put to zero using the Clear Outside function. By looking at the HES sections, non-tumor tissue in the sections was removed by drawing around the areas and using the Clear function. This is demonstrated in Figure 3.3. Light pink areas like in Figure 3.3 a) were deemed muscle or connective tissue and were removed. White areas with low nuclei density could be necrosis or edema, but this is difficult to determine without a pathologist. So areas like 3.3 b) were not removed. Then, the pixel intensity range was set between 100-200 to increase the contrast. A Mean filter

with 50 pixels was then used to increase the light intensity from the tumor tissue and decrease the light intensity from the holes in the tissue. The image was subsequently thresholded using the Default thresholding algorithm, which created a binary image with light pixels for the tissue and dark pixels everywhere else. This image was made into a mask, and an ROI around the mask was made using the Create Selection tool. This total ROI followed the edges of the section and excluded any holes and bubbles from the ROI as seen in Figure 3.4 a).

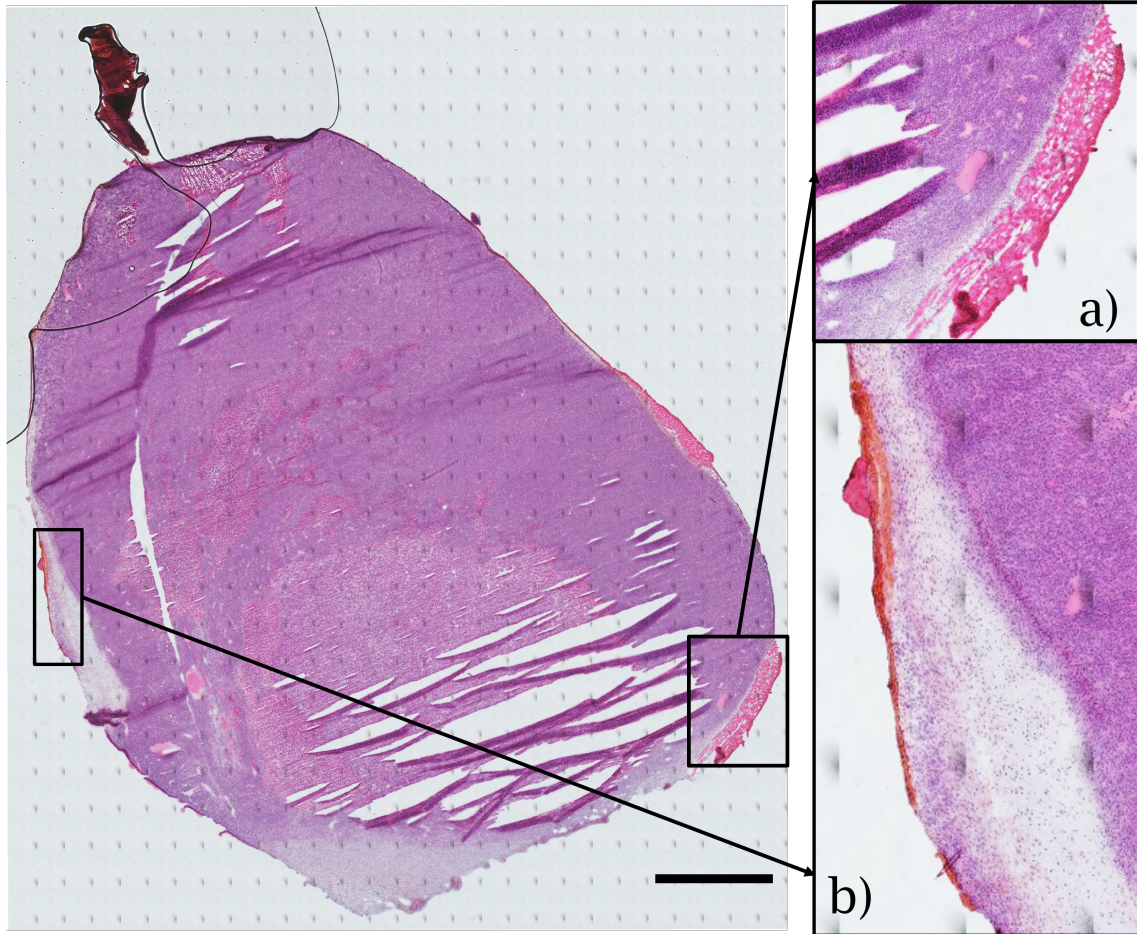


Figure 3.3: HES stained CT26 section tile scan image. Nuclei are colored purple, proteins are colored pink, and collagen is colored orange. a) Highlighted area of likely muscle or connective tissue in pink, that was omitted in the area fraction analysis. b) Highlighted area of possible necrosis or edema, that was not omitted in the area fraction analysis. Scalebar is 2000 μm .

To make the periphery and center ROI, the mask image was duplicated, and all the dark pixels inside the tumor tissue border were filled using the Fill tool. Then a selection was chosen which created an ROI of just the border of the tumor section. This was duplicated and scaled down to 90 % of its original size using the Scale function in ROI manager. This scaled-down ROI was then selected together with the total ROI,

and using the AND function the center ROI was created as can be seen in Figure 3.4c). To make the periphery ROI in Figure 3.4 b), the XOR function was used while the center and mask ROI were selected.

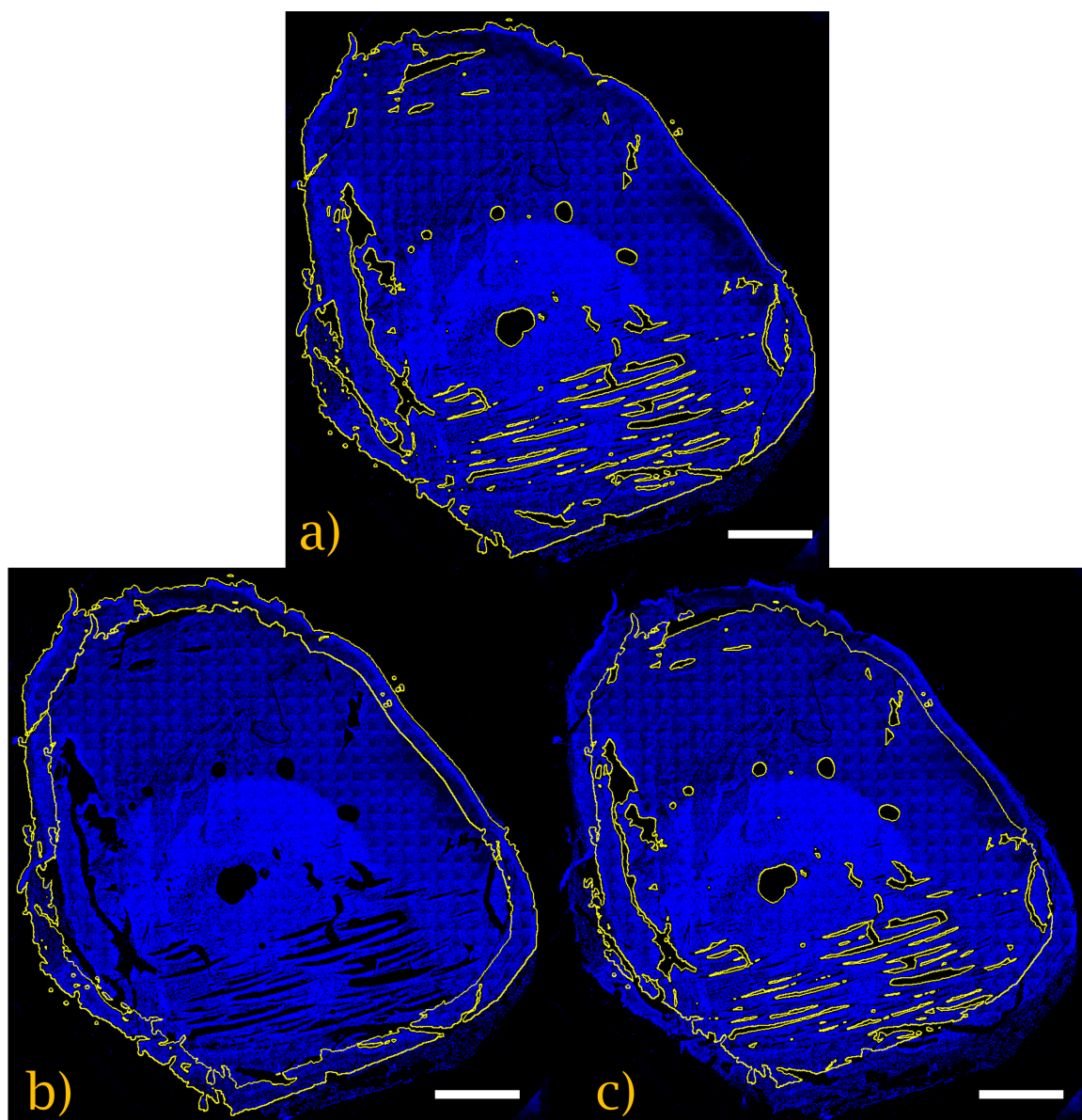


Figure 3.4: Overview of ROIs used for the area fraction analyses on a DAPI tile scan image of a CT26 tumor section. a) is the total ROI of the tumor section, b) is the ROI for the outer 10 % of the tumor section and c) is the ROI for the 90 % center of the tumor section. Scalebar is 2000 μm .

Hyaluronic Acid Area Fraction Analysis

To analyze the HA area fraction, the background was subtracted 10 pixels using the Subtract function. This value came from measuring the mean gray value of the background where there was no tissue. Thresholding followed, using the Default thresholding algorithm which gave the best result from to visual inspection. Then, measurements of the total, periphery, and center ROIs were done using the Measure function with Area fraction, Area, and Limit to threshold ticked off. A macro script was used for this image processing and can be found in Appendix C.1.

Collagen Area Fraction Analysis and FB Ratio

To analyze the collagen area fraction, the image channels were first split into the forward and backward signal using the Split Channel function. Then, to reduce noise a Median filter with 2 pixels was applied to the channels before thresholding the images using the Triangle algorithm which gave the best result from to visual inspection. Afterward, the area fraction of the total, periphery, and center was measured with the Measure function with Area fraction, Area, and Limit to threshold ticked off. A macro script was used for this image processing and can be found in Appendix C.2.

To analyze the forward-to-backward ratio of the SHG intensity, the images were opened anew and split into two channels. The forward channel was then divided by the backward channel using the Image calculator function with the 32-bit (float) ticked off. This created a new image where each pixel was the intensity of the forward signal divided by the backward signal. The total ROI was then added to ROI manager, and with the Mean Gray Value ticked off the Measure function was used. A macro script was used for this image processing and can be found in Appendix C.3.

Cell Density Analysis

To analyze the nucleic acid area fraction, the total, periphery, and center ROI was opened in the ROI manager. The image was thresholded using the Li thresholding algorithm which was found to produce the most reproducible signal-to-noise ratio for the images. Then, the sections were measured using the Measure function with Area fraction, Area, and Limit to threshold ticked off. This measurement was done for the total ROI, periphery ROI and center ROI. The area fraction of nucleic acids can be interpreted as the cellular density of the section, and for the rest of the report, cell density will be used. A macro script was used for this image processing and can be found in Appendix C.4.

NPs Extravasation Analyses

For the extravasation analyses, a macro script was used to process the images. In this macro script, the collagen channels and DAPI channels were closed leaving the BV and NP channels. Both the BV and NP channels were first processed with a Gaussian

blur filter with 2 pixels. This smoothed out the structures and reduced the noise. Then the images were thresholded with the Triangle and Renyi Entropy algorithms for the BV and NP images, respectively. One additional step for the BV image processing was filling any holes within the blood vessels with the Gray morphology tool with a diamond structure, radius of 10 pixels, and close function. A macro script was used for this image processing and can be found in Appendix C.5. 8-12 images per tumor section were used for this analysis and 18 sections were analyzed in total.

These two binary images were then input into a custom Matlab script found in Appendix C.6. This script identified the BVs and NP clusters and calculated the shortest border-to-border distance between the NP cluster and its nearest BV. This border-to-border distance will henceforth be known as the extravasation distance or the penetration distance into the tumor interstitium. The area of the NP cluster was calculated in μm^2 . The resulting data was exported into a pivot table in Excel. Before plotting, NP clusters co-localized with the BVs were removed from the analysis since their extravasation distance is 0. The mean extravasation distance for each section was calculated using the Pivot table. To determine the fraction of NP clusters at different distances from the BVs, the Pivot table was used to group the NPs with distances from 0-200 μm in 10 μm bins. Distances above 200 μm were deemed to have originated from either unstained or out-of-frame BVs. The percentage of the total area of the NPs in each bin was calculated to get the fractions at the distances.

As described earlier in Subsection 3.2.6, images of the SHGFB and DAPI signal were taken together with the NP and BV images. These were not quantitatively analyzed. The DAPI images were used to evaluate whether the images were taken from a muscle or connective tissue, and if so, the image sequence was omitted. The SHGFB images were not used because the sequences were manually focused for optimal BV and NP imaging, and thus, some of the SHG images were somewhat out-of-focus.

Statistical Analyses and Plotting

All statistical analyses and plots were made using the GraphPad Prism software. All data sets were tested for normality using D-Agostino-Pearson and Shapiro Wilk tests with a $p \leq 0.05$. Then, Brown-Forsythe and Bartlett's tests were done with a $p \leq 0.05$ to determine if the groups had significantly different standard deviations. For the groups with a Gaussian distribution, and equal standard deviations an ordinary one-way ANOVA test with a $p \leq 0.05$ was performed. In addition, Tukey's multiple comparison test with $\alpha \leq 0.05$ was used to compare the means of the groups. If the groups had a Gaussian distribution, but with significantly different standard deviations a Welch and Brown-Forsythe ANOVA with $p \leq 0.05$ was performed with a Dunnett's T3 multiple comparison test with $\alpha \leq 0.05$. For data sets that did not pass the normality test then, a Kruskal-Wallis test was performed with $p \leq 0.05$ and Dunn's multiple comparisons test with $\alpha \leq 0.05$. In the plots, statistical significance is denoted by asterisks.

To assess the correlation, the Pearson Correlation Coefficients were calculated if the data had Gaussian distributions. If the data did not have a Gaussian distribution,

then the Nonparametric Spearman correlation test was done in stead. Table 3.5 shows how Prism denotes different levels of significance with p-values corresponding to a number of asterisks.

Table 3.5: This table shows how Graphpad plots the statistical significance using asterisks.

Symbol	Meaning
*	$p \leq 0.05$
**	$p \leq 0.01$
***	$p \leq 0.001$
****	$p \leq 0.0001$

Chapter 4

Results

4.1 Characterization of Tumor Models

The area fractions in this section are presented for the entire section denoted as total, the periphery, and the center of the sections. This corresponds to the ROIs shown in Figure 3.4. The area fractions are sometimes discussed as amounts, contents, or densities of the different constituents for better readability, but more precisely the area fractions denote the percentage of light pixels originating from the fluorophores or second harmonics in an area. In addition, we assume that the SHG signal originated exclusively from collagen and thus, SHG and collagen will be used interchangeably when regarding the area fraction of collagen.

4.1.1 Hyaluronic Acid Area Fraction

From Figure 4.1 the area fractions of HA in the imaged tumor sections are presented. There was a significant difference between the means for the total amount of HA in the CT26 tumor sections compared to the KPC sections. In addition, there was an even more significant difference in the HA content between the center of the CT26 and KPC sections. A trend shared by the 4T1 and CT26 sections was that the periphery had the highest amount of HA. The means between the total, periphery, and center were more similar for the KPC sections than for the 4T1 and CT26. Data for the plot can be found in Table A.2.

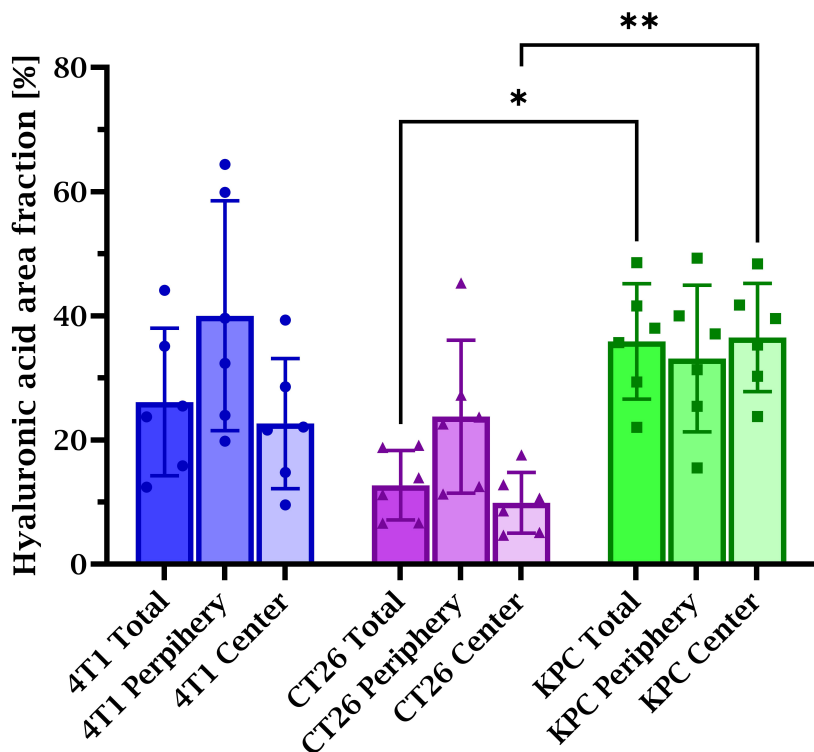


Figure 4.1: Area fraction of hyaluronic acid in 4T1, CT26 and KPC tumor sections. For each tumor model, the area fractions from the entire tumor section (total), periphery, and center are shown. Each point denotes individual tumor sections' area fractions, the bar denotes the mean between these points and the whiskers denote the standard deviation. These measurements come from 1 section per tumor of 6 different tumors from each of the tumor models, summing up to 18 tumors. Asterisks denote statistical significance between groups.

4.1.2 Collagen Area Fraction

The area fraction for both the forward and backward SHG signal can be found in Figure 4.2. Trends observed in the forward signal and backward were very similar, so they will be discussed together. The difference was that the area fractions for the backward signal were marginally higher. A trend is that many of the KPC tumor sections had a higher area fraction of collagen than the 4T1 and CT26 sections. However, it was not significant. The standard deviation, denoted by the whiskers, shows that the KPC sections had a large variation in collagen density. The CT26 collagen density was the lowest, but similar to the 4T1 densities. Another trend observed is that the periphery had a higher mean collagen density than the center for all the tumor models. Data for the plots can be found in Tables A.3 and A.4.

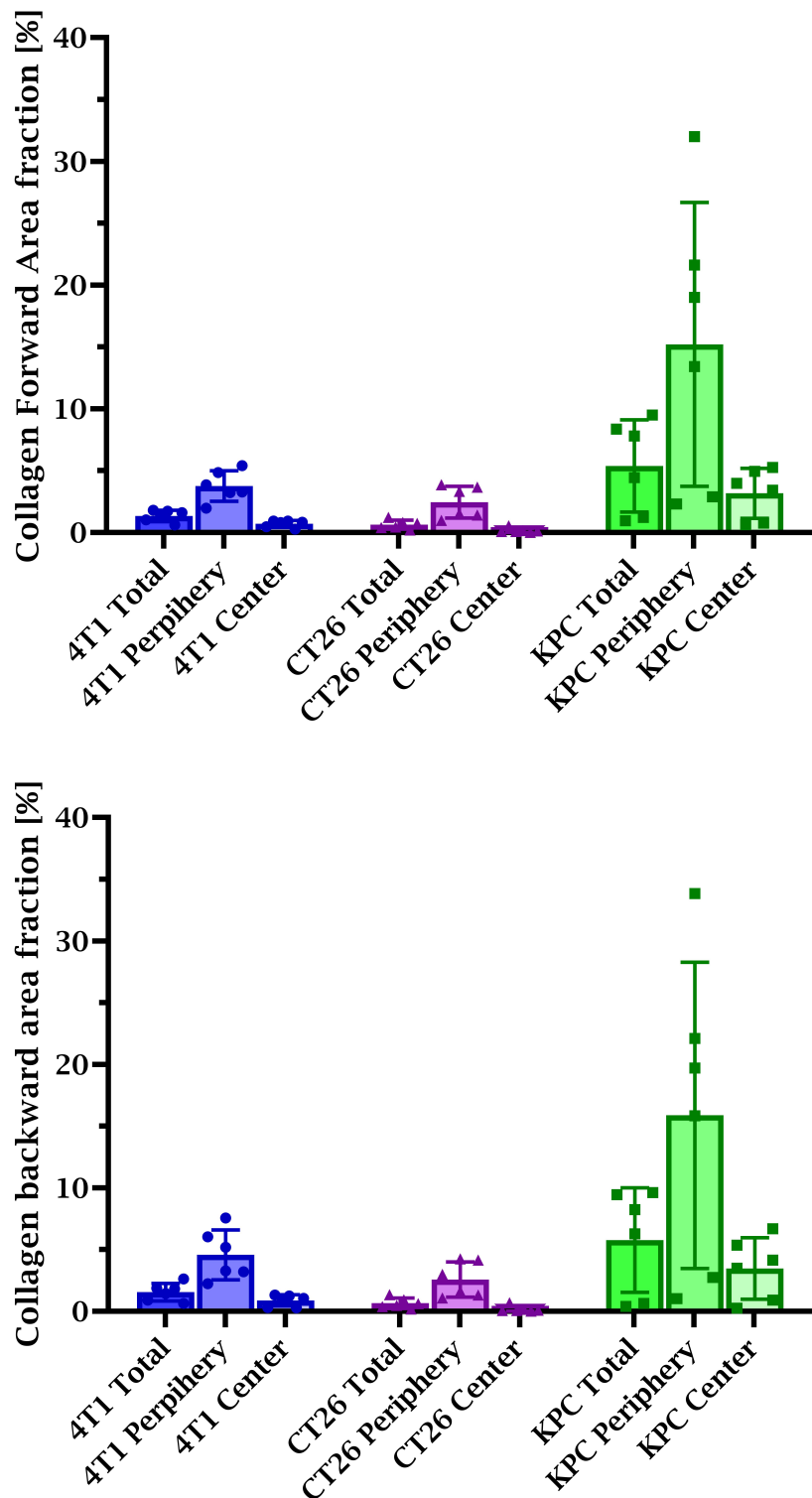


Figure 4.2: Area fraction of forward and backward collagen signal in 4T1, CT26, and KPC tumor sections. For each tumor model, the area fractions from the entire tumor section (total), periphery, and center are shown. Each point denotes individual tumor sections' area fractions, the bar denotes the mean between these points and the whiskers denote the standard deviation. These measurements come from 1 section per tumor of 6 different tumors from each of the tumor models, summing up to 18 tumors.

4.1.3 SHG F/B ratio

The SHG F/B ratio shown in Figure 4.3 describes the intensity between the forward and backward SHG. For all the tumor models, the ratio was similar with the forward SHG intensity being between 2-5 times higher than the backward SHG intensity. The only observable trend besides the results being similar between the tumor models, was that the standard deviation was smaller for the CT26 F/B ratios compared to the 4T1 and KPC models. Data for the plot can be found in Table A.5.

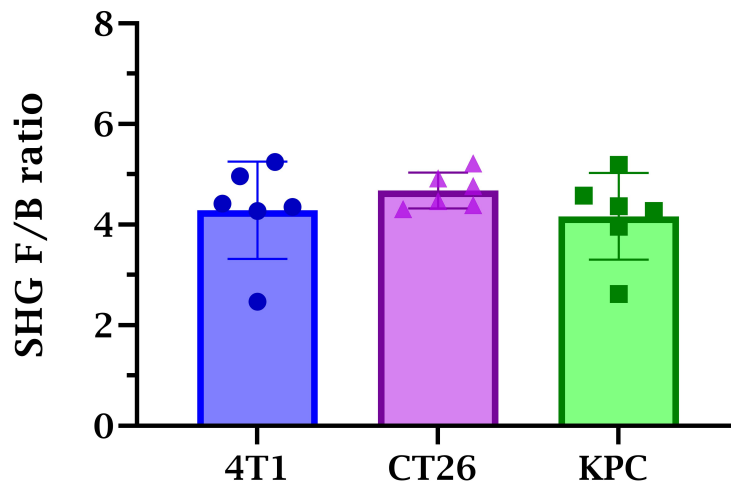


Figure 4.3: SHG F/B ratio in 4T1, CT26 and KPC tumor sections. Each point denotes individual tumor sections' FB ratios, the bar denotes the mean between these points and the whiskers denote the standard deviation. These measurements come from 1 section per tumor of 6 different tumors from each of the tumor models, summing up to 18 tumors.

4.1.4 Cell Density

Figure 4.4 shows the cell density of the tumor sections for the three tumor models. There were no significant differences between the total, center, or periphery within the tumor model groups and no significant differences were found between the tumor models either. However, there is a trend that the center of the tumor sections had a higher cellular density for all tumor models. Another observation is that the cellular density was larger for the CT26 and KPC tumor sections compared to the 4T1 tumor sections. Data for the plot can be found in Table A.6.

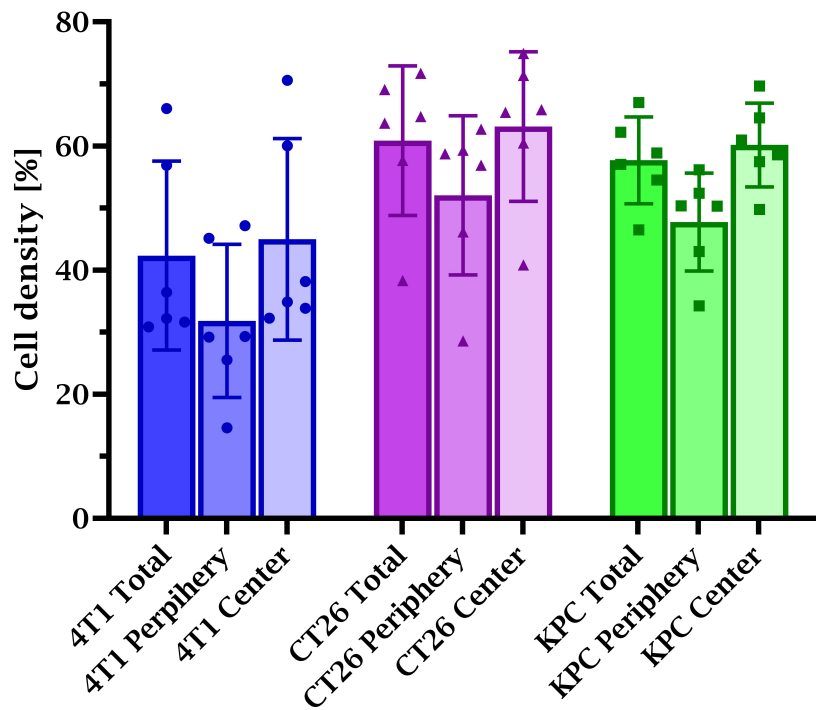


Figure 4.4: Percentage of cell density in 4T1, CT26 and KPC tumor sections. For each tumor model, the area fractions from the entire tumor section (total), periphery, and center are shown. Each point denotes individual tumor sections' cell densities, the bar denotes the mean between these points and the whiskers denote the standard deviation. These measurements come from 1 section per tumor of 6 different tumors from each of the tumor models, summing up to 18 tumors.

4.2 Tumor Weight and Area Fraction Correlation Analyses

The correlation matrix in Figure 4.5 describes the relationship between the tumor weight and the area fraction parameters, and how they correlate with each other. Between HA and tumor weight, and collagen and tumor weight, a significant negative correlation was found with $R = -0.75$ and $R = -0.60$, respectively. A significant positive correlation was found between collagen and hyaluronic acid with an $R = 0.73$. No significant correlations or trends were found between the cell density and the other parameters. Corresponding R and p values can be found in Table A.11.

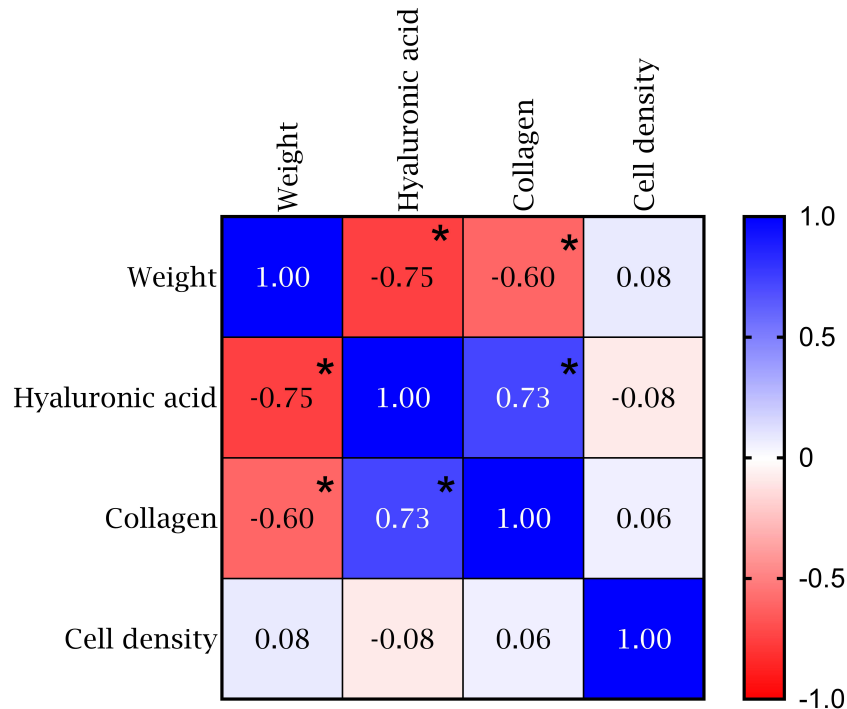


Figure 4.5: Correlation matrix between the tumor weights and all the area fractions of hyaluronic acid, collagen, and cell density. The matrix represents the correlation data as a heatmap where a strong positive correlation is blue and strong negative correlation is red, and no correlation is white. The Pearson correlation coefficient is written in each matrix cell. Asterisks describe where the correlation was statistically significant. The weight measurements included here came from 18 tumors, 6 from each tumor model. The area fraction measurements originated from 1 tumor section each from the same 18 tumors.

Figure 4.6 describes the plots of the individual correlation relationships shown in the correlation matrix. We see that the amount of HA and collagen decreases with the tumor weight in Subfigures 4.6a and 4.6b. In Figure 4.6d, increasing amounts of hyaluronic acid increase with the amount of collagen for these sections. R and p values for the plots can be found in Table A.11.

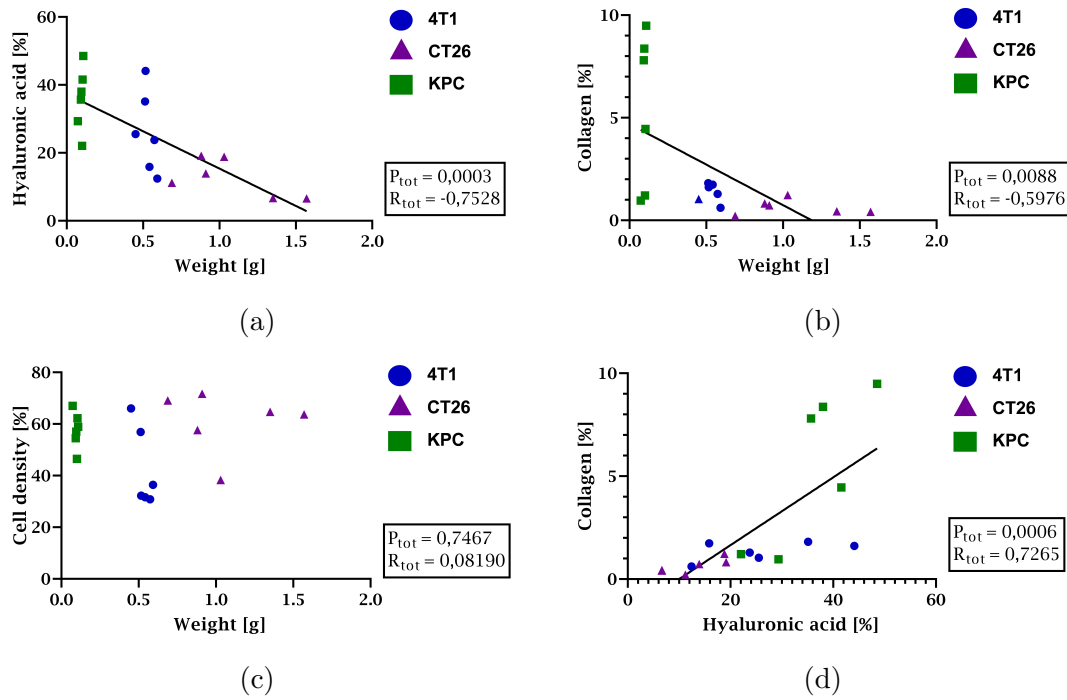


Figure 4.6: (a)-(d) shows correlation plots between area fractions described in Section 4.1 and the tumor weight. (a) shows the correlation between the tumor weight and the hyaluronic acid area fraction in the sections. (b) shows the correlation between the tumor weight and the collagen area fraction while (c) shows weight correlation with cell density. If the correlation is statistically significant for all the tumors this is denoted by a black line in the plot. 4T1 tumor sections are represented by blue circles, CT26 tumor sections by purple triangles, and KPC by green squares. The Pearson R coefficient is written as R_{tot} on the text box to the right of the plot together with its corresponding p-value, P_{tot} . The measurements come from 18 sections, 6 sections from each tumor model.

4.3 Effect of USMB Treatment on Uptake of Liposomes

4.3.1 Uptake Timelines for Tumor Models

Figure 4.7 shows the mean fluorescence from the tumors at the different time points during the USMB treatment. The points plotted here are at 0 h which is right after injection of NPs, 0.25 h which is directly after the USMB treatment, 1.25 h, 4.25 h, and 24 h. Both the treated and control groups' uptake seems to be similar before and after the USMB treatment. 1 h after the treatment the trends in the different tumor models are different. For the CT26 tumors in Subfigure 4.7b, the control and treated uptake curves meet and follow each other from the 1.25 h timepoint to the end. For the 4T1 tumors in Subfigure 4.7a, there is a higher mean fluorescence in the treated group at 1.25 h but after that, the mean fluorescence in the control group is higher until 24 h. The biggest difference between the treated and control group is found in the KPC tumors, which had a higher mean fluorescence from 1.25 h and on. It is also worth noting that the KPC had the highest mean fluorescence before treatment, with 4T1 having the second highest and the CT26 having the lowest mean fluorescence. Data for the plot can be found in Table A.7.

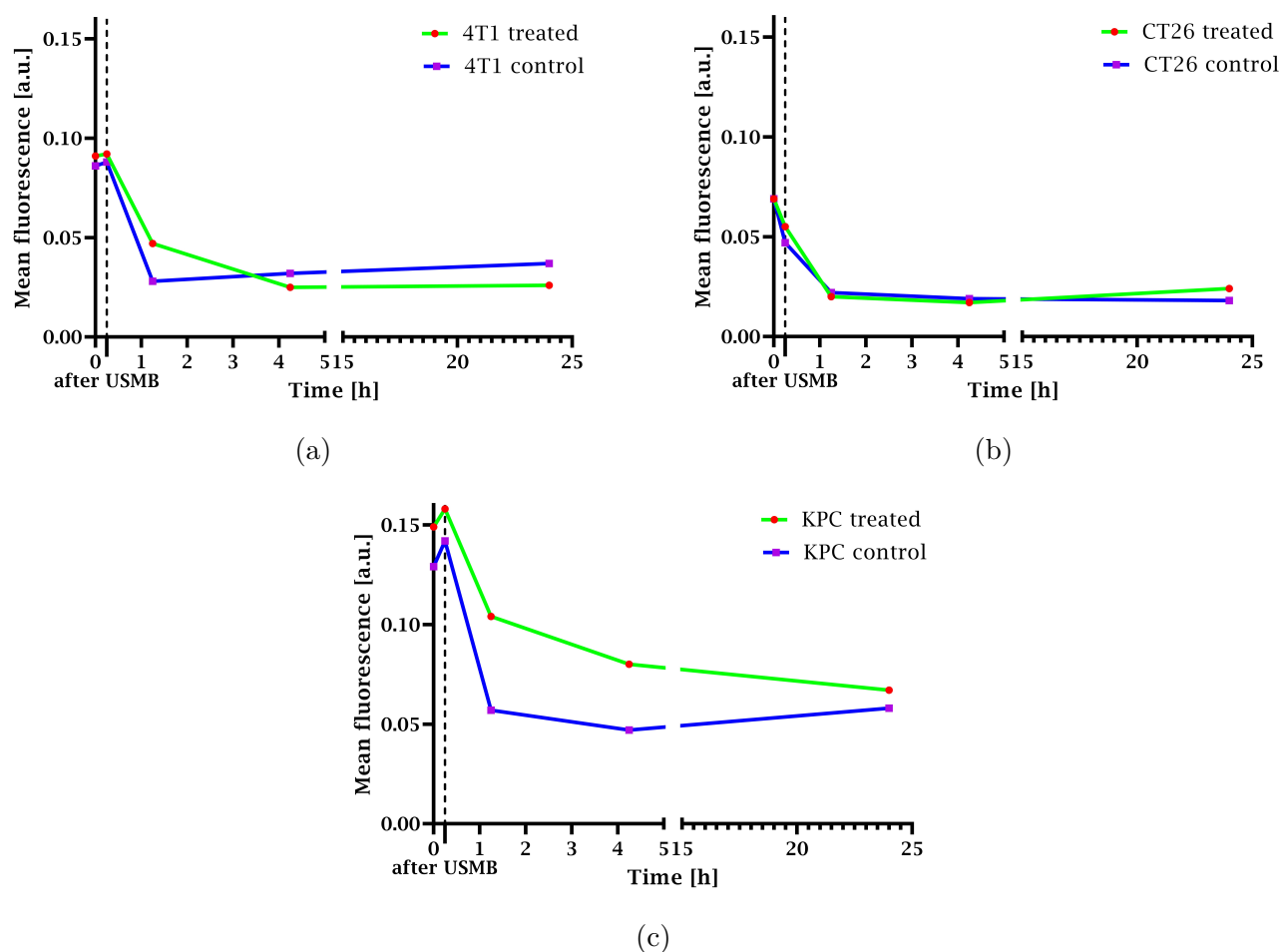


Figure 4.7: Timeline plots of the mean fluorescence of the liposomes in vivo during and around the USMB treatment. Mean fluorescence taken from Pearl whole animal scan images at 0h, 0.25 h, 1.25h, 4.25h, and 24 h. The 0.25 h time point is directly after USMB treatment. Each data point is the average of the mean fluorescence of three tumors in the treated and control group for a total of 18 tumors across the three plots. There is a break in the x-axis between 5h and 15h but no images were taken between these time points.

4.3.2 Uptake of Ex Vivo Tumors

In Figure 4.8, the mean fluorescence from the tumors 24 h after USMB treatment ex vivo, is presented. A statistically significant difference was found between the 4T1 control tumors and the CT26 control tumors, as well as between the treated KPC and treated CT26 tumors. The 4T1 and CT26 tumors shared that the control group had a higher mean fluorescence than their treated counterpart while the KPC tumor had the opposite. Another trend when comparing the tumor models was that the CT26 tumor had a generally lower mean fluorescence than the 4T1 and KPC tumors. Data for the plot can be found in Table A.8.

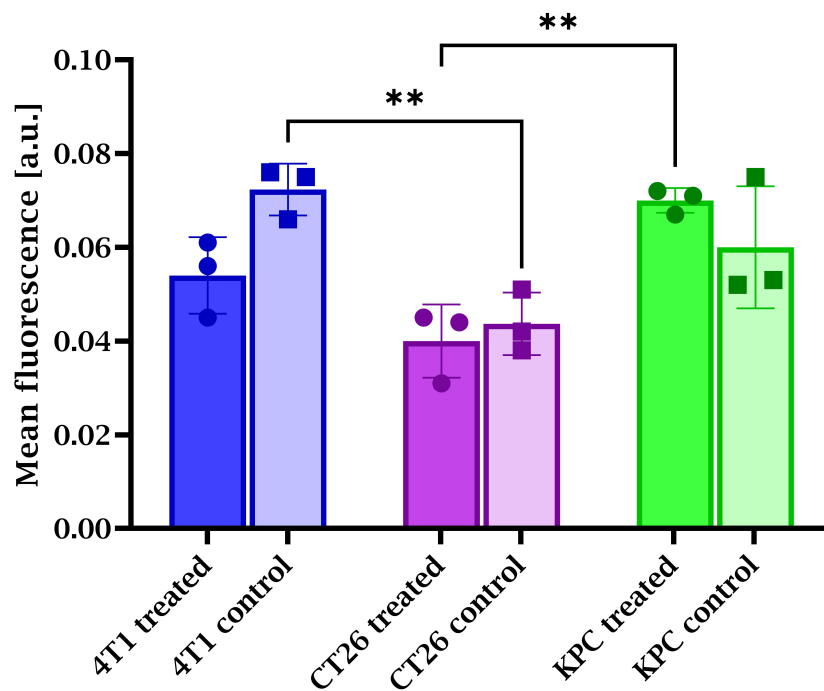


Figure 4.8: Mean fluorescence from tumors ex vivo 24 h after treatment for the 4T1, CT26, and KPC tumors. Each point denotes individual tumor sections' mean fluorescence, the bar denotes the mean between these points and the whiskers denote the standard deviation. These measurements come from 18 tumors with 3 control and 3 treated from each tumor model. Asterisks denote statistical significance between groups.

4.4 Correlation Between Tumor Uptake of Liposomes and Area Fractions of ECM Constituents and Cell Density

Figure 4.9, presents how the area fraction of HA, collagen, and cell density correlates with the mean fluorescence from the tumors, ex vivo. As can be seen in Subfigure 4.9a, there was a statistically significant positive correlation between the mean fluorescence and the amount of HA with $R = 0.7175$ and $p = 0.0008$ when pooling all the tumors together. This means that increasing amount of HA increases with the uptake for these samples. Looking at each of the tumor models individually, the 4T1 samples had a significant correlation coefficient of 0.9458 with a $p=0.0044$.

For the collagen as seen in SubFigure 4.9b, there was no statistical significance for all the tumors together. However, there was a statistically significant positive correlation for the CT26 samples with a correlation coefficient of 0.8732 and a corresponding p-value of 0.0231. For the cell density correlation in Sub-Figure 4.9c there were no significant correlations. R and p values for the plots can be found in Table A.12.

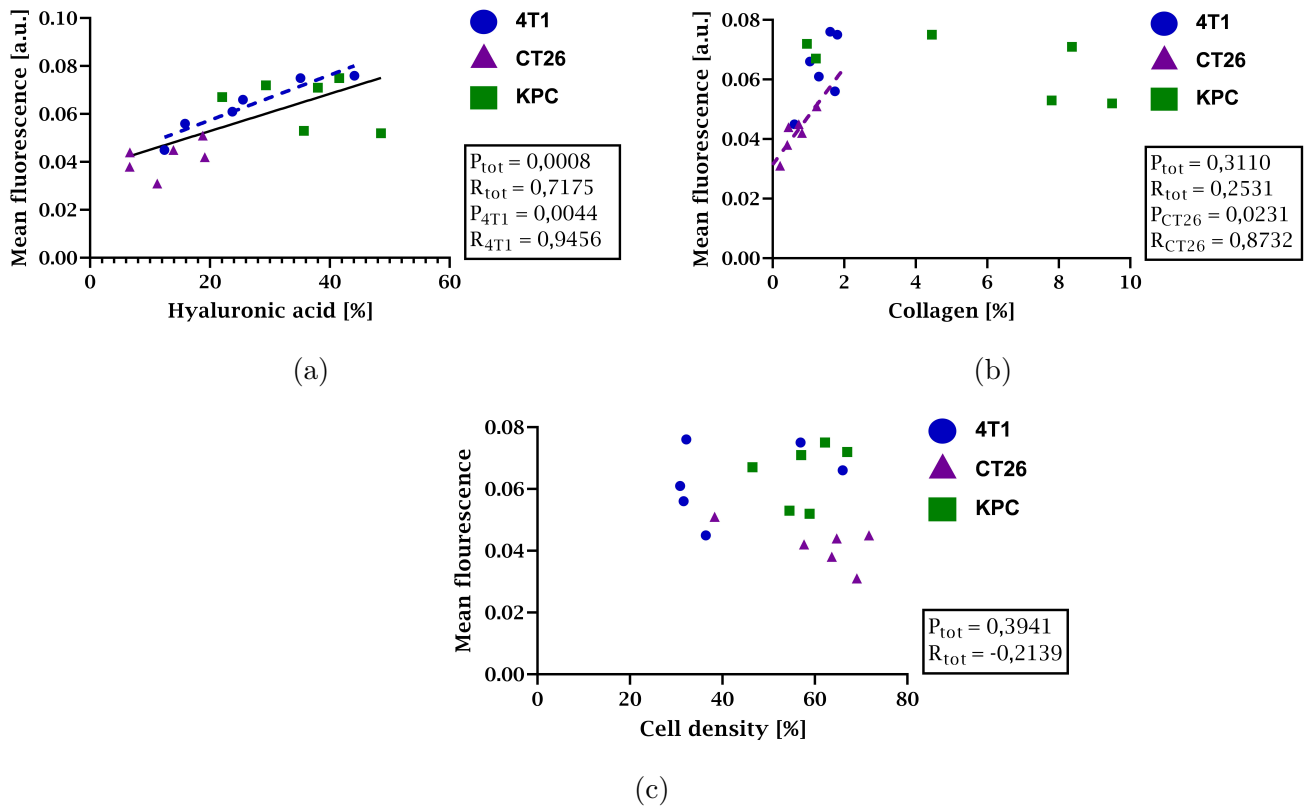


Figure 4.9: (a)-(c) Correlation plots between the ECM constituents, and cell density and uptake of fluorescent liposomes. (a) shows the correlation between the mean fluorescence of liposomes and the hyaluronic acid area fraction. (b) shows the correlation between the mean fluorescence and the collagen area fraction while (c) shows mean fluorescence against cell density. If the correlation is statistically significant for all the tumors this is denoted by a black line in the plot. If there is a significant correlation for one of the tumor model groups then this is denoted by a coloured dotted line. 4T1 tumor sections are represented by blue circles, CT26 tumor sections by purple triangles, and KPC by green squares. The Pearson R coefficient is written as R_{tot} on the text box to the right of the plot together with its corresponding p-value, P_{tot} . If tumor groups have a significant correlation their R- and P-values are also written in the same box. The measurements come from 18 tumors, with 1 section from each tumor.

4.5 Effect of USMB Treatment on Extravasation Distance of Liposomes

4.5.1 Mean Extravasation Distances of NP Clusters

Table 4.1 describe the number of extravascular NP clusters, or extravasation events, found in the images for the different tumor sections. It is evident that there are large differences in the number of extravasation events between tumor models and between individual sections in the same groups. Generally, there seem to be more extravasation events in the periphery compared to the center. Another observation is that fewer NP clusters were found in the images of the CT26 sections, compared to the 4T1 and KPC sections.

Table 4.1: Overview over number of extravascular NP clusters in the different tumor sections. Tumor Section columns describe what tumor model, whether it was in the treated (T) or control (C) group and the number is to separate between the sections. The number of extravasation events from Center and Periphery images is also given. These numbers are totaled in the total column.

Tumor Section	Total	Periphery	Center
4T1 T1	132	113	19
4T1 T2	144	88	56
4T1 T3	80	49	31
4T1 T sum	356	250	106
4T1 C1	223	165	58
4T1 C2	560	205	355
4T1 C3	109	94	15
4T1 C sum	892	464	428
CT26 T4	40	38	2
CT26 T5	95	47	48
CT26 T6	114	85	29
CT26 T sum	249	170	79
CT26 C4	26	16	10
CT26 C5	110	86	24
CT26 C6	58	45	13
CT26 C sum	194	147	47
KPC T7	92	62	30
KPC T8	228	183	45
KPC T9	155	126	29
KPC T sum	475	371	104
KPC C7	256	169	87
KPC C8	94	69	25
KPC C9	241	195	46
KPC C sum	591	433	158

Figure 4.10 shows the mean extravasation distance from the means of the individual 4T1 sections of the treated and control tumors. There was a significant difference between the treated periphery group and the treated center group. In addition, there was a significant difference between the treated and control group for the periphery. There seems to be a trend that the control sections have a lower mean extravasation distance than the treated group. Another trend is that the standard deviations in the treated groups were larger than for the control group. For the treated group, the periphery had the highest mean extravasation distance while for the control group, the center had the highest mean extravasation distance. The data for this plot can be found in Table A.9.

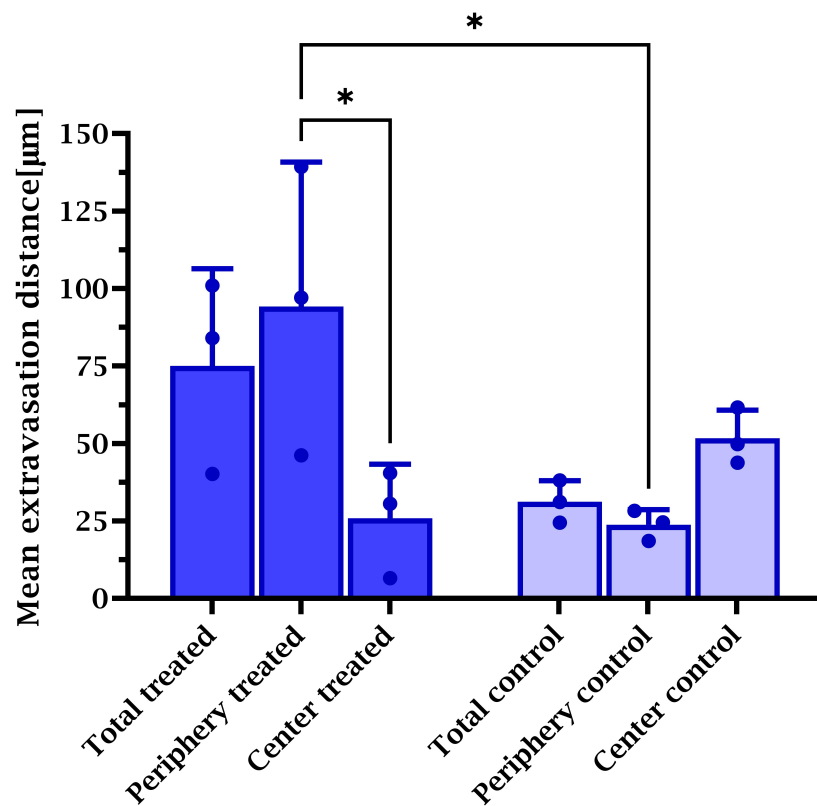


Figure 4.10: Mean extravasation distance for the 4T1 tumors in the treated and control group for the entire section, periphery, and center. Each point denotes individual tumor sections' mean, the bar denotes the mean between these means and the whiskers denote the standard deviation. These measurements come from 1 section per tumor of 6 different tumors from each of the tumor models, summing up to 18 tumors. The means are derived from the number of extravasation events in each section shown in Table 4.1. Asterisks denote statistical significance between groups.

The mean extravasation distance for the different CT26 groups can be found in Figure 4.11. No significant differences were found within or between the treated and control groups. A trend was that the mean extravasation distances were larger for the treatment group compared to the control group. There also seems to be a larger standard deviation for the treated group, than for the control group. For the treated group, the periphery had the highest mean extravasation distance while for the control group, the center had the highest mean extravasation distance. The data for this plot can be found in Table A.9.

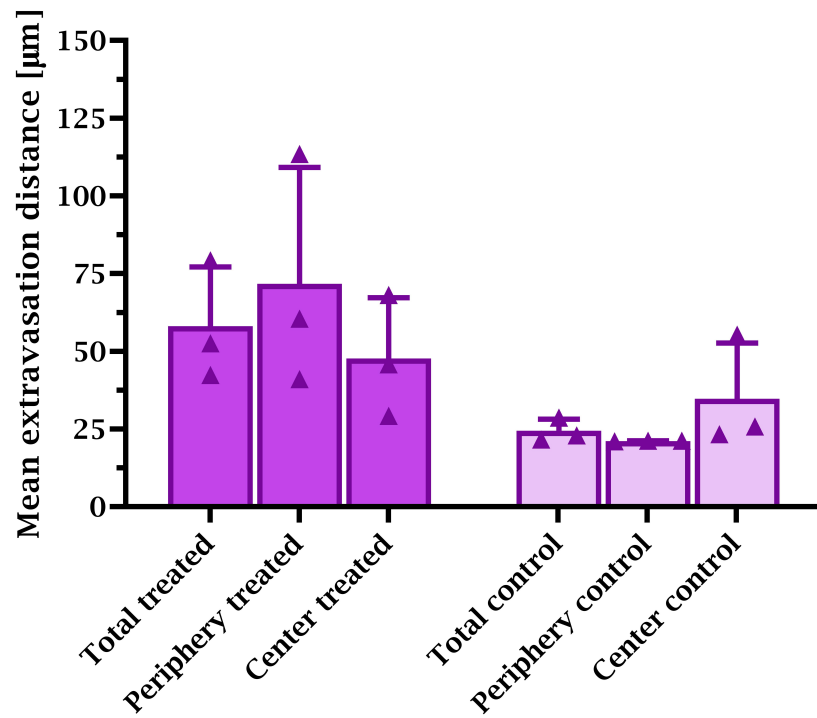


Figure 4.11: Mean extravasation distance for the CT26 tumors in the treated and control group for the entire section, periphery, and center. Each point denotes individual tumor sections' mean, the bar denotes the mean between these means and the whiskers denote the standard deviation. These measurements come from 1 section per tumor of 6 different tumors from each of the tumor models, summing up to 18 tumors. The means are derived from the number of extravasation events in each section shown in Table 4.1.

From Figure 4.12, the mean extravasation distance for the KPC treated and control groups are presented. No significant differences were found in the groups. An evident trend was that the treated and control group had very similar mean extravasation distances for all groups. The center had the largest standard deviation in both the treated and control groups. The data for this plot can be found in Table A.9.

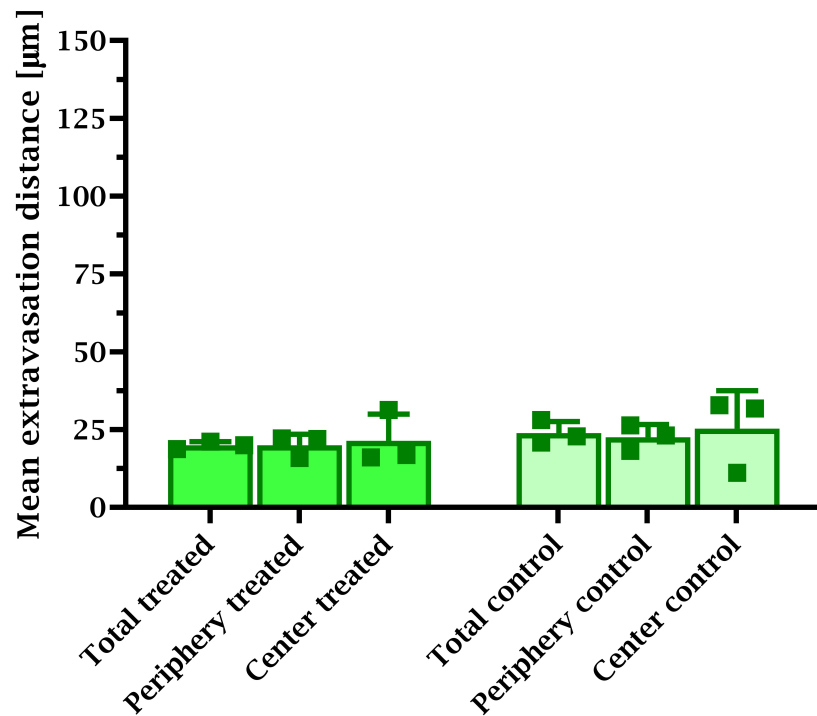


Figure 4.12: Mean extravasation distance for the KPC tumors in the treated and control group for the entire section, periphery, and center. Each point denotes individual tumor sections' mean, the bar denotes the mean between these means and the whiskers denote the standard deviation. These measurements come from 1 section per tumor of 6 different tumors from each of the tumor models, summing up to 18 tumors. The means are derived from the number of extravasation events in each section shown in Table 4.1.

In Figure 4.13, the mean extravasation distance from the total of the treated and control sections is compared between the three tumor models. There was a significant difference in the mean extravasation distance between the treated 4T1 and treated KPC tumors. The mean of the control groups seems to be similar between the three tumor models, while the treated are more different. Even though it is not significant, the mean extravasation distance between the treated CT26 and treated KPC tumors is noticeably different with CT26 having a higher mean extravasation distance. The data for this plot can be found in Table A.9.

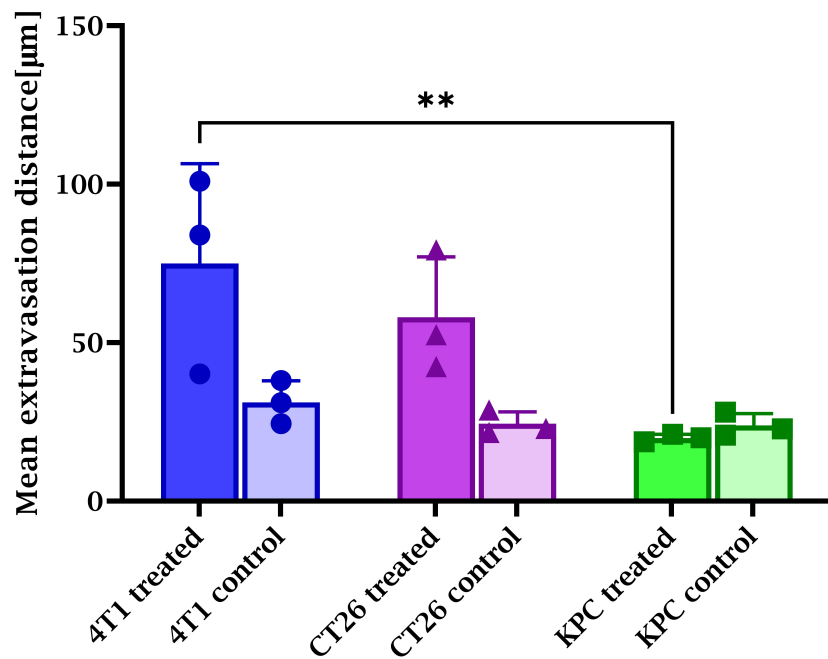


Figure 4.13: Mean extravasation distance for the treated and control group for the 4T1, CT26, and KPC sections. Each point denotes individual tumor sections' mean, the bar denotes the mean between these means and the whiskers denote the standard deviation. These measurements come from 1 section per tumor of 6 different tumors from each of the tumor models, summing up to 18 tumors. The means are derived from the number of extravasation events in each section shown in Table 4.1. Asterisks denote statistical significance between groups.

4.5.2 Fraction of NP Clusters as a Function of Extravasation Distances

In Figure 4.14, we see that up to 80 % of the NP clusters were between 0-10 μm from a BV. Small percentages of the NP clusters were from 20 μm and further from the BVs with the treated having a seemingly larger fraction between 100-200 μm . A trend is that the control NP clusters seem to have a more even distribution between the closest to the furthest distance from the BVs than the treated. The data for this plot can be found in Table A.10.

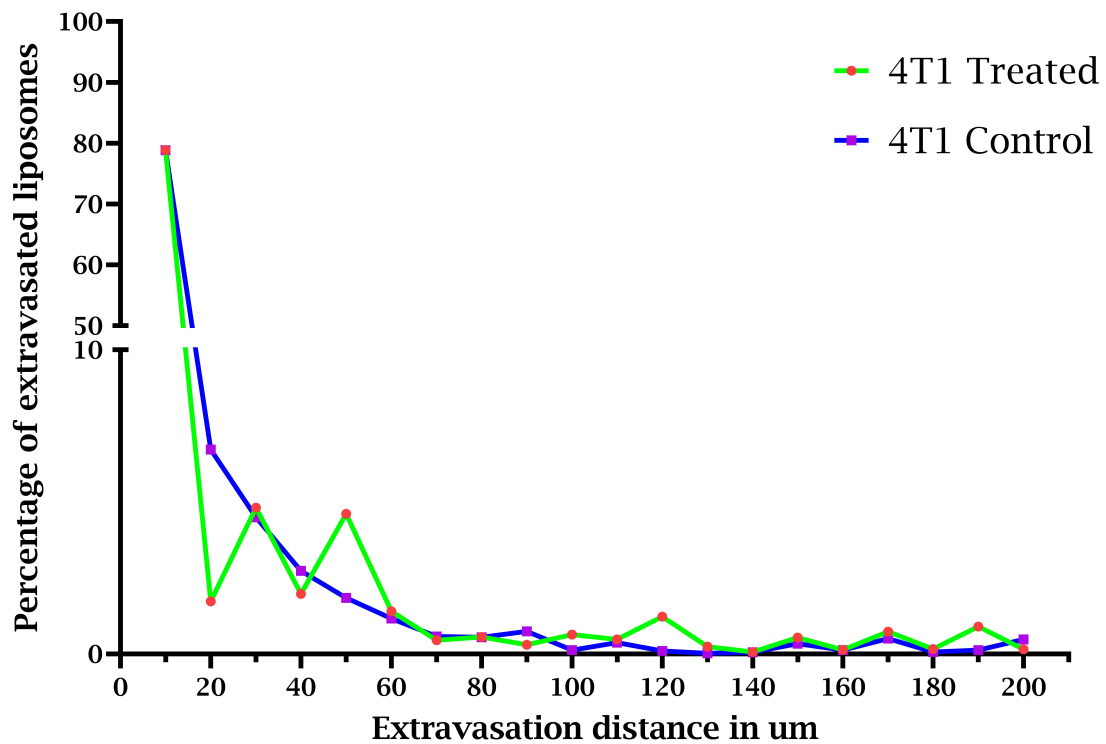


Figure 4.14: Plot of the percentage of extravasated NP clusters with 10 μm bins from 0-10 \rightarrow 190-200 μm for the 4T1 treated and control tumor sections. The y-axis is broken to highlight the features between 0-10 %. The treated data and control data are gathered from 3 sections each where the exact number of extravasation events are found in Table 4.1.

Figure 4.15 shows the fraction of NP clusters and their extravasation distances for the CT26 treated and control groups. Both of the groups had between 60-70 % of their NP clusters 0-10 μm away from the blood vessels. The control sections had a larger remaining fraction of the extravasation events at 30-40 μm away, while the treated sections had a larger fraction between 100-120 μm away. After 90 μm the fraction of the NP clusters for the control sections was close to zero up to 200 μm . Similarly for the treated sections at 150 μm and out. However, the peak at 120 μm seems a bit suspicious when compared to the slope of the curve diminishing up until that point. The data for this plot can be found in Table A.10.

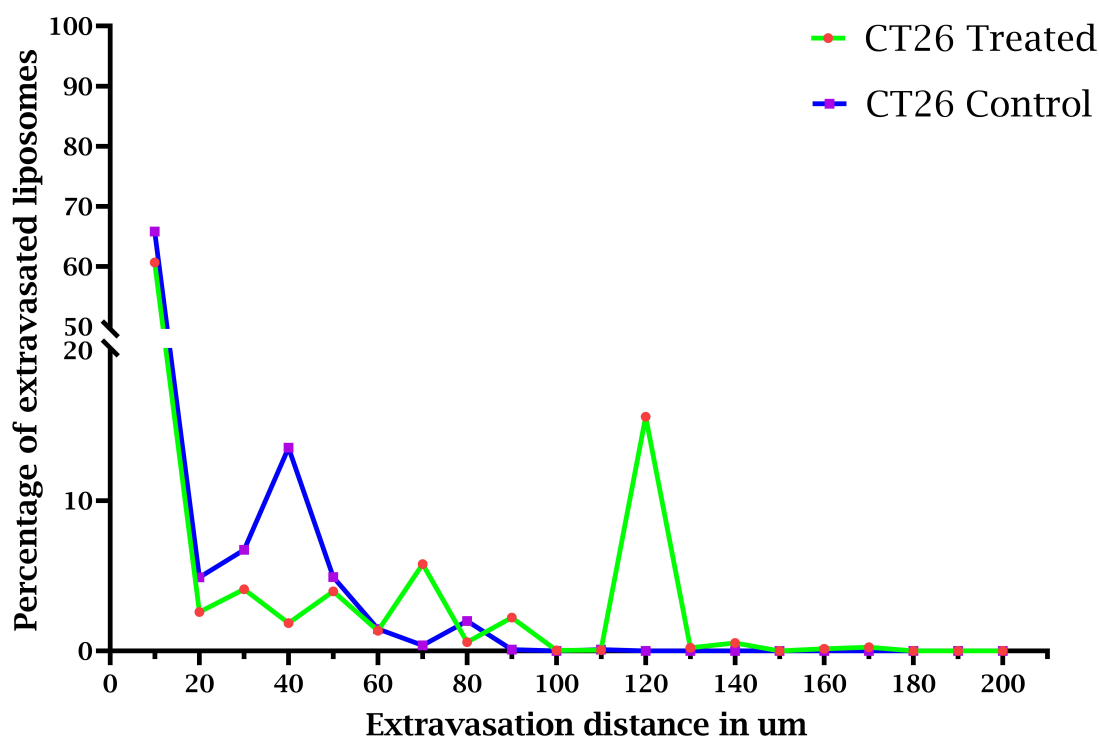


Figure 4.15: Plot of the percentage of extravasated NP clusters with 10 μm bins from 0-10 \rightarrow 190-200 μm for the CT26 treated and control tumor sections. The y-axis is broken to highlight the features between 0-20 %. The treated data and control data are gathered from 3 sections each where the exact number of extravasation events are found in Table 4.1.

About 80 % of the NP clusters were found 0-10 μm from the blood vessel for the KPC control and treated groups as can be seen in Figure 4.16. The curve diminishes a little quicker for the control group compared to the treated group. Above the 90 μm the percentage of the NP clusters, seem negligible and there are only small peaks up to 200 μm . The data for this plot can be found in Table A.10.

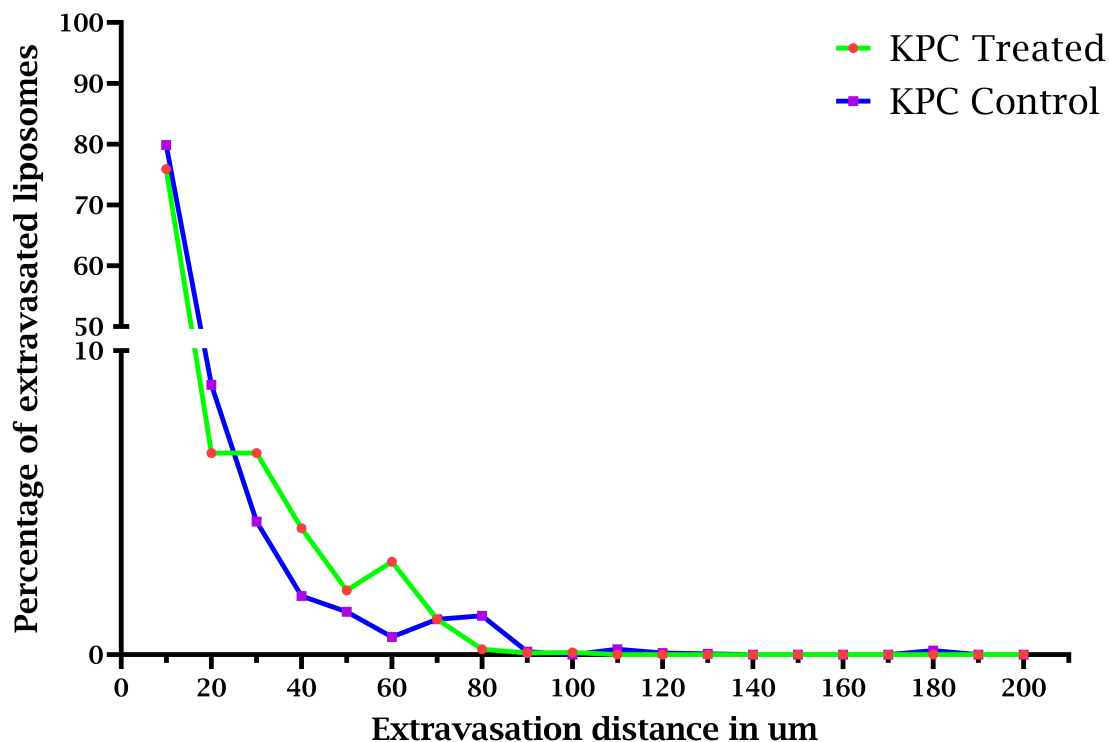


Figure 4.16: Plot of the percentage of extravasated NP clusters with 10 μm bins from 0-10 \rightarrow 190-200 μm for the KPC treated and control tumor sections. The y-axis is broken to highlight the features between 0-10 %. The treated data and control data are gathered from 3 sections each where the exact number of extravasation events are found in Table 4.1.

4.6 Correlation Between Extravasation Distances, and ECM Constituents and Cell Density

In Figure 4.17, the correlation between the mean extravasation distance and the area fraction of HA, collagen and cellular density is presented. For the HA and collagen correlation plots in Subfigures 4.17a and 4.17b, no significant correlations were found for all the tumor groups together or individually.

For the cell density and extravasation correlation analysis, there was a significant negative correlation as can be seen in Figure 4.17c. This means that the mean extravasation distance decreased with increasing cell density. The correlation coefficient was $R = -0.5666$ and $p = 0.0142$ for all tumors together. In addition, there was a significant negative correlation for the CT26 samples as well with a $R = -0.9298$ and $p = 0.0072$. R and p values for the plots can be found in Table A.12

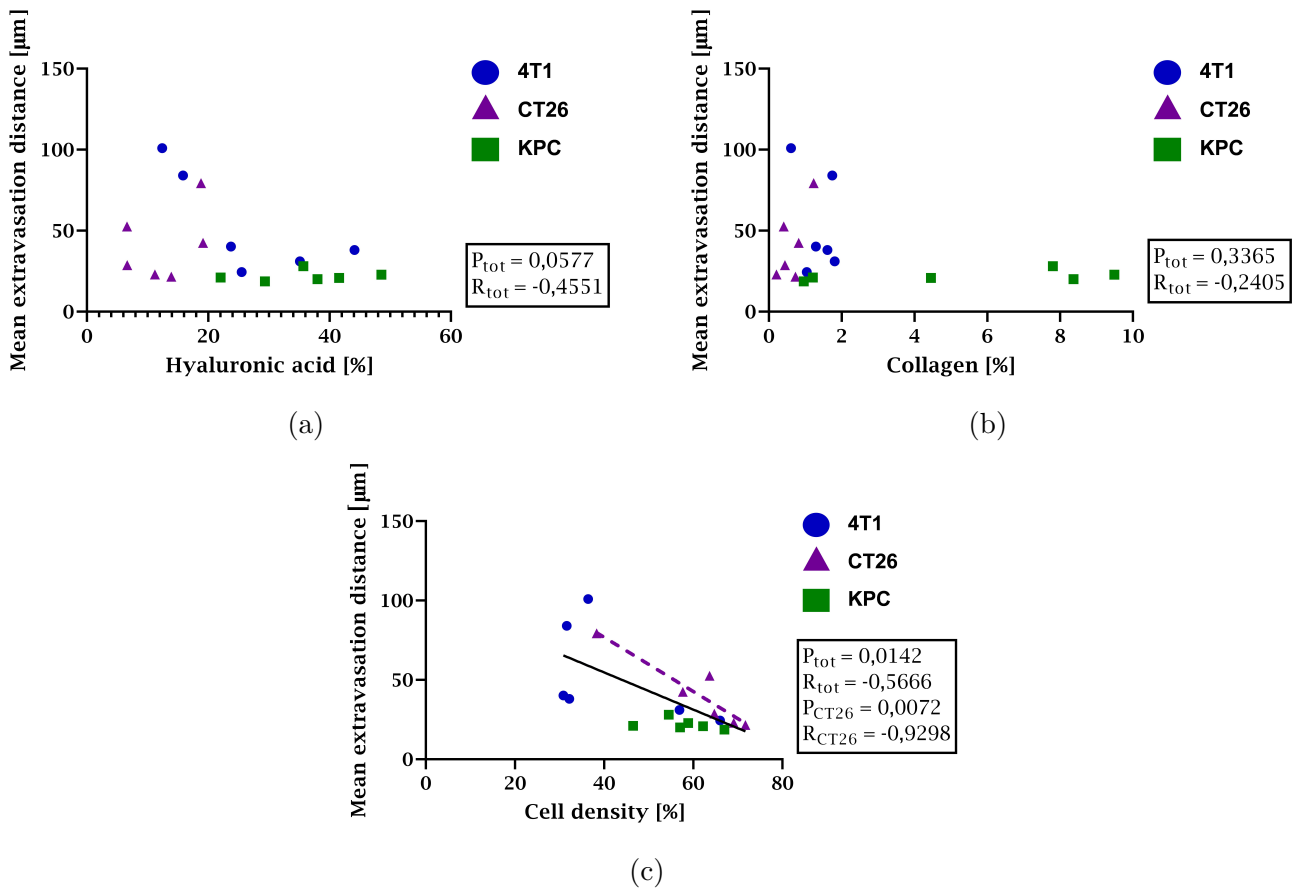


Figure 4.17: (a)-(c) Correlation plots between the area fractions of ECM constituents and cell density, and mean extravasation distances of the fluorescent liposomes. (a) shows the correlation between the mean extravasation distance and the hyaluronic acid area fraction in the sections. (b) shows the correlation between the mean extravasation distance and the collagen area fraction while (c) shows the mean extravasation distance against cell density. If the correlation is statistically significant for all the tumors this is denoted by a black line in the plot. If there is a significant correlation for one of the tumor model groups then these points are denoted by a colored dotted line. 4T1 tumor sections are represented by blue circles, CT26 tumor sections by purple triangles and KPC by green squares. The Spearman R coefficient is written as R_{tot} on the text box to the right of the plot together with its corresponding p-value, P_{tot} . If tumor groups have a significant correlation their R- and P-values are also written in the same box. The measurements come from 18 sections, 6 sections from each tumor model.

Chapter 5

Discussion

The extracellular matrix is a major obstacle for the successful delivery of drugs and nanoparticles to tumors. In the present work, HA, collagen, and cell density were characterized in three different tumor models. These models were chosen because they could represent a variety of tumors based on their mechanical properties. Both the KPC and 4T1 tumors are stiff, while the CT26 tumors are comparably very soft. Since ECM greatly contributes to the mechanical properties of tissues this is an indication that the ECMs in the three tumor models could be different. To the author's knowledge, this thesis represents the first comparative study of ECM components and their effect on drug delivery between these three tumor models. Thus, this study could illuminate the most important barriers in ECM for drug delivery in these tumor models.

One important consideration during this entire discussion is the sample size and how it affects statistical significance. 18 tumors were studied and most of the data comes from one 8 μm section of each of these tumors. Even though a statistically significant difference is reported between these sections, one must be careful to draw the conclusion that this pertains to the tumor models as a whole. There are always variations between tumor sections from different tumors and even variations between sections from the same tumor as well due to tumor heterogeneity[60]. Therefore, the sections studied may not always accurately represent the tumors as a whole even though there might be statistically significant results.

5.1 Characterization of Tumor Models

In order to evaluate how the area fractions of ECM constituents and cell density affect the tumor uptake and extravasation of liposomes, it is important to first compare these values to similar works and published literature. When comparing our results with the literature, an important concept to keep in mind is that mutations in cancer cells are a dynamic process and the expression of these mutations can influence the individual tumor and TME immensely, and in different ways [60, 61]. So it is expected that results could deviate from similar studies, as well as reproduce results from not as similar studies. Tumor heterogeneity makes it difficult to reproduce biology in works such as this, and will always be a factor that contributes to a large variety.

Different experimental approaches will also affect the results and comparability

between studies. Which mouse strain is used, the number of cells implanted, and where they are implanted can all influence the tumor characteristics greatly. Especially whether the tumors are subcutaneously (sc) or orthotopically (ot) grown can greatly influence the tumor microenvironment and growth kinetics [62, 63].

5.1.1 Hyaluronic Acid Area Fraction

A significant difference in the HA area fraction was found between the KPC and CT26 tumors as shown in Figure 4.1. There was a trend with the periphery having a larger amount of HA than the center for the 4T1 and CT26 sections, and this is in accordance with the reported distribution of ECM components in the literature as well [34].

In her master's thesis, Årseth measured the HA area fraction the same way as this thesis for sc 4T1 tumor sections[45]. She found a total mean area fraction of 25.3 %. This is in accordance with this work which found a total area fraction of 26.1 % for the 4T1 sections. However, no trend with the periphery having the largest area fraction was found in her work. This could be due to the way the area fractions were measured. Unlike this work, which imaged entire tumor sections, Årseth took four images in the center and periphery of the section and calculated the mean fluorescence from these. One could speculate that an overview of the entire periphery and center would yield a better representation of the HA distribution in the center and periphery.

Many examples of characterization of HA in different tumors can be found in published literature. However, it is difficult to find literature for the 4T1, KPC, and CT26 tumor models that use exactly the same techniques as this work. Incio et al. studied the effect of the drug metformin on the area fraction of HA in murine ot PDACs [64]. They found an area fraction of about 30 % in frozen 10 μm sections that were stained using indirect immunofluorescence. This is comparable to the mean HA area fraction of 35.87 % for the KPC model in this work.

Reeves et al. found an HA area fraction of about 38 % in ot 4T1 tumors [65]. Sections were 5 μm thick, and stained with a biotinylated recombinant fluorescent HABP. This is higher compared to this work's HA area fraction for 4T1 tumor sections of 26.13 %. These differences could be due to different sectioning protocols, or the tumors being grown orthotopically in stead of subcutaneously.

In Voutouri and Stylianopolous's study of 4T1 ot tumors, a 70 % HA area fraction was found in their 40 μm thick indirectly immunostained sections [66]. Conversely, in a more recent study, Hadjigeorgiou and Stylianopoulus found mean HA area fractions of 5 %, 9%, and 3 % for sc murine MCA205 fibrosarcoma, ot 4T1 breast cancer, and sc murine PAN02 pancreatic carcinoma, respectively [67]. In this study, however, the sections were 7 μm thick and were indirectly stained using biotinylated HABP and fluorophore-conjugated streptavidin rather than two conjugated antibodies. One apparent difference in the protocols here is the thickness of the sections, so that could explain the differences for the 4T1 tumors. It is interesting that two studies outlined by the same person could produce two very different results but as the main focus of both articles was tumor stiffness and growth-induced mechanical stress, Stylianopol-

ous did not comment on this discrepancy. Nevertheless, it substantiates that tumor heterogeneity can make it difficult to reproduce results.

No literature on the HA area fraction of CT26 tumors was found. Given the variance of HA area fraction between the different tumor models presented our results seem plausible. Because of the differences found in the literature, a golden standard for HA characterization would be beneficial to better compare different tumor models.

5.1.2 Collagen Area Fraction

No significant differences in the collagen area fraction were found for the three tumor models as presented in Figure 4.2. A trend, however, was that the KPC sections had higher collagen fractions than the 4T1 and CT26 sections, but the KPC sections also had the largest standard deviation. Pancreatic cancers are often characterized by desmoplasia which describes an excessive amount of collagen in the tumor stroma [68]. So this could explain why there is a difference, but more sections should have been imaged to illuminate whether there actually was a significant difference in collagen amount between the tumor models. Another trend was that the periphery of the tumors had the highest amount of collagen for all tumor models which is in accordance with literature [34].

Fibrillar collagen was imaged by the SHG signal which is a non-labeling technique whereas many examples from the literature use immunostaining or organic dyes to stain collagen. The main difference between these methods is that the SHG signal originates from the intrinsic properties of fibrillar collagen I and II, while other staining techniques use exogenous labels to stain all types of collagen [58]. Thus, one could expect the SHG signal to produce lower collagen area fractions than other collagen staining techniques but also expect fewer uncertainties due to no dye being prone to bleaching or unspecific binding.

In her master's thesis, Årseth also studied the collagen area fraction in sc 4T1 tumors by imaging SHG. Årseth found average collagen area fractions of around 4 % and 3 % for the periphery and center, respectively [45]. This is a little higher than the area fractions found for 4T1 in this work, but comparable. Årseth used 4 images in both center and periphery to determine a mean collagen area fraction. On the other hand, Bang did tile scans of sc 4T1 sections to determine the collagen area fraction in her thesis the same year [69]. She found average periphery and center collagen fractions of around 10 % and 4 %, respectively. The average periphery and center collagen fractions for the 4T1 sections in this work were around 4 % and 1 %, respectively. The standard deviations were similar across all works with around 50 % of the mean. Our results are more in accordance with Årseth's than Bang's. One would expect that similar techniques would yield a more reproducible result, but this was not the case. These results show that the amount of collagen might be heterogenous within a tumor and more than one tumor section should be analyzed. This is substantiated by the author's project thesis which found a large intraheterogeneity for the collagen measurements in the 4T1, CT26, and KPC tumor models [25].

Sulheim et al. also studied the collagen area fraction by using the SHG signal, for

five different human tumor models implanted subcutaneously in mice [70]. They examined PC3 and PC3/2G7 pancreatic carcinoma, MDA-MB-231 triple-negative breast cancer, A431 epidermoid carcinoma, and OHS osteosarcoma. The mean collagen area fractions ranged from about 0 % for the A431 periphery to 5 % for the PC3 center. No apparent trends between the center and periphery distributions seemed to be present. These results are in the same range as the aforementioned area fractions of collagen when using SHG, and also in the same range as this work substantiating our results.

Similar collagen area fractions were found in the orthotopic MIAPaCA-3 and BxPcC-3 human pancreatic tumors characterized by Stylianou et al. [71]. They took biopsies of the tumors at three different time points and stained 7 μm thick sections with picrosirius red, before imaging with polarization microscopy. There was an increased amount of collagen at the second and third time points, indicating that growth kinetics are highly important for the amount of collagen.

Vouturi and Stylianopolous, and Hadjigeorgiou and Stylianopoulus also studied collagen area fractions in their studies outlined in the previous subsection [66, 67]. A greater mean collagen area fraction was found for the 40 μm thick ot 4T1 sections in the former study compared to the 7 μm thick ot 4T1 sections in the latter study. For the 40 μm sections, up to 3 times higher area fractions were found for both collagen and HA when compared to the 7 μm sections. This illuminates how important the section thickness could be for characterizing ECM constituents. Indirect immunofluorescence was used to stain the collagen in both of these studies. Compared to this work's 4T1 sections, the latter study found 20 times higher mean collagen area fractions for the 4T1 sections even though the section thickness was approximately the same. This could be due to the SHG only originating from the fibrillar collagen I and II in our study, while the antibodies stained all types of collagen in the latter study. Tumor heterogeneity could also be a large contributor to this discrepancy.

In the author's project thesis, the amount of collagen was biochemically characterized in the same tumor models as this work [25]. Significantly lower amounts of collagen were found for the CT26 tumor samples compared to the other two models. The 4T1 and KPC had similar means, but the highest collagen measurements were from the KPC samples. This is in accordance with the trends found here where the collagen fraction was highest in the KPC sections, and lowest in the CT26 sections. However, the 4T1 sections were more similar to the CT26 sections than the KPC sections in this work. Biochemical characterization could be a better way to characterize the ECM constituents because this is a more direct method that does not require any imaging or image processing. One sample is also usually a larger fraction of the tumor than an 8 μm thick section, which makes them more representative of the whole tumor. However, biochemical characterization only gives absolute amounts in a sample and does not illuminate the distribution locally of the ECM components, which could be just as important when looking at barriers to drug delivery.

5.1.3 Collagen Organization Measured by the SHG F/B Ratio

For all the tumor sections, the F/B ratio of the SHG signal was of a similar magnitude with similar mean values between the three tumor models as shown in Figure 4.3. This indicates that the structure of the collagen is similar in the three tumor models. An F/B ratio > 1 means that the sections have more ordered collagen structures than random collagen structures [58]. In this work, the mean F/B ratio was between 4-5 which means that there were 4 to 5 times more ordered collagen structures than random structures in the sections for all the tumor models.

Årseth and Bang also calculated the F/B ratio in their master theses for 4T1 sections [45, 69]. Årseth found mean F/B ratios between 4 and 5 for her sections while Bang reported mean F/B ratios between 1.5-2. This work is more in concurrence with Årseth's results. The differences show that collagen organization in the same tumor model can be as heterogenous as the amount of collagen.

From the literature, Han et al. reported an F/B ratio of 44.5 ± 15 for a $100 \mu\text{m}$ thick 4T1 tumor section while Burke et al. reported an F/B ratio of around 4-6 for $5 \mu\text{m}$ thick human breast cancer sections [72, 73]. Again, the thickness of the section seems to be an important factor since there is such a big discrepancy between Han's and Burke's results. Burke had sections with a similar thickness to this work, and the resulting F/B ratios were much more similar to this work as well. No literature on F/B ratios in the KPC and CT26 tumor models was found, but since they had similar ratios to the 4T1 sections, the results seem comparable. For future studies, it would be interesting to look at how this ratio changes with the thickness of the sections to illuminate whether these F/B ratios can reliably describe the collagen organization in tumor sections.

5.1.4 Cell Density

No significant differences in cell density were found between the three tumor models, and the only shared trend was that the center had a larger cell density than the periphery. Another observation was that the 4T1 sections had a lower mean cell density than the KPC and CT26 sections, but also had a larger standard deviation.

In addition to characterizing the collagen area fraction in the five tumor human tumor models, Sulheim et al. also examined the cell density [70]. For the PC3 and PC3/2G7 pancreatic carcinomas a mean cell density of about 19 % and 25 % were found, respectively. While for the MDA-MB-231 triple-negative breast cancer a mean density of about 22 %, A431 epidermoid carcinoma of about 13 %, and 23 % for the OHS osteosarcoma. Higher mean cell densities were found in this work with means ranging from 40-60 % for the three tumor models. This could be because the tumor models in Sulheims work were human xenografts while the tumor models in this work were murine tumor models. Sulheim also reported that most of the tumors in his work had necrotic centers which also could have contributed to the lower cell density compared to this work. There were areas observed in our tumor sections that could

be necrosis as well, but a pathologist's opinion would be needed to conclude anything.

5.1.5 Tumor Weight and ECM Constituents

As seen in the correlation matrix in Figure 4.5, both HA and collagen had a significant negative correlation with weight. Since the tumor weight seems to have a large impact on the amount of ECM constituents, it is important to look at the area fraction results with this in mind. As seen in Table A.1, the KPC tumors were the smallest with the 4T1 and CT26 tumors being around 5 and 10 times heavier, respectively. The KPC tumors had the sections with the most collagen and HA, and it would have been interesting to see whether the total area fraction would have decreased if the tumors were allowed to grow larger. If not, then a large amount of ECM constituents would be a specific characteristic of the KPC models.

In the author's project thesis, the results also indicated that the collagen amount negatively correlated with the tumor weight but it was not significant [25]. Davies et al. also studied the correlation between biochemically characterized collagen and HA with tumor weight in orthotopic and subcutaneous OHS tumors [63]. They found that the collagen content negatively correlated with tumor weight for the orthotopic tumors and positively for the subcutaneous tumors. While there was a significant negative correlation between HA and weight for the orthotopic tumors and no significant correlation for the subcutaneous tumors. This shows that a difference in growth site could be very impactful on the characteristics of a tumor as well as the weight. It is difficult to conclude what impact the large differences in tumor weight may have had on these experiments. For future experiments, tumors with more similar weights would probably aid in illuminating any tumor model-specific differences.

5.1.6 Quality of Tumor Sectioning

CMIC reported difficulties with the sectioning of the tumors, especially with the soft CT26 tumors. This caused the tumor sections to have an uneven thickness, edges that were folded, and a lot of holes. For the NP and BV imaging, this was not a big problem since one could omit areas that seemed to have these faults. However, it posed a challenge for the tile scan images. Since some of the sections were very big, a lot of focus points were needed to create a good focus map for the tile scans. Despite a lot of focus points, the focus map generated in the LASX software sometimes performed sub-optimally and this could have affected the results.

To preserve tumor sections, the two most used methods are freezing the tumor before sectioning in a cryostat or embedding the sections in paraffin. Fixating the tumor sections in paraffin could possibly have improved the uneven sectioning. However, the fixation process with paraffin-embedded sections contains several washing steps and this could wash out the NPs. Because of this, frozen sections were the only viable option in this study. In addition, the consensus seems to be that frozen sections are more optimal for immunostaining while paraffin is more optimal to preserve the mor-

phology of the section [74]. Thus, frozen sections would have been preferred for this work either way.

5.2 Effect of ECM Constituent on Liposome Uptake and Extravasation Distance

5.2.1 Interpreting the Tumor Uptake and Extravasation Distance of Liposomes

Before discussing the effect that the ECM constituents and cell density could have had on the uptake and extravasation of the liposomes, it is important to discuss what the uptake and extravasation data represent. The uptake data are presented as a mean fluorescence for an ROI drawn around the tumor in vivo and ex vivo as seen in Figures 4.7 and 4.8, respectively. The fluorescent signal can originate from the liposomes in the blood vessels or in the tumor interstitium. Since the liposomes leave the circulation after a while, the signal from the blood vessels will decrease with time. The extravasation data originates from 8-12 CLSM images from one tumor section per tumor and shows the distribution of NP clusters in the periphery and center of the tumors. So, where the uptake tells us something about the total accumulation of liposomes in the tumor, the extravasation data tells us more about the micro-distribution of the liposomes within the tumor interstitium. It is important to reiterate that one section from each tumor was used, and the micro-distribution of liposomes in the entire tumor might not be representative from one section.

When interpreting the ex vivo uptake of liposomes shown in Figure 4.8, it is important to consider how the uptake changed over time from Figure 4.7. For the control tumors, the mean fluorescence is higher in the KPC tumors compared to the 4T1 and CT26 tumors. One reason for this could be that the fluorescence emission was more attenuated in the larger tumors. Especially the CT26 tumors that had the lowest mean fluorescence were up to 10 times bigger than the KPC tumors and this could have contributed to the observed differences. Another reason could be that the larger tumors had more necrosis and thus, less functional blood vessels. To this point, a negative correlation between the tumor weight and functional blood vessels was found in Kastellet's master thesis for the 4T1 and CT26 tumors this spring [75]. Also, the difference in uptake of the liposomes between the control tumors in the three different models could also be due to the KPC tumors having a stronger EPR effect. Some studies report that the EPR effect can be highly variable and heterogenous in different tumors [76]. This would explain why the uptake reduction was not as large for the KPC tumors at 1 h and 4 h compared to the other two tumor models. Ultimately, it could be a combination of all these factors or other factors.

When looking at the extravasation data in Table 4.1, one thing that is very apparent is the different number of NP clusters identified for the different sections. To minimize this uncertainty and for better comparison between the three tumor models, all the

extravasation events and their corresponding extravasation distances were averaged for each section. In addition, since the FITC-lectin was injected 24h after injection of liposomes it is possible that some of the blood vessels that were open during the time of NP injection closed, and were not stained. Meaning, that there could be areas in the sections with a lot of NP clusters that were not imaged because they were not in the proximity of visible BVs. With this in mind, evaluating the uptake of liposomes based on the number of NP clusters alone would not be beneficial. However, if we assume that the number of NP clusters found in a section is representative for the number of NPs taken up into the entire tumor interstitium. Then, the uptake of liposomes from the tumors ex vivo would correspond to the number of extravasation events i.e. the largest amount of NP clusters were found in the KPC tumors and they also had the highest ex vivo uptake of liposomes. While the lowest amount of NP clusters was found in the CT26 tumors and they also had the lowest ex vivo uptake of liposomes. This substantiates the trends observed in the uptake and extravasation of liposomes.

5.2.2 Hyaluronic Acid as a Barrier for Nanoparticle Delivery

A significant positive correlation was found between the ex vivo uptake of the liposomes and the area fraction of HA. In addition to a significant positive correlation for all the tumors pooled together, the 4T1 tumors also had a significant positive correlation alone. This means that the uptake of the liposomes increased with increased values of HA. This is interesting since high HA is often associated with decreased drug delivery [77, 65, 4].

While the liposome uptake positively correlated with the HA fractions, a negative but insignificant correlation was found between the HA fraction and the liposome's mean extravasation distances. The negative correlation was almost significant when all the tumor samples were pooled together with a $p = 0.0577$. This is in agreement with the established literature. Since the NPs do not penetrate further into the interstitium this indicates that HA is a barrier in these tumor models.

In 2005 Eikenes et al. investigated the uptake of doxorubicin encapsulated in liposomes in sc and orthotopic OHS tumors with intratumor injections of hyaluronidase [78]. Hyaluronidase is an enzyme that breaks down HA [79]. They found that injection of hyaluronidase greatly improved the doxorubicin distribution in the center of the tumor compared to the non-treated tumors. A similar study was done by Jacobetz et al. in 2012 where they studied how PEGylated human recombinant PH20 hyaluronidase could improve the drug delivery of chemotherapeutics in KPC tumor models [77]. They also found that enzymatic depletion of HA increased the delivery of the chemotherapeutics and lead to the re-expansion of the blood vessels.

With the use of hyaluronidase increasing the delivery of drugs in tumors in the literature, it is no doubt that HA is a barrier in drug delivery to solid tumors. The mechanism by which it is a barrier is more unclear. As mentioned in Section 2.4.1, an increased amount of HA increases the IFP which decreases convective transport

mechanisms into the tumor. In this work, it was found that increased amounts of HA increased the uptake of liposomes while decreasing the extravasation distance of the liposomes. This can be interpreted as the liposomes more easily transporting over the endothelium, but being more hindered from diffusing further into the tumor interstitium. Exactly the mechanisms for how increased levels of HA could decrease the diffusivity is not clear, but it could be due to steric hindrance between the particles and the long HA molecules. Electrostatic interactions could have contributed to the hindrance but is unlikely since the liposomes were approximately neutral in charge. It could also be the interplay between the HA and other GAGs, and it is difficult to conclude the actual impact of the HA on the uptake and extravasation of the liposomes from this study alone.

5.2.3 Collagen as a Barrier for Nanoparticle Delivery

No significant correlation between the uptake and collagen area fraction was found for all the tumors pooled together, but the CT26 tumors showed a significant positive correlation with a p-value of 0.2531. This means that an increased area fraction of collagen corresponded with increased uptake of the liposomes in the CT26 tumors. Similarly to the correlation for the HA vs uptake, this is the opposite of the established literature [80, 4]. There were no significant correlations or trends between the collagen and the extravasation distances of the liposomes.

To study how collagen can affect NP drug delivery in tumors, Torosean et al. characterized collagen and uptake in pancreatic adenocarcinoma, rat gliosarcoma, and human epithelial cancer in mice [81]. They found that a high presence of collagen appeared as a prominent barrier in NP delivery, but whether it was the collagen directly or the increased collagen-controlled IFP was difficult to conclude. Another study by Eikenes et al. was done to look at how the degradation of collagen by collagenases could affect the uptake and distribution of monoclonal antibodies in sc OHS tumors [82]. Collagenases are enzymes that break down collagen [83]. Eikenes found that decreased amounts of collagen improved the uptake and distribution of the antibodies. In the already mentioned multi-modal characterization paper by Sulheim et al. they also examined how NP accumulation correlated with collagen area fractions [70]. They found no significant correlation, but tumors with the highest collagen content showed the lowest NP accumulation.

There seems to be a consensus in the literature that collagen can contribute to decreased uptake and penetration of NPs and drugs in tumors, but the exact mechanism is not clear here either. As mentioned in Section 2.4.1, a direct effect that can decrease the transport in the tumor interstitium is a steric hindrance from the relatively large collagen fibers in comparison to the nanoparticles. In addition, indirect effects like increasing the solid stress in the tumor which promotes fibroblast to CAF transformation, and increasing IFP could also contribute to the decreased drug delivery. In this study, however, there are no clear conclusions that collagen measured by SHG decreases the uptake or extravasation distance significantly.

5.2.4 Cell Density as a Barrier for Nanoparticle Delivery

No significant correlations were found between the uptake of the liposomes and the cell density. However, a significant negative correlation was found between the mean extravasation distances of the liposomes and the cell density for all the tumors pooled together, and also for the CT26 tumors alone. This is in accordance with some reports in the literature [84].

Sulheim et al. also studied the correlation between cell density and NP accumulation in the five aforementioned tumor models [70]. No significant correlation or even trends were found. Although, the A431 tumors had the highest diffusivity and the lowest cell and collagen density. In 2001 Zheng et al. reported their study looking at the penetration of doxorubicin in prostate tumors [85]. The spatial drug distribution in frozen tumor sections was studied using fluorescent microscopy, and correlated with cell density studies of corresponding H&E stained sections. They found that a higher cell density corresponded with lower drug accumulation.

So, the significant negative correlation in this work can be substantiated by some literature. Intuitively, it makes sense that NPs or drugs will have a more inhibited transport in tumor tissues with densely packed cells than in tumor tissue with less dense packing. This will in turn could contribute to the decreased extravasation distance of NPs.

5.3 Effect of USMB Treatment on Liposome Uptake and Extravasation Distance

5.3.1 Effect of USMB Treatment on Uptake of Liposomes

Looking at the timeline of the uptake of the liposomes in Figure 4.7 there is a small increase in the mean fluorescence that can be observed for the treated 4T1 and KPC tumors after the USMB treatment. Interestingly, the control tumors also exhibit this same peak. Thus, it is unlikely that this increase is due to the USMB treatment and is more likely due to the liposomes naturally accumulating while in circulation and a contribution from the EPR effect. The CT26 tumors did not have this peak and the curves for the treated and control tumors were almost identical. No significant differences were found between the treated and control group at the individual time points either. This is substantiated by the ex-vivo uptake as well in Figure 4.8, where no significant differences were found between the control and treated groups.

In the literature, several ultrasound-mediated drug and nanoparticle uptake studies have been done for different tumor models. In 2017, Snipstad et al. investigated the delivery and therapeutic effect of nanoparticle-stabilized microbubbles in sc triple-negative human breast cancer tumors [86]. The NPs were fluorescently labeled, and the mean fluorescence intensity in tumor sections of the USMB-treated tumors was 2.3 times higher than the control sections. In 2020, they followed up with a similar study where they evaluated the uptake of free and NP-encapsulated cabazitaxel using USMB

treatment in sc prostate adenocarcinoma tumors [87]. They studied the biodistribution of the NPs by using a Pearl scanner before and after treatment for three rounds of treatment spanning 3 weeks. In addition, they looked at the biodistribution 2 and 4 weeks after the last treatment. It was found that the USMB treatment enhanced the uptake from the first treatment and all subsequent treatments.

Our results are not in accordance with the literature since the uptake of liposomes did not increase in the treated tumors. Conversely, there seems to be an effect of the USMB when looking at the increased mean extravasation distances from the blood vessels. An important reason for this discrepancy could be that the uptake measures liposomes in the blood vessels as well as the interstitium while extravasation distance only is measured from extravascular liposomes. Local effects of the USMB could have also contributed to this discrepancy. Only the tissue surrounding the blood vessels with microbubbles that start oscillating would benefit from the USMB treatment. Due to this, local effects of the USMB could be more likely to be observed on the extravasation distances than effects on the entire tumor uptake.

5.3.2 Effect of USMB Treatment on Extravasation of Liposomes Into the Tumor Interstitium

Mean Extravasation Distance Into the Tumor Interstitium

When looking at the mean extravasation distances of NP clusters for the three tumor models in Figure 4.13, the USMB seems to have increased the penetration distance of the NPs into the tumor interstitium. Although it is only statistically significant between the treated and control group for the 4T1 tumors, the trend with a higher mean extravasation distance of the liposomes in the treated tumors is observed for the CT26 tumors as well. The KPC tumors seem to have had little to no effect from the USMB with very similar mean extravasation distances for the treated and control. The reason for this could be that the larger area fractions of HA and collagen found in the KPC sections create a dense ECM barrier that hinders the transport in the interstitium.

The mechanisms for the USMB treatment increasing the mean extravasation distance of the liposomes into the tumor interstitium could start with acoustic streaming pushing the liposomes and MBs closer to the endothelial wall [10, 37]. Here, the MBs would start oscillating and creating microstreams. These microstreams together with the physical expansion of the MBs at the blood vessel wall could have created small pores between the endothelial cells or even created pores in the cell membranes themselves. Through these pores, the liposomes could have extravasated into the tumor interstitium. If the cavitation effects of the MBs were strong enough, the MBs could have collapsed which could have caused a microjet that pierced the endothelial wall and sent the liposomes into the tumor interstitium.

USMB treatment could also potentially have changed the ECM organization in the tumors. While no differences were observed between the treated or control sections with the SHG F/B ratio, that does not mean there were no local changes in the

collagen structure. There is a limit to the spatial resolution of optical imaging and thus, the changes could have been impossible to detect when imaging the SHG signal. However, since the KPC tumors which had the largest area fractions of collagen and HA had no measurable effect of the USMB treatment one would think that the USMB treatment's effect on the ECM was minuscule, at least for the KPC tumors.

For the 4T1 and CT26 control tumors, the mean extravasation distance was the highest in the center while it was highest in the periphery for the treated tumors. This is interesting since the area fraction of HA and collagen was the highest in the periphery and lowest in the center for these tumors, and thus indicates that the USMB treatment had a larger effect in the periphery than in the center. So, there is a possibility that the USMB reorganized the ECM to increase the penetration distance of the liposomes. Another reason could be due to the periphery in tumors being more well vascularized and thus, having an increased chance of MBs entering the peripheral blood vessels and interacting with the peripheral tissue. Whether the increased penetration distance in the periphery is due to better vascularization or ECM reorganization is difficult to conclude with this study, but would be interesting to look at in future studies.

Fraction of NP Clusters at Increasing Extravasation Distances from BVs

In addition to plotting the mean extravasation distance, the fraction of NP clusters as a function of extravasation distance was studied as shown in Section 4.5.2. It was found that the fraction of NP clusters between 0-10 μm was higher for the 4T1 and KPC sections than in the CT26 sections. This could mean that the NPs had a harder time penetrating into the tumor interstitium of the 4T1 and KPC tumors, than in the CT26 tumors. Indicating again, that the more HA and collagen-rich tumors had lower extravasation distances. There were not any significant differences between the treated and control sections. A trend however was that the treated sections included more peaks and the fraction of NP cluster did not gradually decline further from the BVs. It is difficult to conclude whether these peaks actually were due to increased penetration from USMB treatment. One possible explanation for the peaks is that the NP clusters identified at these distances originated from blood vessels that were closed at the time of the FITC-lectin injection or originated from blood vessels above or under the section imaged. To address this, all NP clusters at 200 μm and beyond were disregarded as originating from other BVs and not included in the analysis.

Another master's student, Kastellet, also investigated the extravasation of liposomes in CT26 sections from the same tumors and levels as this work [75]. Kastellet did not find a difference between the mean extravasation distance of the liposomes for the treated and control groups whereas this work found a doubled mean extravasation distance for the treated sections compared to the control sections. Kastellet also reported that around 7-16 % of the NP clusters were 0-10 μm from the blood vessels. These are large discrepancies compared to this work. She used a different microscope, but other than that the sample preparation and image processing was the same. It could have been a difference with the microscope, but more likely it is due to tumor

heterogeneity. Since she studied 1 section each from 8 more tumors, and because of large intravariation in tumors this could have contributed to the differences. It is clear, however, that more sections need to be analyzed to conclude what lead to this discrepancy.

In 2020, Olsman et al. did a similar study that investigated the extravasation distance of liposomes after USMB treatment in sc prostate adenocarcinoma in mice [88]. They found a significantly increased amount of NP clusters in the USMB-treated groups compared to the control groups. They also studied the average area of pixels representing liposomes per image as a function of extravasation distance from the nearest blood vessel. In these plots, a shorter extravasation distance was found for the control sections. In addition, the extravasation distance fraction declined down to zero quicker than in both Kastellet's and the author's work. One reason that neither our work nor Kastellet's work reproduced Olsman's results could be that the prostate adenocarcinoma is too different from our tumor models. Another reason could be the higher MI the treatment could have contributed to the differences.

5.4 Future Work

To be able to conclude on the most important barriers for ultrasound-mediated delivery of liposomes into the tumor interstitium, more experiments are needed. There are 8 other tumors in each of the tumor model groups that were not imaged and could help to illuminate the differences in the ECM composition of the tumors, and how this affects the penetration of liposomes to the tumor interstitium. Because of tumor heterogeneity, it would also be beneficial to look at several sections from the same tumor.

If similar experiments are to be repeated, it would be beneficial if the tumors were more similar in size. This is not easy to control as the growth kinetics of tumors depend on the cells implanted and the host animal. However, with the amount of ECM constituents correlating strongly and significantly with tumor weight, it could be a crucial part of substantiating how different tumor models respond to different treatments.

A more specific idea for future studies is looking at thicker samples for the collagen and HA area fractions. Thicker samples could perhaps illuminate more clearly the structure and composition of the ECM, especially regarding the ordered and unordered structural organization of collagen.

It is important to emphasize what future implications studies like these could have for the treatment of cancer. There is a huge potential for personalized cancer treatment based on the biomarkers found in the individual patient to have optimal efficacy. Identifying the most important biomarkers could be crucial for a curative outcome. In this work, the biomarkers in question are the amounts of collagen and hyaluronic acid. Some trends were found that substantiated that these ECM components could predict treatment efficacy of USMB treatment. Thus, with studies like these, we are one step closer to understanding how to increase the efficacy of cancer treatment.

Chapter 6

Conclusion

One of the main aims of this project was to characterize the ECM in the 4T1, CT26, and KPC tumor models. This work found that the KPC tumors had higher mean collagen area fractions than the 4T1 and CT26 tumors with the CT26 tumors having the lowest area fraction of collagen. The differences were not significant, but there was a clear trend. Additionally, the KPC models also had the highest mean total HA area fraction with the 4T1 tumors having the second highest and the CT26 tumors having significantly lower area fractions of HA than the KPC tumors. When comparing to the literature the range of values reported varied a lot, but the range found in this work was in accordance with some similar studies and seemed plausible.

Another main aim was to identify barriers in the ECM for the extravasation of liposomes into the tumor interstitium. No significant correlations were found between the area fractions of HA and collagen with the mean extravasation distance. However, a trend was that the KPC tumors which had the highest area fraction of HA and collagen also had the lowest mean extravasation distance. The CT26 tumors had the lowest area fraction of both HA and collagen but did not have the highest mean extravasation distance, which was found in the 4T1 tumors. Indicating that the area fractions of HA and collagen alone were not the determining factor for the mean extravasation distance. The lowest cell density was found for the 4T1 sections and a significant negative correlation was found between the cell density and mean extravasation for all the tumors pooled together. This could have been attributed to the highest mean extravasation distances found in the 4T1 tumors. Ultimately, this study indicates that the interplay of many different factors governs how far liposomes can penetrate into the tumor interstitium including the amount of HA and collagen.

The final aim of the project was to look at how USMB treatment could increase the uptake and extravasation distance of liposomes in tumors. The only statistically significant difference was found in the 4T1 periphery between the control and treated tumors. However, a clear trend with increased mean extravasation distance was found for both the 4T1 and CT26 treated tumors. The KPC tumors had little to no effect on the USMB treatment, and one could speculate that this is due to the high area fractions of collagen and HA.

In order to conclude what the main barriers are for ultrasound-mediated delivery of liposomes in these three tumor models, more experiments are needed. These results come from a small sample size and most of the interesting findings are trends and not statistically significant differences. In order for increased therapeutic efficacy of new cancer medicines, it is important to identify biomarkers that can predict the success of

the treatment for each individual patient. This work indicates that HA and collagen in the tumor ECM could be such biomarkers, and more studies are needed to unveil the mechanisms behind how they affect drug delivery.

References

- [1] Stephen Paget. ‘The distribution of secondary growths in cancer of the breast.’ In: *The Lancet* 133.3421 (1889), pp. 571–573.
- [2] Vincent T DeVita Jr and Steven A Rosenberg. ‘Two hundred years of cancer research’. In: *New England Journal of Medicine* 366.23 (2012), pp. 2207–2214.
- [3] Jacques Ferlay et al. ‘Global cancer observatory: cancer today’. In: *Lyon, France: international agency for research on cancer* 3.20 (2020), p. 2019.
- [4] Erik Henke, Rajender Nandigama and Süleyman Ergün. ‘Extracellular matrix in the tumor microenvironment and its impact on cancer therapy’. In: *Frontiers in molecular biosciences* 6 (2020), p. 160.
- [5] Borros Arneth. ‘Tumor microenvironment’. In: *Medicina* 56.1 (2019), p. 15.
- [6] Sylvie Brassart-Pasco et al. ‘Tumor microenvironment: extracellular matrix alterations influence tumor progression’. In: *Frontiers in oncology* 10 (2020), p. 397.
- [7] Sandra N Ekdawi, David A Jaffray and Christine Allen. ‘Nanomedicine and tumor heterogeneity: Concept and complex reality’. In: *Nano Today* 11.4 (2016), pp. 402–414.
- [8] Guoxiang Liu et al. ‘A Review on drug delivery system for tumor therapy’. In: *Frontiers in Pharmacology* 12 (2021), p. 735446.
- [9] Dnyaneshwar Kalyane et al. ‘Employment of enhanced permeability and retention effect (EPR): Nanoparticle-based precision tools for targeting of therapeutic and diagnostic agent in cancer’. In: *Materials Science and Engineering: C* 98 (2019), pp. 1252–1276.
- [10] Sofie Snipstad et al. ‘Ultrasound and microbubbles to beat barriers in tumors: Improving delivery of nanomedicine’. In: *Advanced Drug Delivery Reviews* 177 (2021), p. 113847.
- [11] Jeff Hardin, Gregory Bertoni and Lewis J. Kleinsmith. *Beckers world of the cell*. Pearson Education, 2018.
- [12] Douglas Hanahan and Robert A Weinberg. ‘The hallmarks of cancer’. In: *cell* 100.1 (2000), pp. 57–70.
- [13] Douglas Hanahan and Robert A Weinberg. ‘Hallmarks of cancer: the next generation’. In: *cell* 144.5 (2011), pp. 646–674.
- [14] Douglas Hanahan. ‘Hallmarks of cancer: new dimensions’. In: *Cancer discovery* 12.1 (2022), pp. 31–46.

- [15] Marion De Jong and Theodosia Maina. ‘Of mice and humans: Are they the same?—Implications in cancer translational research’. In: *Journal of Nuclear Medicine* 51.4 (2010), pp. 501–504.
- [16] Beverly A Teicher. ‘Tumor models for efficacy determination’. In: *Molecular cancer therapeutics* 5.10 (2006), pp. 2435–2443.
- [17] Beth A Pulaski and Suzanne Ostrand-Rosenberg. ‘Mouse 4T1 breast tumor model’. In: *Current protocols in immunology* 39.1 (2000), pp. 20–2.
- [18] Saba Malekian et al. ‘Expression of diverse angiogenesis factor in different stages of the 4T1 tumor as a mouse model of triple-negative breast cancer’. In: *Advanced Pharmaceutical Bulletin* 10.2 (2020), p. 323.
- [19] Kai Tao et al. ‘Imagable 4T1 model for the study of late stage breast cancer’. In: *BMC cancer* 8.1 (2008), pp. 1–19.
- [20] DP Griswold and Thomas H Corbett. ‘A colon tumor model for anticancer agent evaluation’. In: *Cancer* 36.S6 (1975), pp. 2441–2444.
- [21] Michael G Brattain et al. ‘Establishment of mouse colonic carcinoma cell lines with different metastatic properties’. In: *Cancer research* 40.7 (1980), pp. 2142–2146.
- [22] John C Castle et al. ‘Immunomic, genomic and transcriptomic characterization of CT26 colorectal carcinoma’. In: *BMC genomics* 15.1 (2014), pp. 1–12.
- [23] Sunil R Hingorani et al. ‘Preinvasive and invasive ductal pancreatic cancer and its early detection in the mouse’. In: *Cancer cell* 4.6 (2003), pp. 437–450.
- [24] Jae W Lee et al. ‘Genetically engineered mouse models of pancreatic cancer: the KPC model (LSL-KrasG12D/+; LSL-Trp53R172H/+; Pdx-1-Cre), its variants, and their application in immuno-oncology drug discovery’. In: *Current protocols in pharmacology* 73.1 (2016), pp. 14–39.
- [25] Håkon Fosslund Wesche. ‘Characterization of extracellular matrix constituents in three murine tumor models’. Project thesis. Norwegian University of Science and Technology, 2023.
- [26] Kristine Y DeLeon-Pennell, Thomas H Barker and Merry L Lindsey. ‘Fibroblasts: The arbiters of extracellular matrix remodeling’. In: *Matrix Biology* 91 (2020), pp. 1–7.
- [27] Min Fang et al. ‘Collagen as a double-edged sword in tumor progression’. In: *Tumor Biology* 35 (2014), pp. 2871–2882.
- [28] Jarett Casale and Jonathan S Crane. ‘Biochemistry, glycosaminoglycans’. In: (2019).
- [29] Andreas Wicki et al. ‘Nanomedicine in cancer therapy: challenges, opportunities, and clinical applications’. In: *Journal of controlled release* 200 (2015), pp. 138–157.
- [30] Daniela Iannazzo et al. ‘Recent advances in nanotherapeutics for multiple myeloma’. In: *Cancers* 12.11 (2020), p. 3144.

- [31] Hans-Peter Gerber, Peter D Senter and Iqbal S Grewal. ‘Antibody drug-conjugates targeting the tumor vasculature: current and future developments’. In: *MABs*. Vol. 1. 3. Taylor & Francis. 2009, pp. 247–253.
- [32] Erik Sahai et al. ‘A framework for advancing our understanding of cancer-associated fibroblasts’. In: *Nature Reviews Cancer* 20.3 (2020), pp. 174–186.
- [33] Triantafyllos Stylianopoulos, Lance L Munn and Rakesh K Jain. ‘Reengineering the physical microenvironment of tumors to improve drug delivery and efficacy: from mathematical modeling to bench to bedside’. In: *Trends in cancer* 4.4 (2018), pp. 292–319.
- [34] Triantafyllos Stylianopoulos et al. ‘Causes, consequences, and remedies for growth-induced solid stress in murine and human tumors’. In: *Proceedings of the National Academy of Sciences* 109.38 (2012), pp. 15101–15108.
- [35] Saroja Ramanujan et al. ‘Diffusion and convection in collagen gels: implications for transport in the tumor interstitium’. In: *Biophysical journal* 83.3 (2002), pp. 1650–1660.
- [36] Triantafyllos Stylianopoulos et al. ‘Diffusion of particles in the extracellular matrix: the effect of repulsive electrostatic interactions’. In: *Biophysical journal* 99.5 (2010), pp. 1342–1349.
- [37] William G Pitt, Ghaleb A Hussein and Bryant J Staples. ‘Ultrasonic drug delivery—a general review’. In: *Expert opinion on drug delivery* 1.1 (2004), pp. 37–56.
- [38] Atin Saha and Mahan Mathur. ‘Ultrasound Physics & Overview’. In: *Ultrasound Fundamentals: An Evidence-Based Guide for Medical Practitioners* (2021), pp. 3–16.
- [39] William D O’Brien Jr. ‘Ultrasound–biophysics mechanisms’. In: *Progress in biophysics and molecular biology* 93.1-3 (2007), pp. 212–255.
- [40] Pascal Laugier and Guillaume Haiat. ‘Introduction to the physics of ultrasound’. In: *Bone quantitative ultrasound* (2011), pp. 29–45.
- [41] Vincent Chan and Anahi Perlas. ‘Basics of ultrasound imaging’. In: *Atlas of ultrasound-guided procedures in interventional pain management* (2011), pp. 13–19.
- [42] SB Barnett et al. ‘Current status of research on biophysical effects of ultrasound’. In: *Ultrasound in medicine & biology* 20.3 (1994), pp. 205–218.
- [43] Charles C Church. ‘Frequency, pulse length, and the mechanical index’. In: *Acoustics Research Letters Online* 6.3 (2005), pp. 162–168.
- [44] Taner Şen, Omaç Tüfekçioğlu and Yavuzer Koza. ‘Mechanical index’. In: *Anatolian journal of cardiology* 15.4 (2015), p. 334.
- [45] Charlotte Årseth. ‘Effect of Ultrasound and Microbubbles on Vasculature and Extracellular Matrix Components in Murine Breast Cancer Tumors’. Master thesis. Norwegian University of Science and Technology, 2022.

- [46] Ralph M Albrecht and Julie A Oliver. ‘Labeling considerations for confocal microscopy’. In: *Basic Confocal Microscopy* (2018), pp. 99–134.
- [47] Andrew H Fischer et al. ‘Hematoxylin and eosin staining of tissue and cell sections’. In: *Cold spring harbor protocols* 2008.5 (2008), pdb-prot4986.
- [48] Cassandra Ceccopieri, Joanna Skonieczna and Jan P Madej. ‘Modification of a haematoxylin, eosin, and natural saffron staining method for the detection of connective tissue’. In: *Journal of Veterinary Research* 65.1 (2021), pp. 125–130.
- [49] Erik Edston and Liv Gröntoft. ‘Saffron—A connective tissue counterstain in routine pathology’. In: *Journal of histotechnology* 20.2 (1997), pp. 123–125.
- [50] Farial A Tanious et al. ‘DAPI (4’, 6-diamidino-2-phenylindole) binds differently to DNA and RNA: minor-groove binding at AT sites and intercalation at AU sites’. In: *Biochemistry* 31.12 (1992), pp. 3103–3112.
- [51] Claire E Chivers et al. ‘How the biotin–streptavidin interaction was made even stronger: investigation via crystallography and a chimaeric tetramer’. In: *Biochemical Journal* 435.1 (2011), pp. 55–63.
- [52] W Gray Jerome. ‘The theory of fluorescence’. In: *Basic confocal microscopy* (2018), pp. 21–36.
- [53] W Gray Jerome and Robert L Price. ‘Fluorescence Microscopy’. In: *Basic Confocal Microscopy* (2018), pp. 37–71.
- [54] Amicia D Elliott. ‘Confocal microscopy: principles and modern practices’. In: *Current protocols in cytometry* 92.1 (2020), e68.
- [55] John Fuseler, W Gray Jerome and Robert L Price. ‘Types of confocal instruments: Basic principles and advantages and disadvantages’. In: *Basic confocal microscopy* (2018), pp. 187–213.
- [56] Adaobi Nwaneshiudu et al. ‘Introduction to confocal microscopy’. In: *Journal of Investigative Dermatology* 132.12 (2012), pp. 1–5.
- [57] Volker Schweikhard et al. ‘The Power HyD family of detectors for confocal microscopy’. In: *NATURE METHODS* (2020).
- [58] Xiyi Chen et al. ‘Second harmonic generation microscopy for quantitative analysis of collagen fibrillar structure’. In: *Nature protocols* 7.4 (2012), pp. 654–669.
- [59] Johannes Schindelin et al. ‘Fiji: an open-source platform for biological-image analysis’. In: *Nature methods* 9.7 (2012), pp. 676–682.
- [60] Andriy Marusyk and Kornelia Polyak. ‘Tumor heterogeneity: causes and consequences’. In: *Biochimica et Biophysica Acta (BBA)-Reviews on Cancer* 1805.1 (2010), pp. 105–117.
- [61] Adriana Albini et al. ‘Cancer stem cells and the tumor microenvironment: interplay in tumor heterogeneity’. In: *Connective tissue research* 56.5 (2015), pp. 414–425.

- [62] Derek J Erstad et al. ‘Orthotopic and heterotopic murine models of pancreatic cancer and their different responses to FOLFIRINOX chemotherapy’. In: *Disease models & mechanisms* 11.7 (2018), p. dmm034793.
- [63] C Davies et al. ‘Uptake of IgG in osteosarcoma correlates inversely with interstitial fluid pressure, but not with interstitial constituents’. In: *British journal of cancer* 85.12 (2001), pp. 1968–1977.
- [64] Joao Incio et al. ‘Metformin reduces desmoplasia in pancreatic cancer by reprogramming stellate cells and tumor-associated macrophages’. In: *PloS one* 10.12 (2015), e0141392.
- [65] Emma L Reeves et al. ‘Investigating the contribution of hyaluronan to the breast tumour microenvironment using multiparametric MRI and MR elastography’. In: *Molecular Oncology* (2023).
- [66] Chrysovalantis Voutouri and Triantafyllos Stylianopoulos. ‘Accumulation of mechanical forces in tumors is related to hyaluronan content and tissue stiffness’. In: *PloS one* 13.3 (2018), e0193801.
- [67] Andreas G Hadjigeorgiou and Triantafyllos Stylianopoulos. ‘Evaluation of growth-induced, mechanical stress in solid tumors and spatial association with extracellular matrix content’. In: *Biomechanics and Modeling in Mechanobiology* (2023), pp. 1–19.
- [68] Marvin Schober et al. ‘Desmoplasia and chemoresistance in pancreatic cancer’. In: *Cancers* 6.4 (2014), pp. 2137–2154.
- [69] Camilla Bang. ‘Using atomic force microscopy and second harmonic generation to investigate the effects of ultrasound and microbubbles on the extracellular matrix in 4t1 breast tumors.’ Master thesis. Norwegian University of Science and Technology, 2022.
- [70] Einar Sulheim et al. ‘Multi-modal characterization of vasculature and nanoparticle accumulation in five tumor xenograft models’. In: *Journal of controlled release* 279 (2018), pp. 292–305.
- [71] Andreas Stylianou et al. ‘Pancreatic Cancer Presents Distinct Nanomechanical Properties During Progression’. In: *Annals of Biomedical Engineering* (2023), pp. 1–14.
- [72] Xiaoxing Han et al. ‘Second harmonic properties of tumor collagen: determining the structural relationship between reactive stroma and healthy stroma.’ In: *Optics express* 16.3 (2008), pp. 1846–1859.
- [73] Kathleen Burke, Ping Tang and Edward Brown. ‘Second harmonic generation reveals matrix alterations during breast tumor progression’. In: *Journal of biomedical optics* 18.3 (2013), pp. 031106–031106.
- [74] Vashendriya VV Hira et al. ‘Comparison of different methodologies and cryostat versus paraffin sections for chromogenic immunohistochemistry’. In: *Acta histochemica* 121.2 (2019), pp. 125–134.

- [75] Andrea Berge Kastellet. ‘Effect of Ultrasound and Microbubbles on Tumor Vasculature and Liposomal uptake in Murine Cancer Models’. Master thesis. Norwegian University of Science and Technology, 2023.
- [76] Md Abdus Subhan et al. ‘Recent advances in tumor targeting via EPR effect for cancer treatment’. In: *Journal of personalized medicine* 11.6 (2021), p. 571.
- [77] Michael A Jacobetz et al. ‘Hyaluronan impairs vascular function and drug delivery in a mouse model of pancreatic cancer’. In: *Gut* 62.1 (2013), pp. 112–120.
- [78] L Eikenes et al. ‘Hyaluronidase induces a transcapillary pressure gradient and improves the distribution and uptake of liposomal doxorubicin (Caelyx™) in human osteosarcoma xenografts’. In: *British journal of cancer* 93.1 (2005), pp. 81–88.
- [79] Hyunwook Jung. ‘Hyaluronidase: An overview of its properties, applications, and side effects’. In: *Archives of plastic surgery* 47.04 (2020), pp. 297–300.
- [80] John A Conti et al. ‘The desmoplastic reaction surrounding hepatic colorectal adenocarcinoma metastases aids tumor growth and survival via αv integrin ligation’. In: *Clinical Cancer Research* 14.20 (2008), pp. 6405–6413.
- [81] Sason Torosean et al. ‘Nanoparticle uptake in tumors is mediated by the interplay of vascular and collagen density with interstitial pressure’. In: *Nanomedicine: Nanotechnology, Biology and Medicine* 9.2 (2013), pp. 151–158.
- [82] Live Eikenes et al. ‘Collagenase increases the transcapillary pressure gradient and improves the uptake and distribution of monoclonal antibodies in human osteosarcoma xenografts’. In: *Cancer research* 64.14 (2004), pp. 4768–4773.
- [83] Hamzeh Alipour et al. ‘Therapeutic applications of collagenase (metalloproteases): A review’. In: *Asian Pacific Journal of Tropical Biomedicine* 6.11 (2016), pp. 975–981.
- [84] JL-S Au et al. ‘Determinants of drug delivery and transport to solid tumors’. In: *Journal of controlled release* 74.1-3 (2001), pp. 31–46.
- [85] Jenny H Zheng et al. ‘Time- and concentration-dependent penetration of doxorubicin in prostate tumors’. In: *Aaps Pharmsci* 3 (2001), pp. 69–77.
- [86] Sofie Snipstad et al. ‘Ultrasound improves the delivery and therapeutic effect of nanoparticle-stabilized microbubbles in breast cancer xenografts’. In: *Ultrasound in medicine & biology* 43.11 (2017), pp. 2651–2669.
- [87] Sofie Snipstad et al. ‘Sonopermeation enhances uptake and therapeutic effect of free and encapsulated cabazitaxel’. In: *Ultrasound in Medicine & Biology* 47.5 (2021), pp. 1319–1333.
- [88] Marieke Olsman et al. ‘Ultrasound-mediated delivery enhances therapeutic efficacy of MMP sensitive liposomes’. In: *Journal of controlled release* 325 (2020), pp. 121–134.

Appendix A

Data for plots

A.1 Tumor Weights

Table A.1: Overview over the ex vivo weight of the tumors. Tumor Section columns describe what tumor model, whether it was in the treated (T) or control (C) group and the number is to differentiate between the tumors.

Tumor Section	Weight [g]
4T1 T1	0.542
4T1 T2	0.574
4T1 T3	0.593
4T1 C1	0.513
4T1 C2	0.516
4T1 C3	0.450
CT26 T4	0.880
CT26 T5	1.030
CT26 T6	1.570
CT26 C4	0.688
CT26 C5	0.910
CT26 C6	1.350
KPC T7	0.096
KPC T8	0.100
KPC T9	0.072
KPC C7	0.108
KPC C8	0.093
KPC C9	0.104

A.2 Hyaluronic Acid Area Fraction Data

Table A.2: Hyaluronic acid area fraction data. Tumor Section columns describe what tumor model, whether it was in the treated (T) or control (C) group and the number is to differentiate between the sections. The mean and standard deviation are given for each group in its own row.

Tumor Section	Total [%]	Periphery [%]	Center [%]
4T1 T1	15.85	19.82	14.8
4T1 T2	23.75	32.36	21.63
4T1 T3	12.43	23.99	9.56
4T1 C1	35.13	59.89	28.59
4T1 C2	44.12	64.38	39.34
4T1 C3	25.50	39.62	22.08
4T1 Mean and STD	26.13±11.87	40.01±18.50	22.67±10.47
CT26 T4	19.15	45.28	12.78
CT26 T5	18.82	23.68	17.58
CT26 T6	6.60	12.49	4.65
CT26 C4	11.20	22.59	8.60
CT26 C5	13.91	27.24	10.64
CT26 C6	6.66	11.32	5.13
CT26 Mean and STD	12.72±5.59	23.77±12.32	9.90±4.90
KPC T7	38.02	31.36	39.55
KPC T8	22.05	15.51	23.81
KPC T9	29.34	25.45	30.29
KPC C7	48.55	49.28	48.37
KPC C8	35.68	37.10	35.32
KPC C9	41.59	40.00	41.72
KPC Mean and STD	35.87±9.29	33.12±11.80	36.51±8.70

A.3 Collagen Forward Area Fraction Data

Table A.3: Collagen forward area fraction data. Tumor Section columns describe what tumor model, whether it was in the treated (T) or control (C) group and the number is to differentiate between the sections. The mean and standard deviation are given for each group in its own row.

Tumor Section	Total [%]	Periphery [%]	Center [%]
4T1 T1	1.74	4.85	0.94
4T1 T2	1.29	3.23	0.81
4T1 T3	0.61	1.98	0.29
4T1 C1	1.81	5.42	0.84
4T1 C2	1.61	3.27	0.94
4T1 C3	1.04	3.86	0.48
4T1 Mean and STD	1.35±0.46	3.77±1.24	0.72±0.27
CT26 T4	0.82	3.66	0.13
CT26 T5	1.23	3.86	0.54
CT26 T6	0.41	1.41	0.16
CT26 C4	0.21	0.99	0.01
CT26 C5	0.73	3.33	0.09
CT26 C6	0.44	1.53	0.08
CT26 Mean and STD	0.64±0.37	2.46±1.29	0.17±0.19
KPC T7	8.37	21.62	5.26
KPC T8	1.21	2.90	0.76
KPC T9	0.96	2.32	0.63
KPC C7	9.49	32.00	3.99
KPC C8	7.80	19.01	4.96
KPC C9	4.45	13.42	3.42
KPC Mean and STD	5.38±3.73	15.21±11.47	3.17±2.03

A.4 Collagen Backward Area Fraction Data

Table A.4: Collagen backward area fraction data. Tumor Section columns describe what tumor model, whether it was in the treated (T) or control (C) group and the number is to differentiate between the sections. The mean and standard deviation are given for each group in its own row.

Tumor Section	Total [%]	Periphery [%]	Center [%]
4T1 T1	1.44	6.03	1.03
4T1 T2	1.87	5.19	1.06
4T1 T3	0.65	2.23	0.29
4T1 C1	2.62	7.55	1.25
4T1 C2	1.83	3.27	1.32
4T1 C3	0.90	3.20	0.31
4T1 Mean and STD	1.55±0.72	4.58±2.02	0.88±0.46
CT26 T4	0.94	4.16	0.15
CT26 T5	1.35	4.25	0.68
CT26 T6	0.37	1.33	0.09
CT26 C4	0.19	1.07	0.01
CT26 C5	0.62	3.00	0.05
CT26 C6	0.46	1.64	0.07
CT26 Mean and STD	0.66±0.42	2.58±1.43	0.18±0.25
KPC T7	9.62	22.11	6.68
KPC T8	0.63	2.75	0.90
KPC T9	0.41	1.03	0.26
KPC C7	9.45	33.85	3.49
KPC C8	8.25	19.70	5.35
KPC C9	6.27	15.84	4.15
KPC Mean and STD	5.77±4.24	15.88±12.40	3.47±2.50

A.5 F/B Ratio Data

Table A.5: F/B ratio data. Tumor Section columns describe what tumor model, whether it was in the treated (T) or control (C) group and the number is to differentiate between the sections. The mean and standard deviation are given for each group in its own row.

Tumor Section	F/B ratio
4T1 T1	4.35
4T1 T2	4.27
4T1 T3	4.42
4T1 C1	4.96
4T1 C2	5.25
4T1 C3	2.47
4T1 Mean and STD	4.29±0.97
CT26 T4	4.77
CT26 T5	4.39
CT26 T6	4.31
CT26 C4	5.22
CT26 C5	4.92
CT26 C6	4.47
CT26 Mean and STD	4.68±0.35
KPC T7	4.58
KPC T8	2.62
KPC T9	5.19
KPC C7	4.27
KPC C8	4.37
KPC C9	3.96
KPC Mean and STD	4.17±0.86

A.6 Cell Density Data

Table A.6: Cell density data. Tumor Section columns describe what tumor model, whether it was in the treated (T) or control (C) group and the number is to differentiate between the sections. The mean and standard deviation are given for each group in its own row.

Tumor Section	Total [%]	Periphery [%]	Center [%]
4T1 T1	31.64	29.22	32.27
4T1 T2	30.86	14.59	34.86
4T1 T3	36.41	29.29	38.15
4T1 C1	56.90	45.15	60.6
4T1 C2	32.21	25.55	33.86
4T1 C3	66.03	47.17	70.58
4T1 Mean and STD	42.34±15.21	31.83±12.35	44.96±16.23
CT26 T4	57.66	46.14	60.47
CT26 T5	38.32	28.57	40.81
CT26 T6	63.67	56.87	65.85
CT26 C4	69.08	59.33	71.37
CT26 C5	71.71	58.75	74.89
CT26 C6	64.72	62.71	65.39
CT26 Mean and STD	60.86±12.05	52.06±12.81	63.13±12.03
KPC T7	57.03	50.37	58.60
KPC T8	46.49	34.26	49.77
KPC T9	67.02	56.17	69.68
KPC C7	58.88	50.29	60.98
KPC C8	54.53	43.01	57.45
KPC C9	62.22	52.39	64.56
KPC Mean and STD	57.70±7.00	47.75±7.88	60.17±6.76

A.7 Uptake Timeline Data

Table A.7: Uptake timeline data. Tumor Section columns describe what tumor model, whether it was in the treated (T) or control (C) group and the number is to differentiate between the tumors. The mean and standard deviation are given for each group in its own row.

Tumor \ Time [h]	0	0.25	1.25	4.25	24
4T1 T1	0.11	0.098	0.053	0.031	0.031
4T1 T2	0.075	0.073	0.048	0.025	0.028
4T1 T3	0.089	0.104	0.039	0.02	0.02
4T1 T Mean and STD	0.091 \pm 0.018	0.092 \pm 0.016	0.047 \pm 0.007	0.025 \pm 0.006	0.026 \pm 0.006
4T1 C1	0.064	0.072	0.018	0.025	0.028
4T1 C2	0.094	0.095	0.035	0.038	0.044
4T1 C3	0.101	0.096	0.03	0.032	0.04
4T1 C Mean and STD	0.086 \pm 0.020	0.088 \pm 0.014	0.028 \pm 0.009	0.032 \pm 0.007	0.037 \pm 0.008
CT26 T4	0.077	0.057	0.025	0.015	0.019
CT26 T5	0.081	0.045	0.018	0.016	0.032
CT26 T6	0.05	0.064	0.016	0.019	0.021
CT26 T Mean and STD	0.069 \pm 0.017	0.055 \pm 0.010	0.020 \pm 0.005	0.017 \pm 0.002	0.024 \pm 0.007
CT26 C4	0.043	0.043	0.016	0.013	0.017
CT26 C5	0.065	0.049	0.019	0.019	0.018
CT26 C6	0.099	0.05	0.031	0.024	0.02
CT26 C Mean and STD	0.069 \pm 0.028	0.047 \pm 0.004	0.022 \pm 0.008	0.019 \pm 0.006	0.018 \pm 0.002
KPC T7	0.143	0.135	0.114	0.069	0.057
KPC T8	0.154	0.153	0.091	0.085	0.073
KPC T9	-	0.185	0.106	0.086	0.071
KPC T Mean and STD	0.149 \pm 0.008	0.158 \pm 0.025	0.104 \pm 0.012	0.080 \pm 0.010	0.067 \pm 0.009
KPC C7	0.098	0.119	0.046	0.039	0.05
KPC C8	0.143	0.129	0.049	0.035	0.049
KPC C9	0.147	0.178	0.077	0.066	0.076
KPC C Mean and STD	0.129 \pm 0.027	0.142 \pm 0.032	0.057 \pm 0.017	0.047 \pm 0.017	0.058 \pm 0.015

A.8 Uptake Ex Vivo data

Table A.8: Uptake Ex Vivo data. Tumor Section columns describe what tumor model, whether it was in the treated (T) or control (C) group and the number is to differentiate between the tumors. The mean and standard deviation are given for each group in its own row.

Tumor Section	F/B ratio
4T1 T1	0.056
4T1 T2	0.061
4T1 T3	0.045
4T1 T Mean and STD	0.054± 0.008
4T1 C1	0.075
4T1 C2	0.076
4T1 C3	0.066
4T1 C Mean and STD	0.072±0.006
CT26 T4	0.031
CT26 T5	0.045
CT26 T6	0.044
CT26 T Mean and STD	0.040±0.008
CT26 C4	0.042
CT26 C5	0.051
CT26 C6	0.038
CT26 C Mean and STD	0.044±0.007
KPC T7	0.071
KPC T8	0.067
KPC T9	0.072
KPC T Mean and STD	0.070±0.003
KPC C7	0.052
KPC C8	0.053
KPC C9	0.075
KPC C Mean and STD	0.060±0.013

A.9 Mean Extravasation Distance Data

Table A.9: Mean extravasation distance data. Tumor Section columns describe what tumor model, whether it was in the treated (T) or control (C) group and the number is to differentiate between the sections. The mean and standard deviation are given for each group in its own row.

Tumor Section	Total [μm]	Periphery [μm]	Center [μm]
4T1 T1	84.01	97.03	6.56
4T1 T2	40.14	46.22	30.58
4T1 T3	100.99	139.28	40.47
4T1 T Mean and STD	75.04 ± 31.40	94.17 ± 46.60	25.87 ± 17.44
4T1 C1	31.08	24.52	49.75
4T1 C2	38.09	28.24	43.77
4T1 C3	24.48	18.55	61.61
4T1 C Mean and STD	31.22 ± 6.81	23.77 ± 4.89	51.71 ± 9.08
CT26 T4	42.39	41.04	68.07
CT26 T5	79.28	113.48	45.79
CT26 T6	52.52	60.48	29.17
CT26 T Mean and STD	58.06 ± 19.06	71.67 ± 37.49	47.68 ± 19.52
CT26 C4	22.93	21.16	25.76
CT26 C5	21.62	21.16	23.28
CT26 C6	28.68	20.99	55.32
CT26 C Mean and STD	24.41 ± 3.76	21.10 ± 0.10	34.78 ± 17.82
KPC T7	20.00	21.92	16.04
KPC T8	21.06	22.12	16.78
KPC T9	18.74	15.84	31.33
KPC T Mean and STD	19.94 ± 1.16	19.96 ± 3.57	21.38 ± 8.63
KPC C7	22.81	18.18	31.80
KPC C8	28.06	26.32	32.84
KPC C9	20.79	23.07	11.13
KPC C Mean and STD	23.88 ± 3.75	22.52 ± 4.10	25.26 ± 12.25

A.10 Fraction of NP Clusters As A Function Of Extravasation Distances Data

Table A.10: Fraction of NP clusters extravasated from BV at 10 μm increments. Tumor Section columns describe what tumor model, whether it was in the treated (T) or control (C) group and the number is to differentiate between the sections.

Bins [μm]	4T1 T[%]	4T1 C[%]	CT26 T[%]	CT26 C[%]	KPC T[%]	KPC C[%]
0-10	78.88	78.84	60.69	65.83	75.92	79.85
10-20	1.73	6.72	2.59	4.90	6.63	8.88
20-30	4.81	4.49	4.10	6.73	6.63	4.38
30-40	1.97	2.74	1.86	13.54	4.16	1.94
40-50	4.61	1.85	3.98	4.92	2.11	1.41
50-60	1.40	1.16	1.34	1.47	3.06	0.58
60-70	0.46	0.58	5.78	0.39	1.17	1.16
70-80	0.56	0.55	0.58	2.00	0.18	1.28
80-90	0.30	0.74	2.23	0.10	0.06	0.10
90-100	0.64	0.13	0.05	0.01	0.08	0.01
100-110	0.48	0.38	0.06	0.10	0.00	0.18
110-120	1.23	0.10	15.59	0.00	0.00	0.05
120-130	0.24	0.02	0.22	0.00	0.00	0.03
130-140	0.07	0.06	0.53	0.00	0.00	0.00
140-150	0.54	0.34	0.00	0.00	0.00	0.00
150-160	0.14	0.13	0.15	0.00	0.00	0.00
160-170	0.74	0.51	0.25	0.00	0.00	0.00
170-180	0.16	0.07	0.00	0.00	0.00	0.14
180-190	0.90	0.13	0.00	0.00	0.00	0.00
190-200	0.15	0.48	0.00	0.00	0.00	0.00

A.11 Correlation Coefficients and P-values

Table A.11: Correlation coefficients between tumor weights, and area fraction parameters. Samples denote whether this is for all tumor samples, and correlation denotes which two parameters are tested against each other. R is the Pearson correlation coefficient, and p is the statistical power of the correlation.

Samples	Correlation	R	p
All	Weight vs HA	-0,7528	0,0003
All	Weight vs Coll	-0,5976	0,0088
All	Weight vs Cell density	0,0819	0,7467
All	HA vs Coll	0,7265	0,0006
All	HA vs Cell density	-0,0824	0,7452
All	Coll vs Cell density	0,0622	0,8063

Table A.12: Correlation coefficients between tumor uptake, and area fraction parameters. Samples denote whether this is for all tumor samples, and correlation denotes which two parameters are tested against each other. R is the Pearson correlation coefficient, and p is the statistical power of the correlation.

Samples	Correlation	R	p
All	Uptake vs HA	0,7175	0,0008
4T1	Uptake vs HA	0,9456	0,0044
CT26	Uptake vs HA	0,4607	0,3578
KPC	Uptake vs HA	-0,3561	0,4884
All	Uptake vs Coll	0,2531	0,3110
4T1	Uptake vs Coll	0,6804	0,1369
CT26	Uptake vs Coll	0,8732	0,0231
KPC	Uptake vs Coll	-0,6057	0,2026
All	Uptake vs Cell density	-0,2139	0,3941
4T1	Uptake vs Cell density	0,3544	0,4907
CT26	Uptake vs Cell density	-0,6453	0,1664
KPC	Uptake vs Cell density	0,3043	0,5576

Table A.13: Correlation coefficients between the mean extravasation distances, and area fraction parameters. Samples denote whether this is for all tumor samples, and correlation denotes which two parameters are tested against each other. R is the Spearman correlation coefficient, and p is the statistical power of the correlation.

Samples	Correlation	R	p
All	Extravasation vs HA	-0,4551	0,0577
4T1	Extravasation vs HA	-0,7466	0,0882
CT26	Extravasation vs HA	0,4052	0,4255
KPC	Extravasation vs HA	0,2099	0,6898
All	Extravasation vs Coll	-0,2405	0,3365
4T1	Extravasation vs Coll	-0,3801	0,4573
CT26	Extravasation vs Coll	0,7092	0,1146
KPC	Extravasation vs Coll	0,5123	0,2988
All	Extravasation vs Cell density	-0,5666	0,0142
4T1	Extravasation vs Cell density	-0,5486	0,2597
CT26	Extravasation vs Cell density	-0,9298	0,0072
KPC	Extravasation vs Cell density	-0,3667	0,4747

Appendix B

Images

The images in this section are to serve as visual examples of the images analyzed in this work. All images in this section have been processed in FIJI.

The tile scans have an adjusted brightness and contrast to emphasize the features in the images. A Median filter with 2 pixels selected was used for the SHG/collagen images to subtract some noise in the background due to the linear accumulation. The tile scans chosen are representative of their tumor model group but were chosen arbitrarily.

The blood vessel and nanoparticle images were also chosen arbitrarily. The variation between the images in each tumor was huge and there were no apparent visual characteristics that could separate the tumor models from each other from the author's perspective. These images are just to show some variation found in these images. The brightness and contrast have been adjusted. Figure B.4 shows an image with a very strong NP signal. When these images were thresholded usually only the strongest signals were left, but clusters like this were in some of the images. Figures B.4 and B.5 are images from the center of the tumors, while Figure B.6 is from the periphery of a tumor.

B.1 4T1 Tile Scan

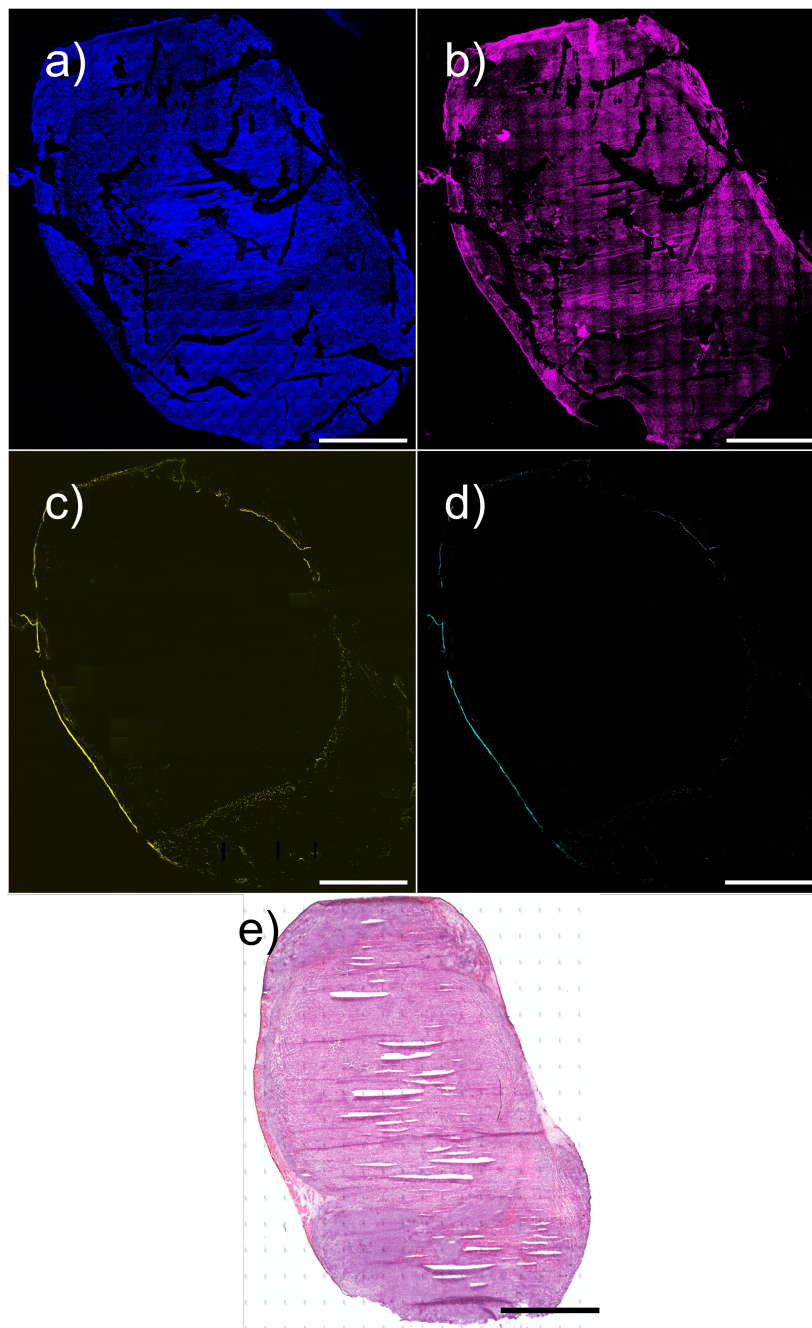


Figure B.1: Example of tile scans with 4T1 section T1. a) is the cell density tile scan, b) is the HA tile scan, c) is the collagen forward tile scan, and d) is the collagen backward tile scan. e) is the HES tile scan from the same tumor level. Brightness and contrast have been adjusted in the images. All scale bars are 2000 μm .

B.2 CT26 Tile Scan

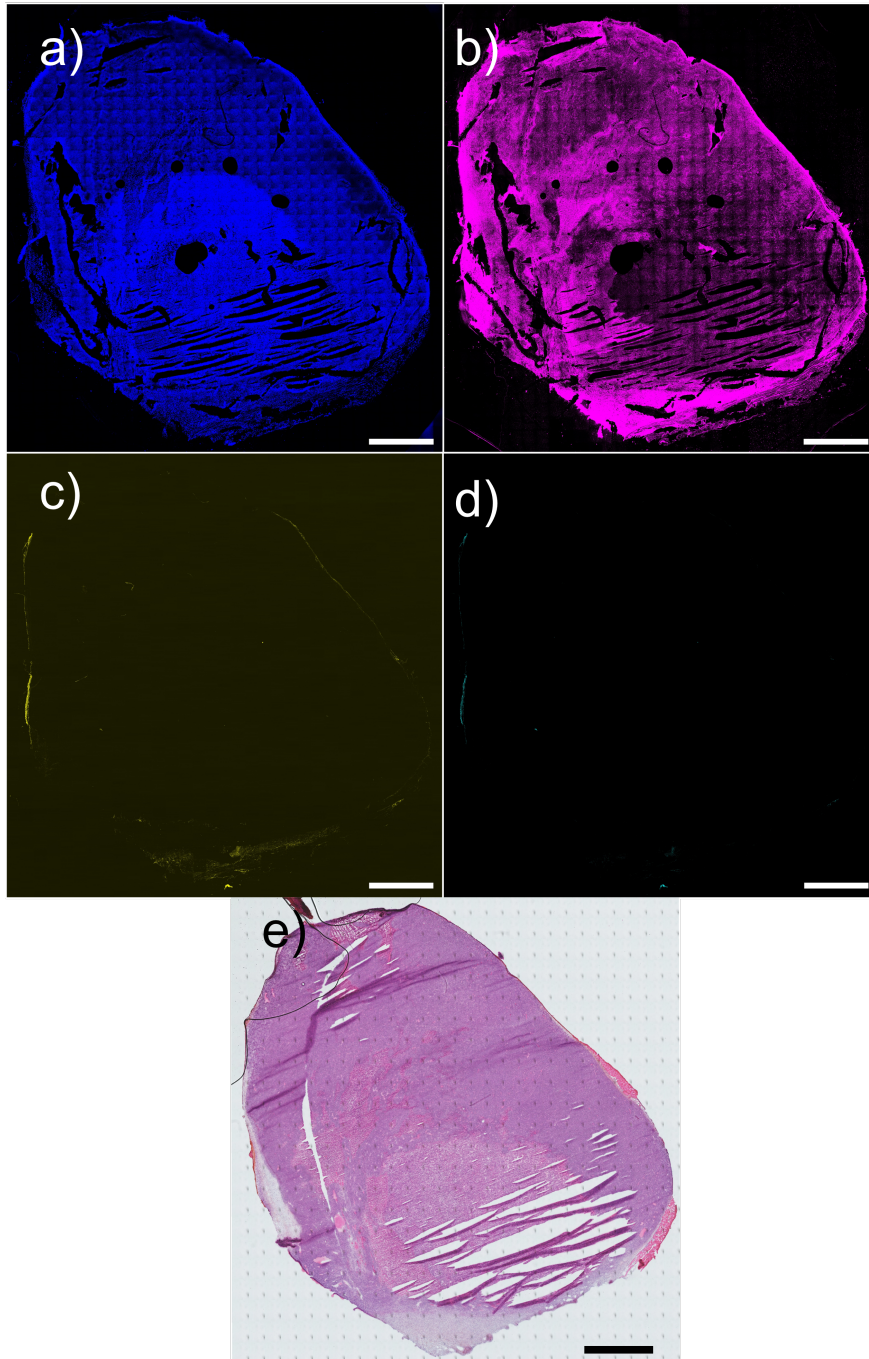


Figure B.2: Example of tile scans with CT26 section T4. a) is the cell density tile scan, b) is the HA tile scan, c) is the collagen forward tile scan, and d) is the collagen backward tile scan. e) is the HES tile scan from the same tumor level. Brightness and contrast have been adjusted in the images. All scale bars are 2000 μm .

B.3 KPC Tile Scan

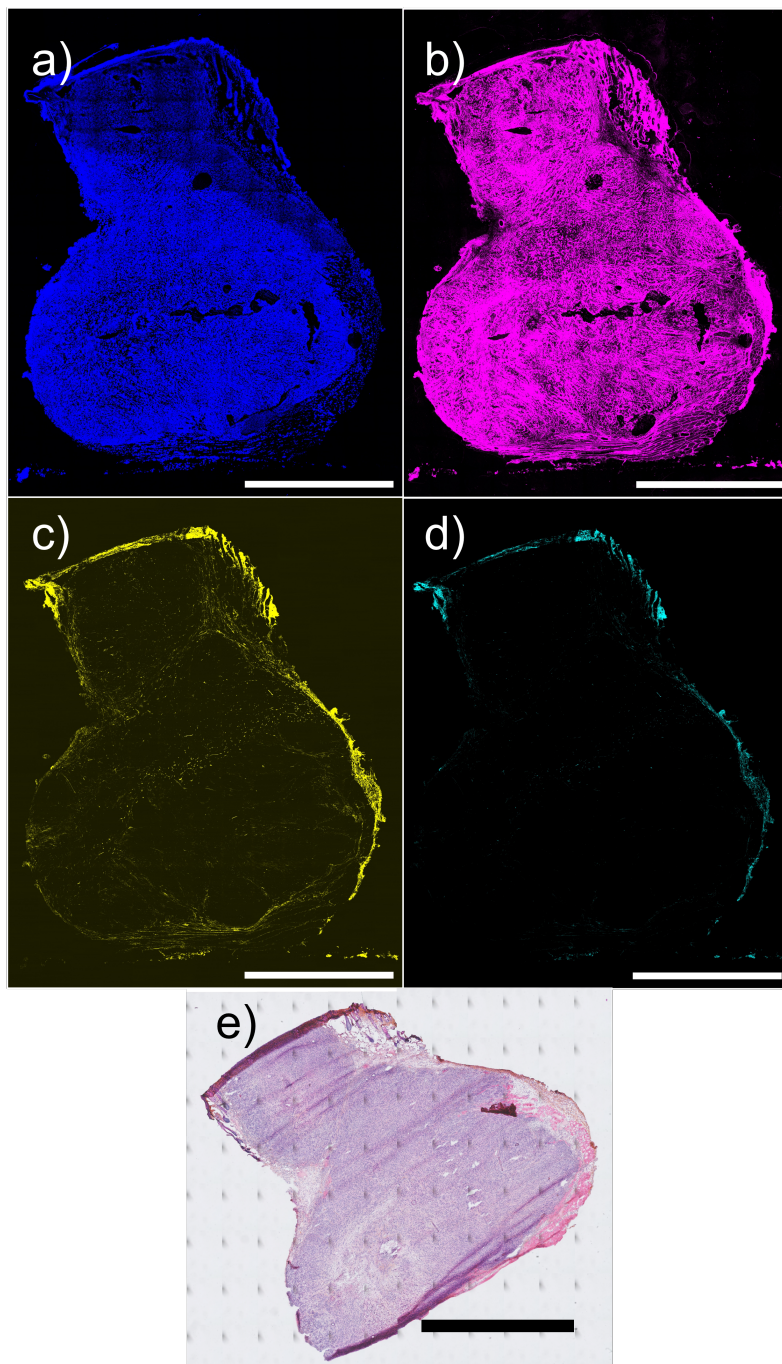


Figure B.3: Example of tile scans with KPC section T7. a) is the cell density tile scan, b) is the HA tile scan, c) is the collagen forward tile scan, and d) is the collagen backward tile scan. e) is the HES tile scan from the same tumor level. Brightness and contrast have been adjusted in the images. All scale bars are 2000 μm .

B.4 Blood Vessel and Nanoparticle Images

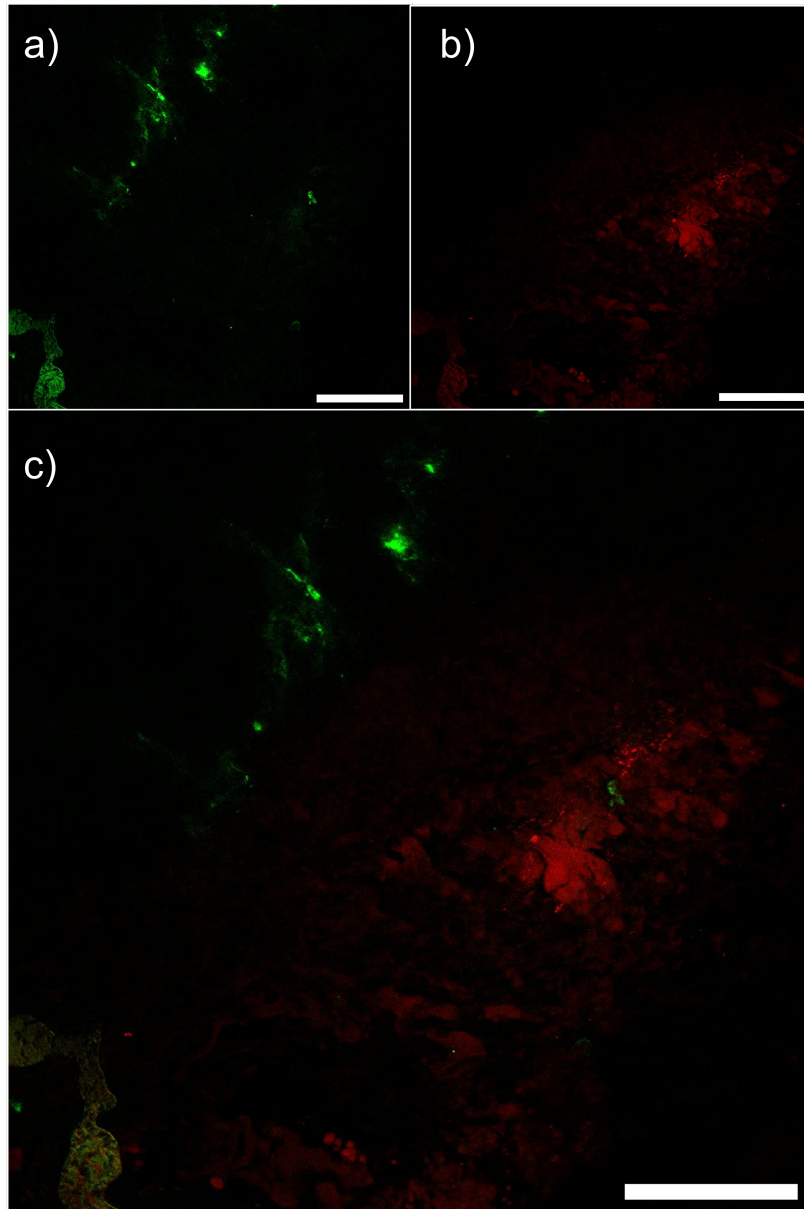


Figure B.4: Example of the blood vessel and nanoparticle images from 4T1 C2 tumor center. a) is the blood vessel image, b) is the nanoparticle image, and c) is the blood vessel and nanoparticle images merged. All scale bars are 100 μm .

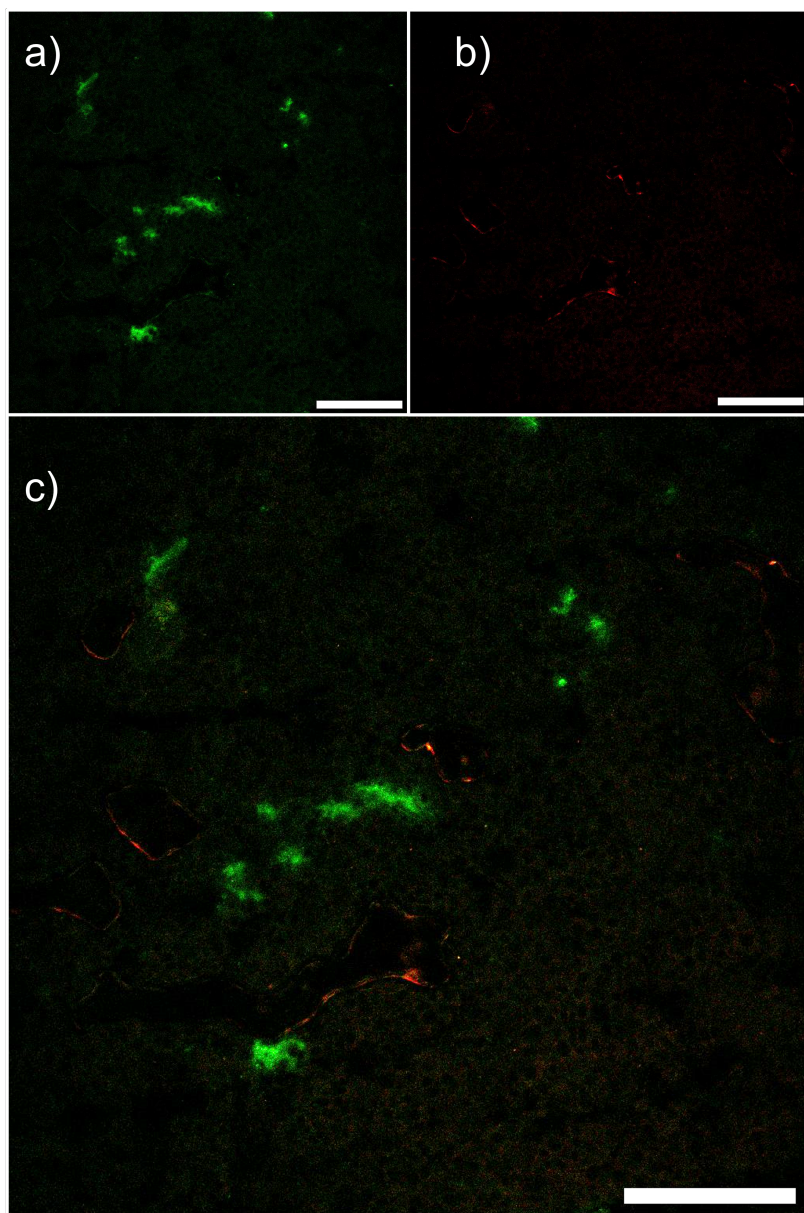


Figure B.5: Example of the blood vessel and nanoparticle images from CT26 C4 tumor center. a) is the blood vessel image, b) is the nanoparticle image, and c) is the blood vessel and nanoparticle images merged. All scale bars are 100 μm .

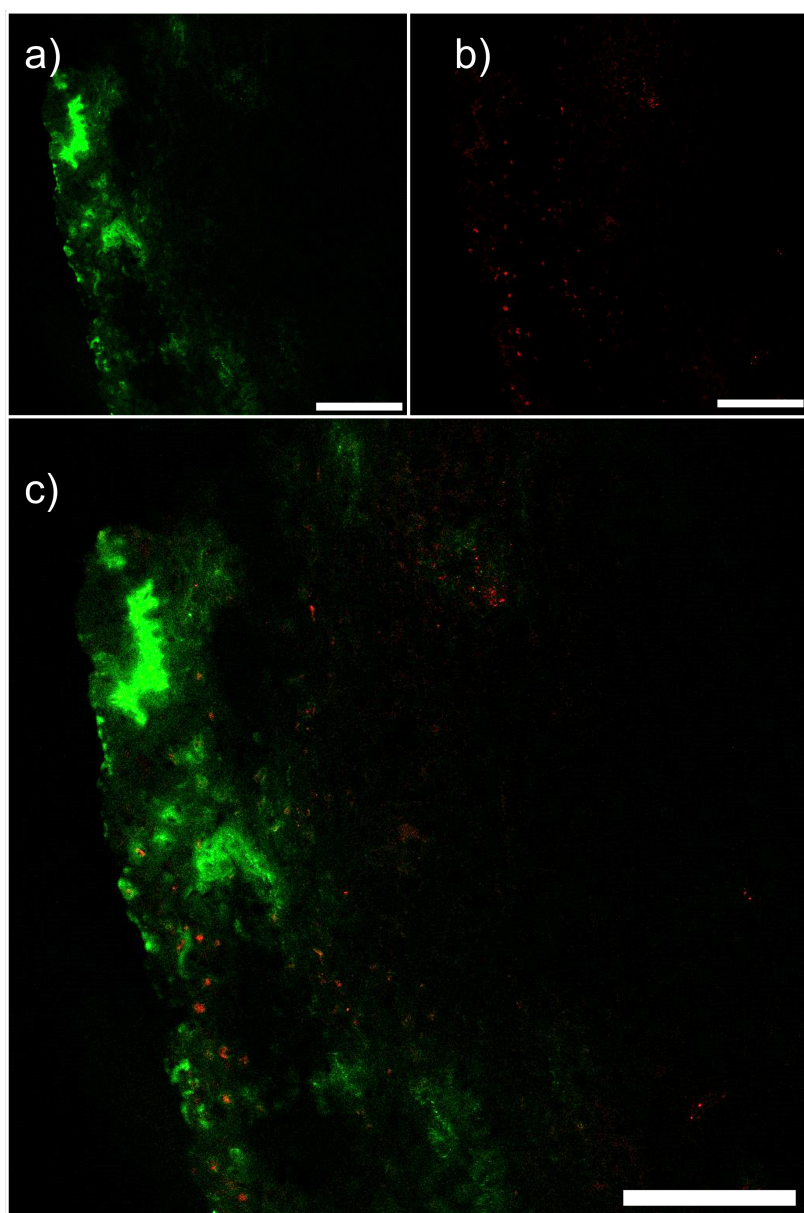


Figure B.6: Example of the blood vessel and nanoparticle images from KPC C8 tumor periphery. a) is the blood vessel image, b) is the nanoparticle image, and c) is the blood vessel and nanoparticle images merged. All scale bars are 100 μm .

Appendix C

Scripts

C.1 Hyaluronic Acid Image Processing Macroscript

```
1 //run("Brightness/Contrast...");
2 resetMinAndMax();
3 run("Subtract...", "value=10");
4 setAutoThreshold("Default dark no-reset");
5 //run("Threshold...");
6 setOption("BlackBackground", true);
7 run("Convert to Mask");
```

C.2 Collagen Image Processing Macroscript

```
1 name = getTitle();
2 run("Split Channels");
3 selectWindow("C1-"+name);
4 resetMinAndMax();
5 run("Median...", "radius=2");
6 //run("Threshold...");
7 setAutoThreshold("Triangle dark no-reset");
8 setOption("BlackBackground", true);
9 run("Convert to Mask");
10 selectWindow("C2-"+name);
11 resetMinAndMax();
12 run("Median...", "radius=2");
13 setAutoThreshold("Triangle dark no-reset");
14 //run("Threshold...");
15 run("Convert to Mask");
```

C.3 SHG F/B Ratio Macroscript

```
1 name = getTitle();
2 run("Split Channels");
3 selectWindow("C1-"+name);
4 //run("Brightness/Contrast...");
5 resetMinAndMax();
6 selectWindow("C2-"+name);
7 resetMinAndMax();
8 imageCalculator("Divide create 32-bit", "C1-"+name, "C2-
"+name);
```

C.4 Cell Density Image Processing Macroscript

```
1 //run("Brightness/Contrast...");
2 resetMinAndMax();
3 setAutoThreshold("Li dark no-reset");
4 //run("Threshold...");
5 setOption("BlackBackground", true);
6 run("Convert to Mask");
```

C.5 Blood vessel and Nanoparticle Pre-Processing Macroscript

```
1 imageName = getTitle();
2 run("Split Channels");
3 close();
4 close();
5 close();
6 selectWindow("C1-"+imageName);
7 run("Gaussian Blur...", "sigma=2");
8 //run("Threshold...");
9 setAutoThreshold("Triangle dark no-reset");
10 setOption("BlackBackground", true);
11 run("Convert to Mask");
12 run("Gray Morphology", "radius=3 type=diamond operator=
close");
13 selectWindow("C2-"+imageName);
```

```

14     run("Subtract...", "value=20");
15     run("Gaussian Blur...", "sigma=2");
16     setAutoThreshold("RenyiEntropy dark no-reset");
17     run("Convert to Mask");

```

C.6 Extravasation Distance Matlab Script

```

1
2 %Load the tif-files! Two channels: C1 and C3.
3 %Note: Additional file required: tiffread
4
5 %ENDRE PATH 'M.....' TIL NOE SOM PASSER P DI MASKIN!!
6     [Filename, Pathname] = uigetfile('*.tif;*.tiff;*.lsm',
7         'select the image file: ',...
8         'F:\FITC ATTO SHGFB - Mark and Find\Processed
9         images\CT26\199\Center', 'MultiSelect', 'On');
10
11     fprintf(1, 'First File: %s\n', [Pathname char(Filename(1))])
12     ;
13     fprintf(1, 'Last File: %s\n', [Pathname char(Filename(end))
14         ]);
15
16 nrFiles = round(length(Filename)/2);
17
18 prompt = {'Enter name of the SUM result file:', 'Dimension
19     of image: 2D or 3D', ...
20     'Pixel size dxy in microns: '};
21 dlg_title = 'Information';
22 %num_lines = 2;
23 dims = [1 35];
24 def = {'results.txt', '2D', '0.4545'};
25 answer = inputdlg(prompt,dlg_title,dims, def);
26
27 if answer{2} == '3D'
28     prompt = {'Pixel size dz in microns: '};
29     dlg_title = 'Information';
30     %num_lines = 2;
31     dims = [1 35];
32     def = {'1.0000'};
33     answer2 = inputdlg(prompt,dlg_title,dims, def);
34     dz = str2num(answer2{1});
35 end
36

```



```

31
32 filnavn = answer{1};
33 datafile = strcat(Pathname, filnavn);
34 SUM_datafile = strcat(Pathname, 'SUM_', filnavn);
35 np_fid = fopen(char(datafile), 'a');
36 SUM_fid = fopen(char(SUM_datafile), 'a');
37 fprintf(np_fid, 'NP lump\t Vol(u)\t coloc\t bor-bor(u)\n');
38 fprintf(SUM_fid, 'Files\t Total NPs\t coloc NPs\t nocoloc
    NPs\t Vol NPs(u)\t');
39 fprintf(SUM_fid, 'Vol BVs(u)\t Vol colocNPs(u)\t Vol
    nocolocNPs(u)\n');
40
41
42 %Syntax must be as follows: xxxx_BV_positionyy and
    xxxx_NP_positionyy
43
44 %locate all the NP-images in the list of files:
45 test = strfind(Filename, '_NP');
46 b = 1;
47 n = 1;
48 %group the NV and the BV files together, store position in
    the Filename cell
49 %array
50 for i = 1:length(Filename)
51     if isempty(test{i})
52         BVnr_Filename(b) = i;
53         b = b+1;
54     else
55         NPnr_Filename(n) = i;
56         % Locate the position of the '_' in '_NP', store in
    posn:
57         posn(n) = test{i};
58         n = n+1;
59     end
60 end
61
62 dxy = str2num(answer{3});
63
64 for f = 1:nrFiles
65     f_NP = [Pathname Filename{NPnr_Filename(f)}];
66     % find the position yy and find the corresponding BV-
    image
67     test = Filename{NPnr_Filename(f)}(posn(f)+4:end);
68     BV_pos = strfind(Filename(BVnr_Filename), test);

```

```

69     for b = 1:length(BV_pos)
70         if ~isempty(BV_pos{b})
71             f_BV = [Pathname Filename{BVnr_Filename(b)}];
72         end
73     end
74
75     filetxt= Filename{f};
76     fprintf(1,'Start analysis of:  %s\n',Filename{f});
77
78     BVO = bfoopen(f_BV);
79     NPO = bfoopen(f_NP);
80     %[dummy,nrZ] = size(BV);
81
82     %DENNE KODEN FUNGERER IKKE ALLTID
83     % Metadata = char(BVO{2});
84     %Find the dxy pixel size and the number of pixels in
the image
85     % sc_1 = length('Global scales=');
86     % dxypos = strfind(Metadata,'Global scales=');
87     % Reading four decimals, assuming format x.xxxx
88     % dxy = str2num(Metadata(dxypos+sc_1:dxypos+sc_1+5));
89
90     % Need to figure out how Metadata is organized for a 3D
image!
91     % --> not ready for 3D analysis yet!
92     BV1 = BVO{1,1};
93     NP1 = NPO{1,1};
94     nrZ = size(BV1,1);
95     XYdim = size(BV1{1,1});
96
97     for i = 1:nrZ
98         %binary images from ImageJ are 0 (black) and 255 (
white)
99         BWbv(:, :, i) = logical(BV1{1,1});
100        BWnptemp(:, :, i) = logical(NP1{1,1});
101    end
102
103    if answer{2} == '3D'
104        BWnp = imclearborder(BWnptemp,26);
105        % ...need to figure how to find the dz parameter in
a 3D image!
106
107        %calculate the nr (dr_dellump) of pixels in a 10 cubic
micron big lump!)

```

```

108     % nr_dellump = round(10/(dxy^2*dz));
109     % lumps of 9 pixels are removed!
110     nr_dellump = 9;
111     BWbv = bwareaopen(BWbv,nr_dellump);
112
113     %For binary matrix BWbv and BWnp, max 3D connectivity =
114     26
115     %Holes are already filled in ImageJ
116     BWnp = imfill(BWnp, 26, 'holes');
117     BWbv = imfill(BWbv, 26, 'holes');
118
119     %Need only perimeter-pixels to calculate bor-bor
120     distances!
121     BW_npp = bwperim(BWnp,26);
122     BW_bvp = bwperim(BWbv,26);
123     %CC = bwconncomp(BW_npp,26);
124     else
125     BWnp = imclearborder(BWnptemp,8);
126     %nr_dellump = round(10/(dxy^2));
127     %LUMPS SOM ER 1-2-3-4 PIXELS FJERNES!!!
128     nr_dellump = 4;
129     BWbv = bwareaopen(BWbv,nr_dellump);
130     BWbv = imfill(BWbv, 8, 'holes');
131
132     %SJEKK HVA SOM SKJER DERSOM DENNE KOMMANDOEN
133     FJERNES!! MED %
134     BWnp = imfill(BWnp, 8, 'holes');
135     BW_npp = bwperim(BWnp,8);
136     BW_bvp = bwperim(BWbv,8);
137
138     end
139
140     STATSnp = regionprops(BW_npp, 'PixelList');
141     STATSnp_fill = regionprops(BWnp, 'Area', 'PixelList');
142     N_np = length(STATSnp);
143     %Lnp = labelmatrix(CC);
144     %CC = bwconncomp(BW_bvp,26);
145     STATSbv = regionprops(BW_bvp, 'PixelList');
146     STATSbv_fill = regionprops(BWbv, 'Area', 'PixelList');
147     N_bv = length(STATSbv);
148
149     fprintf(1, 'Number of NPs and BVs: %i\t%i\n', N_np, N_bv)
150     ;
151     fprintf(1, 'Pixelsize (um): %6.4f\n', dxy);

```

```

148     % For the NP = n that have no coloc for the BV (1 to
149     N_bv), ie. all elements
150     % in row n = 0, calculate minimum bor-bor distance to
151     all the BV's.
152     % Use the STATSn and STATSbv for this!
153
154     % For the NP = n having coloc, some elements in the row
155     = 1, calculate the
156     % coloc, the fraction of n's volume that is inside a
157     vessel.
158     % Use the STATSn_fill and STATSbv_fill for this!
159
160     BVvol = zeros(1,N_bv);
161     %NPfrac = zeros(1,N_np);
162     NPvol = zeros(1,N_np);
163     borbor = zeros(1,N_np);
164     coloc = zeros(N_np,N_bv);
165     NPfrac = zeros(1,N_np);
166     Volcoloc = zeros(1,N_np);
167     %For every NP....
168     for i = 1:N_np
169         frac = zeros(1,N_bv);
170         nrpix = zeros(1,N_bv);
171         %...test coloc with all the BV's!
172         for j = 1:N_bv
173             Lia = ismember(STATSn_fill(i).PixelList,
174             STATSbv_fill(j).PixelList, 'rows');
175             if nnz(Lia) > 0
176                 coloc(i,j) = 1;
177                 frac(j) = nnz(Lia)/STATSn_fill(i).Area;
178                 nrpix(j) = nnz(Lia);
179             end
180         end
181         %It could be that a NP is coloc'ed with several BV'
182
183     NPfrac(i) = 100*sum(frac);
184     if answer{2} == '3D'
185         Volcoloc(i) = dxy^2*dz*sum(nrpix);
186     else
187         Volcoloc(i) = dxy^2*sum(nrpix);
188     end
189     % If there's no coloc, calculate bor-bor distance!
190     if nnz(coloc(i,:)) == 0
191         [npix, dummy] = size(STATSn(i).PixelList);

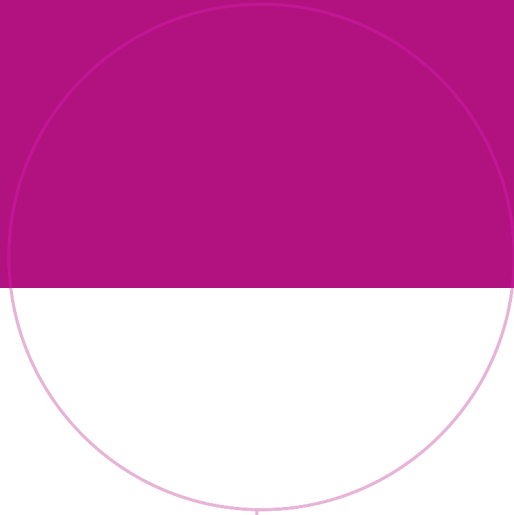
```

```

186         minpix = zeros(1,npix);
187         minBVPix = zeros(1,N_bv);
188         %Test for every BV
189         for j = 1:N_bv
190             for k = 1:npix
191                 x1 = STATSnp(i).PixelList(k,1);
192                 y1 = STATSnp(i).PixelList(k,2);
193                 if answer{2} == '3D'
194                     z1 = STATSnp(i).PixelList(k,3);
195                 end
196                 diffx = (STATSbv(j).PixelList(:,1)-x1)*
dxy;
197                 diffy = (STATSbv(j).PixelList(:,2)-y1)*
dxy;
198                 if answer{2} == '3D'
199                     diffz = (STATSbv(j).PixelList(:,3)-
z1)*dz;
200                 alldist=sqrt(diffx.^2+diffy.^2+
diffz.^2);
201                 else
202                     alldist=sqrt(diffx.^2+diffy.^2);
203                 end
204                 %alldist=sqrt((STATSbv(j).PixelList
(:,1)-x1).^2+(STATSbv(j).PixelList(:,2)-y1).^2+(STATSbv(
j).PixelList(:,3)-z1).^2);
205                 minpix(k) = min(alldist);
206             end
207             minBVPix(j) = min(minpix);
208         end
209         borbor(i) = min(minBVPix);
210     end
211     if answer{2} == '3D'
212         NPvol(i) = dxy^2*dz*STATSnp_fill(i).Area;
213     else
214         NPvol(i) = dxy^2*STATSnp_fill(i).Area;
215     end
216     fprintf(np_fid, '%i \t', i);
217     fprintf(np_fid, '%6.4f\t %6.4f\t %6.4f\n', NPvol(i),
NPfrac(i), borbor(i));
218     end
219
220     if answer{2} == '3D'
221         for j = 1:N_bv
222             BVvol(j) = dxy^2*dz*STATSbv_fill(j).Area;

```

```
223     end
224     else
225         for j = 1:N_bv
226             BVvol(j) = dxy^2*STATSbv_fill(j).Area;
227         end
228     end
229
230     fprintf(SUM_fid, '%s \t %i\t %i\t', char(Filename{f}),
N_np, N_np-nnz(borbor));
231     fprintf(SUM_fid, '%i \t %6.4f\t %6.4f\t', nnz(borbor),
sum(NPvol), sum(BVvol));
232     fprintf(SUM_fid, '%6.4f\t %6.4f\n', sum(Volcoloc), (sum(
NPvol)-sum(Volcoloc)));
233     %clear ind coloc borbor min_borbor max_coloc mass_c
mass;
234     clear BWbv BWnp
235
236     fprintf(1, ' Finished analysis of %s\n',Filename{f});
237 end
238 fclose(np_fid);
239 fclose(SUM_fid);
240 clear BVnr_Filename NPnr_Filename
241 %clear all
```



Norwegian University of
Science and Technology